UNIVERSITY OF CALIFORNIA

Santa Barbara

Principles of sensorimotor integration and olfactory processing

A Dissertation submitted in partial satisfaction of the

requirements for the degree

Doctor of Philosophy in Mechanical Engineering

by

Philip H. Wong

Committee in charge:

Professor Matthieu Louis, Co-Chair

Professor Jeff Moehlis, Co-Chair

Professor Enoch Yeung

Professor Linda Petzold

Professor Adele Doyle

June 2023

The dissertation of Philip H. Wong is approved.

_____
Adele Doyle

_____
Linda Petzold

_____
Enoch Yeung

_____
Jeff Moehlis, Committee Co-Chair

_____
Matthieu Louis, Committee Co-Chair

June 2023

ACKNOWLEDGEMENTS

I am fortunate to be co-advised by both an experimentalist, Matthieu Louis and a theorist, Jeff Moehlis. I would like to thank Matthieu for his unwavering support and his guidance in my journey from engineering with no prior biology background into the world of neuroscience. To Jeff, for fostering this fruitful collaboration at the intersection of experimental and theoretical neuroscience. I am grateful to both advisors for allowing me to explore the full closed-loop of interdisciplinary neuroscience research, from developing experimental tools, to simulating predicted results of behavioral assays, to building neural models from dynamical systems theory.

I would like to thank Vivek Jayaraman at Janelia Research Campus for the opportunity to visit as part of the Janelia visiting scientist program and for inviting me to the MSRI summer graduate school upon my arrival at Janelia. Working at Janelia allowed me to live and breathe neuroscience and was a life changing experience that I will cherish. I would like to thank Ann Hermundstad and the many members of Janelia Research Campus for their insightful comments and suggestions on my research.

I would like to thank Rubén Moreno Bote and Alexandre Pouget, for their long-standing collaboration with our lab and the additional perspective they brought that allowed us to elevate the multisensory integration project.

I would like to thank the senior members of Louis lab: Ajinkya, David, and Daeyeon, for their camaraderie and their mentorship during my initiation to neuroscience. I would like to thank Thuc, Kirstin, Mihai, and Nitesh, for joining us during the pandemic and rebuilding a lively community in the lab. I would like to thank my mentees: Tanish, and Nafi, for their outstanding consistent contributions to multiple projects.

Finally, I would like to thank my family for their encouragement throughout my graduate studies.

CURRICULUM VITAE

Philip H. Wong

Education

2023	**Ph.D. in Mechanical Engineering, Neuroengineering Emphasis** University of California, Santa Barbara
2016	**B.S. in Mechanical Engineering** Cornell University

Professional Experience

2018 – 2023	**Graduate Student Researcher** University of California, Santa Barbara
2018 – 2019	**Visiting Scientist** Howard Hughes Medical Institute, Janelia Research Campus
2017	**Graduate Student Researcher** University of California, Santa Barbara
2015 – 2016	**Research Assistant** Cornell University

Teaching Experience

Spring 2022	**Teaching Assistant** Course: ME 16 *Dynamics* Mechanical Engineering, University of California, Santa Barbara
Winter 2020	**Teaching Assistant** Course: ME 6 *Basic Electrical and Electronic Circuits* Mechanical Engineering, University of California, Santa Barbara

Spring 2017, 2018, 2019	**Teaching Assistant** Course: ME 151C *Thermosciences 3* Mechanical Engineering, University of California, Santa Barbara
Winter 2017, 2018	**Teaching Assistant** Course: ME 151B *Thermosciences 2* Mechanical Engineering, University of California, Santa Barbara
Fall 2016	**Teaching Assistant** Course: ME 104 *Mechatronics* Mechanical Engineering, University of California, Santa Barbara
Fall 2015	**Grader** Course: MAE 6510 *Advanced Heat Transfer* Mechanical Engineering, Cornell University

Mentoring

2022 – Present	**Nafi Khan** Undergraduate Research Assistant Biochemistry, University of California, Santa Barbara
2021 – Present	**Tanish Baranwal** Undergraduate Research Assistant / UCSB Research Mentorship Program 2021 EECS, University of California, Berkeley

Publications

David Tadres, **Philip H. Wong**, Thuc To, Jeff Moehlis, Matthieu Louis. "Depolarization block in olfactory sensory neurons expands the dimensionality of odor encoding", *Science Advances*, 2022.

Philip H. Wong, Andreas Braun, Daniel Malagarriga, Jeff Moehlis, Rubén Moreno-Bote, Alexandre Pouget, Matthieu Louis. "Computational principles of multisensory integration in the Drosophila larva", *Under Review at eLife*.

Philip Wong, Mahnoosh Alizadeh. "Congestion Control and Pricing in a Network of Electric Vehicle Public Charging Stations", *IEEE Allerton*, 2017.

ABSTRACT

Principles of sensorimotor integration and olfactory processing

By

Philip H. Wong

When confronted with an ever-changing and often perilous environment, how an organism behaves in response to uncertain and incomplete sensory information can be a matter of life and death. Besides the need to assess individual sensory signals accurately, sensory systems must also be able to integrate signals from multiple sensory modalities (e.g. visual, auditory, haptic), some of which may produce conflicting information. Through studying the insect brain of the *Drosophila* larva, we sought to unwrap the mathematical principles behind how animals process sensory signals to guide their behavior, with a focus on olfaction. In my dissertation, we employ computational models to investigate how the *Drosophila* larva transduces odors through its olfactory sensory neurons and combines these cues with other sensory modalities. We obtain three important clues towards understanding the neural implementation of sensory systems: 1. *Drosophila* larvae are capable of computing and combining the variance of sensory inputs to organize orientation behavior, suggesting that even relatively simple nervous systems can achieve probabilistic inference. 2. Upon prolonged increasing excitation, olfactory sensory neurons can counterintuitively transition from a spiking state to a silent state called depolarization block, which preserves sparsity in the neural code. 3. The bifurcation of spiking and silent states in olfactory sensory neurons driven by depolarization block allows *Drosophila* larvae to encode and discriminate different odors.

TABLE OF CONTENTS

LIST OF FIGURES

Introduction

The human brain is an unfathomably complex computing system. While we can easily recognize the scent of Chanel No. 5, identify the melody of our favorite song, and find our way to the bathroom at night in pitch darkness, many of the mechanisms behind how we process and make sense of the world around us have yet to be understood. In this dissertation, we attempt to characterize the principles of how neurons – the basic units of computation in the brain – process and encode information that we perceive in the world around us.

To understand how sensory information is processed by the brain, we turn to the neural circuitry of the *Drosophila melanogaster*. Commonly known as the fruit fly, the *Drosophila melanogaster* is an extensively studied model organism in both its adult and larval form. In this dissertation, we focus on the olfactory system of the *Drosophila* larva. With a nervous system of approximately 10,000 neurons [1], [2] (as opposed to the 86 billion of the human brain [3]), the *Drosophila* larva is an ideal model organism for studying the functions of individual neurons and neural circuitry at a simple, mechanistic level.

The first chapter (adapted from [4]) centers on multisensory integration, a process by which the nervous system consolidates information simultaneously from multiple senses. Here, we characterize the computational principles behind how the *Drosophila* larva combines information from sensory modalities like temperature and odor. The second chapter (adapted from [5]) describes our discovery of an unexpected feature called depolarization block in olfactory sensory neurons - the neurons involved in the sensation of

smell. While this phenomenon was previously viewed as an anomaly, we demonstrate why we believe that depolarization block may have profound implications on how smells are encoded by the olfactory system. With this discovery in mind, the third and final chapter examines how olfactory sensory neurons encode and allow the brain to discriminate different odors: for example, the fragrance of a flower versus the pungent stench of the durian fruit. While we are far from demystifying the neural representation of smell, we find evidence that depolarization block may be a feature that expands and facilitates the peripheral encoding of odors.

Our methodology in each study involves a synergy of in-vivo experiments and in-silico computer simulations. Through a closed feedback loop between experimental and theoretical neuroscience, we iteratively build on data-driven computational models that not only reveal conceptual insights about how neural circuits perform computation, but also inspire new hypotheses to be verified through experimentation. Although it is often said that “all models are wrong”, we hope that this dissertation demonstrates the value and versatility of computational models in neuroscience.

Computational principles of adaptive multisensory combination

Introduction

When confronted with an ever-changing and often perilous environment, how an organism behaves in response to uncertain and incomplete sensory information can be a matter of life and death. Besides the need to assess individual sensory signals accurately, sensory systems must also be able to integrate signals from multiple sensory modalities (e.g. visual, auditory, haptic), some of which may produce conflicting information. This task of "multisensory cue combination" has therefore been the focus of many studies, particularly in psychophysics, to characterize its implementation in different organisms and to evaluate whether these solutions are optimal from a probabilistic point of view [6].

One mechanism adopted by organisms to integrate noisy (fluctuating) information arising from different sensory modalities is to prioritize signals based on their relative uncertainty (variance) by using a principle of Bayesian inference. This strategy has the advantages of allowing adaptation to sudden changes in the environment, permitting the filtering of irrelevant information (noise), and improving the signal-to-noise ratio of the combined signal. In humans, for example, the visual-haptic estimation of the height of an object is close to optimal and closely matches the Bayesian estimate [7]. Similar results have also been observed for other tasks in humans [8], as well as in primates [9]. To a lesser extent, recent evidence indicates that insect brains may also be capable of implementing similar strategies of cue combination, for example in the integration of directional

information in ants [10], [11]. In addition, the neural integration of multisensory cues has been studied in the adult *Drosophila* and it has been shown that flies are able to dynamically adjust their response to conflicts between visual, olfactory and airflow cues [12].

Although the neural implementation of cue combination is not well-understood, various theories speculate about how neural ensembles can implement probabilistic inference [13], [14]. While certain theories require neuronal populations to encode probabilities and information about signal variance [13], others suggest the possibility of encoding variability through synaptic plasticity in single neurons [14]. Further characterizing multisensory cue combination in a comparatively simple model organism like the *Drosophila* larva is advantageous, not only to reveal how strategies evolve through development, but also to delineate the minimal complexity required to mechanistically implement strategies of multisensory-cue combination [15].

While it has yet to be shown how the *Drosophila* larva implements cue combination in natural conditions, previous studies have examined how turns are triggered in the *Drosophila* larva in response to the combination of aversive light input and attractive virtual odor input [16], [17]. In the first study, a computational model that describes the basic transformation of sensory input into turning decisions was built to investigate the sequence of mathematical operations combining multi-modal inputs [16]. In subsequent work, a modified version of the same model was used to establish that signals triggering turns adapt to the variance of the individual multi-modal sensory inputs [17]. In the present work, we investigate whether this form of variance adaptation fits into traditional cue combination models as observed in other animals and dissect how the mechanism underlying the combination of multi-modal inputs contributes to the overall navigational strategy of the

larva. Specifically, we investigate how the *Drosophila* larva responds to gradients of two independent odors, as well as the combination of an odor and a temperature gradient. While chemotaxis and thermotaxis have been studied extensively in the larva [18]–[20], little is known about how unimodal navigational mechanisms contribute to navigation in unison.

Experimentally, we investigate combinations of thermotactic and olfactory (real and virtual) stimuli in scenarios where cues are directionally similar (congruent) or in opposing (conflicting) directions. Furthermore, we test conditions where noise is added optogenetically to the peripheral olfactory system to study how the combination of multisensory cues adapts to changes in the variance of individual sensory inputs. To capture the precise reorientation mechanisms and navigational behavior of larvae in these scenarios, we built a data-driven agent-based model inspired by Wystrach et al. [21] that represents both turn rate and turning direction, and models how different sensory inputs are processed and transformed into behavioral outputs. Using this agent-based framework, we tested and simulated different experimental paradigms to narrow down the set of plausible mechanisms for multisensory cue combination in the *Drosophila* larva through a process of elimination. With this approach, we explore computationally how larvae use signal variance to weigh and combine unreliable sensory information from multiple modalities. Using our agent-based model, we conduct a perturbative analysis to characterize the modulatory impact of cue combination on individual aspects of the control of locomotion underlying sensory navigation.

Motivated by a need to go beyond cue-combination models that specifically estimate the properties of a single object (e.g., the width of a bar, [7]), we explore different notions of optimality related to sensory navigation in response to realistic configurations of multimodal

gradients. Through a generalized formalism of cue-combination strategies, we define a bimodal contrast coefficient that represents the degree to which signal variance is prioritized over the value (reward) of individual signals in the combination of multimodal sensory inputs. In addition to the observation that larvae are near-optimal in both formalisms, we find that their cue-combination strategy can adapt depending on the nature of the sensory information available to the animal.

Materials and Methods

Parameter-Free Model

Drosophila larvae sample the environment to gather information about local odor and temperature gradients through head casts and runs to guide their behavior [22]. We assume that local information is relatively weak as it is corrupted by fluctuations due to intrinsic noise in the local gradient; thus, the larva needs to accumulate information over time. Two main experimental setups are considered here: one in which two odor gradients are present (one real and another virtual generated by optogenetic stimulation), corresponding to the 'intramodal' condition, and another in which an odor and a temperature gradient are present, corresponding to the 'intermodal' condition. Mathematically these two conditions can be described with the same formalism, and therefore we do not distinguish them here. We generally use 'cue 1' and 'cue 2' to refer to either odor or temperature gradients, regardless of the sensory modality used. We will also model the effect of noise injection through optogenetics.

Our model is based on the idea that the larva's goal is estimating a hidden binary variable s, with values -1 and 1, denoting the 'best location in the world': if $s = 1$, then the

goal location is on the right of the petri dish; if $s = -1$, then the goal location is on the left. The larva estimates this hidden variable by iteratively sampling gradients through the space. We assume that up to time t the accumulated evidence for cues 1 and 2 is characterized by sampled gradients Δc_1 and Δc_2, respectively. These sampled gradients correspond to the accumulated local sampled gradients, which are lumped together into a single mean-field value. Since sensory observations are noisy due to intrinsic and extrinsic variability, the sampled gradients are corrupted versions of the true gradients, $\Delta c_1^0$and Δc_2^0 with Gaussian noise. Because both gradients are generated congruently, then we can use the same hidden variable s to express $\Delta c_1^0 = s\Delta C_1$ and $\Delta c_2^0 = s\Delta C_2$, where $\Delta C_i \geq 0$ are the absolute values of the true gradients Δc_i^0, $i = 1, 2$. Therefore s represents the sign of the gradient, which points towards the goal location, while $\Delta C_i \geq 0$ controls the intensity of the gradients. The sampled gradients follow then the equations:

$$\begin{aligned} \Delta c_1 &= s\Delta C_1 + \sigma_1 n_1 \\ \Delta c_2 &= s\Delta C_2 + \sigma_2 n_2 \ , \end{aligned} \tag{1}$$

where $n_i (i = 1, 2)$ are independent normal random variables with zero-mean and unit variance, and σ_i is the inverse reliability of the *i*-th cue. Control of independence of the fluctuations of the two cues can be achieved in our experiments by using odor and virtual odor gradients.

It is important to emphasize that the primary goal of the larva is to estimate the value of the hidden variable s rather than estimating the true values of the gradients ΔC_i through the sampled gradients Δc_1 and Δc_2. The variable s (the sign of the gradient) specifies the goal location, while the absolute value true gradients are uninformative about the goal location. As the larva estimates the value of the variable s, it moves to the estimated goal location. It is important to note that the larva does not have direct access to the true gradient ΔC_i and to the hidden variable s. In contrast, in the model the larva has direct access to the inverse reliabilities of each cue through sampling of the noise, as is well documented in other similar scenarios [7]. This assumption is also supported by our experimental observations.

Errors in the estimated goal location can occur when the two sampled gradients have a different sign with respect to the true location (e.g., when $\Delta c_1 < 0$, $\Delta c_2 < 0$ and $s = 1$). When one of the sampled gradients is positive but the other is negative, then the larva should weigh them according to the reliabilities of each cue. There is a unique way of combining the sampled gradients optimally, the so-called optimal strategy, which we will derive. Our framework is based on Bayesian inference of the hidden variable s, which corresponds to the optimal strategy in the sense that the goal location is attained with the highest probability. Given the sampled gradients Δc_1 and Δc_2, one can build the posterior probability of the hidden variable s and the absolute true gradients as $p(s, \Delta C_1, \Delta C_2 | \Delta c_1, \Delta c_2)$. Using Bayes rule,

$$\begin{aligned} p(s, \Delta C_1, \Delta C_2 | \Delta c_1, \Delta c_2) &\propto p(\Delta c_1, \Delta c_2 | s, \Delta C_1, \Delta C_2) \\ &= p(\Delta c_1 | s, \Delta C_1) p(\Delta c_2 | s, \Delta C_2) \end{aligned} \tag{2}$$

where the proportionality is in relation to s, $\Delta C_1$and ΔC_2. Since the sampled gradients specify the order of magnitude of the true gradients, and because the true gradients are distributed over several orders of magnitude, we ignore the prior distribution on the true gradients above (effectively, we assume that the prior is flat). In addition, on the right side of the equation we assume that, conditioned on the true gradients and goal location, the fluctuations of the sampled gradients are independent. This is strictly true in our experimental condition in which one gradient is odor and the other is a virtual odor gradient, and they are close-to-independent in other conditions because of the random mixing of odors due to chaotic dynamics in fluids.

Using eq. (1), $p(\Delta c_i | s, \Delta C_i) = N(\Delta c_i | s\Delta C_i, \sigma_i^2)$ for $i = 1,2$, that is, the density is a Gaussian probability density with mean $s\Delta C_i$and variance σ_i^2. Inserting this expression into eq. (2), we find

$$p(\Delta c_1, \Delta c_2 | s, \Delta C_1, \Delta C_2) \propto e^{\left(-\frac{(\Delta c_1 - s\Delta C_1)^2}{2\sigma_1^2} - \frac{(\Delta c_2 - s\Delta C_2)^2}{2\sigma_2^2} \right)}. \tag{3}$$

Optimal behavior involves determining the distribution of the hidden variable, but ignoring the absolute values of true concentration gradients, as the latter are not informative

about the goal location. Therefore, we are interested in the posterior over the hidden variable s, where the absolute values of the gradients are marginalized,

$$p(s|\Delta c_1, \Delta c_2) \propto \int_0^\infty d\Delta C_1 \int_0^\infty d\Delta C_2 \; p(s, \Delta C_1, \Delta C_2|\Delta c_1, \Delta c_2) \; . \tag{4}$$

Using eqs. (2-4) and the definition of cumulative Gaussian, $\Phi(x) = \int_{-\infty}^{x} dy N(y \mid 0,1)$, we find

$$p(s|\Delta c_1, \Delta c_2) \propto \Phi(s\Delta c_1/\sigma_1)\Phi(s\Delta c_2/\sigma_2) \; . \tag{5}$$

To find a closed expression for $p(s|\Delta c_1, \Delta c_2)$ we approximate the cumulative Gaussians by sigmoid functions, which is known to be an excellent approximation for the best fit parameters (that is, $\Phi(x)$ is approximated by $\Phi(x) \sim 1/(1 + e^{-\alpha x})$, where α is the best fit parameter). Therefore, within this approximation, we can write the probability over s as

$$p(s|\Delta c_1, \Delta c_2) = \frac{1}{1+\mathrm{e}^{(-\alpha(\Delta c_1/\sigma_1 + \Delta c_2/\sigma_2)s)}} = \frac{1}{1+e^{-\alpha\, d\, s}}. \tag{6}$$

where we have defined the 'decision variable d'

$$d = \Delta c_1/\sigma_1 + \Delta c_2/\sigma_2 \; . \tag{7}$$

Note that the decision variable weighs the size of the sampled gradients with the reliability of each gradient.

Obtaining the decision variable is one of the central results of this section, as it dictates what the larva should do trial by trial based on the sampled gradients and their reliability. Specifically, when the decision variable is positive, $d > 0$, the probability of $s = 1$ is larger than one half, and therefore optimal behavior dictates moving towards the right. If the decision variable is negative, then optimal behavior dictates moving towards the left. In summary, the decision rule reads:

$$\begin{gathered} \text{“choose } s = 1\text{”} \quad \text{if} \quad d > 0 \\ \text{"choose } s = -1\text{"} \;\; \text{if} \quad d > 0. \end{gathered} \tag{8}$$

It is important to emphasize that for a larva to follow the optimal behavior it should follow the decision rule in eq. (8). This obviously does not mean that the neuronal circuitry needs to perform explicitly the computation described in eqs. (2-6): all these computations can be bypassed if the decision rule in eq. (8) is hardwired within the neuronal circuits.

The decision rule in eq. (8) is a deterministic rule given the sampled gradients Δc_1 and Δc_2. However, we do not have access to the sampled gradients as measured by the larvae. This means that the value of the decision variable d at any particular trial is unknown to us. This implies in turn that we can only know the behavior of the larvae averaged over observations given a predetermined experimental setup, which is characterized by the true gradients $\Delta c_1^0 = s\Delta C_1$ and $\Delta c_2^0 = s\Delta C_2$. We will take advantage of the fact that, while the true gradients are unknown to the larvae, they are known to the experimenter.

We first note that d is the sum of two Gaussian variables, and therefore it is a Gaussian variable. Its mean and variance are respectively:

$$\begin{aligned} \bar{d}(\Delta C_1, \Delta C_2) &= \frac{\Delta C_1}{\sigma_1} + \frac{\Delta C_2}{\sigma_2} \\ Var(d)(\Delta C_1, \Delta C_2) &= 2\,, \end{aligned} \tag{9}$$

where we assume without loss of generality that the goal location is at $s = 1$. From this expression we can compute the central experimental measurement, the preference index, PI. This quantity is defined experimentally as the number of larvae that at time *t* are located on the correct half-side of the petri dish, $s = 1$. We can make a prediction using eq. (9) by noticing that the PI is the fraction of times that the decision variable *d* is above zero,

$$PI(\Delta C_1, \Delta C_2) = \Phi\left(\frac{\Delta C_1}{\sqrt{2}\sigma_1} + \frac{\Delta C_2}{\sqrt{2}\sigma_2}\right). \tag{10}$$

This equation provides a prediction of the preference index when the two gradients are present. Now we can use the same expression to find expressions for the preference indexes for the single-gradient conditions as

$$\begin{aligned} PI(\Delta C_1) &= P_I(\Delta C_1, \Delta C_2 = 0) = \Phi\left(\frac{\Delta C_1}{\sqrt{2}\sigma_1}\right) \\ PI(\Delta C_2) &= P_I(\Delta C_1 = 0, \Delta C_2) = \Phi\left(\frac{\Delta C_2}{\sqrt{2}\sigma_2}\right). \end{aligned} \tag{11}$$

Finally, we can use eqs. (10-11) to obtain the combination rule

$$PI_{Model}(\Delta C_1, \Delta C_2) = \Phi(\Phi^{-1}(P_I(\Delta C_1)) + \Phi^{-1}(P_I(\Delta C_2)))\,, \quad (12)$$

where $\Phi^{-1}(x)$ is the inverse cumulative normal. Thus, using the same sigmoidal approximation of the cumulative Gaussian employed above, we obtain the coarse-grained model given by eq. (2) in the main text. Another important feature of these predictions, which will be exploited later, is that optogenetic stimulation can affect the reliability of each cue in predefined ways. In particular, it should be possible to increase the noise level of cue 1 without affecting the noise level in cue 2. If this happens, then the model predicts that the preference index when only cue 2 is present should remain unchanged in the presence of noise in cue 1. To understand this result, note that in this rule increasing the variance of one signal does not change the total variance of eq. (9), which implies that it is not possible to shut down a cue even if it is very noisy. This is however the optimal thing to do under the above assumption, as the signal is scaled down by the standard deviation of the noise, but gives a different result than the variance weighted combination rule of eq. (44) in the main text. In the main text, $PI_{Model}(\Delta C_1, \Delta C_2)$ is denoted as $PI_{1+2,Model}$.

Agent-based Model

We model *Drosophila* larvae with an adapted version of an agent-based model developed by Wystrach et al. [21]. This model provided a general framework for describing taxis behavior in unimodal stimulus gradients, based on evidence that larvae display continuous lateral oscillations ("head-casts") of the anterior body during peristalsis. Their work showed that this simple mechanism coupled with the direct sensory modulation of oscillation amplitude could reproduce many taxis signatures observed in larvae. To test different mechanistic hypotheses for cue integration, we build upon this framework to investigate how information can be combined across real odor, virtual odor, and temperature gradients to modulate taxis.

Lateral Oscillation Model

In our adaptation of the above agent-based model we consider the anterior and posterior body of the larva as two connected segments. The anterior body is modelled as a single segment from the midpoint to the head (Figure 1A). To mimic active sampling, this segment rotates about the midpoint and alternates between left and right rotations between timesteps (Figure 1B), with casting amplitude modulated by the sensory experience. The posterior body on the other hand, is "passive" and assumed to follow the axis of the anterior segment. Larvae are assumed to be uniform in length and move along the anterior heading direction at a constant speed. At any timestep n of 1s, this mechanism can be summarized with the following state-update equations:

$$\begin{aligned} \theta_n &= \theta_{n-1} + \delta_\theta(d)(-1)^n \\ x_n &= x_{n-1} + v\cos(\theta_n) \\ y_n &= y_{n-1} + v\sin(\theta_n), \end{aligned} \tag{13}$$

where θ_n is the heading direction of the anterior body relative to the midpoint at timestep n, v is the distance travelled in a single time-step, and $\{x_n, y_n\}$ is the updated midpoint of the larva. The quantity $\delta_\theta(d)$ is the casting amplitude, which is modulated by a decision variable d that is a function of the sensory experience (see below). The constant v was estimated based on the average speed observed in larva in the experimental data. In ref. [21], the amplitudes of the lateral oscillations is modelled as a hard-limit ramp function:

$$\delta_\theta(d) = H(\theta_B + d), \text{ where } H(x) = \begin{cases} x & 0 \le x \le \pi \\ \pi & x > \pi \\ 0 & x < 0 \end{cases}, \tag{14}$$

where θ_B is the baseline amplitude of the lateral oscillations in the absence of stimuli (i.e. when $d = 0$). During larval chemotaxis, turning increases during upgradient motion whereas it is reduced during downgradient motion. Accordingly, the decision variable d should be negative when moving up a stimulus gradient and positive when moving down a stimulus gradient.

One important feature of our adaptation of the agent-based model that is distinct from Wystrach's model [21] is that sensory measurements are sampled at every time-step by a sensor located at the extremity of the larva's head, which rotates about the midpoint. This allows us to distinguish between head casting during "runs" when the larva is undergoing forward peristalsis and head casting during "stops", when the midpoint of the larva is stationary. In contrast, the larva in ref. [21] is modelled as a point agent that rotates on the spot for simplicity. Note that in our model, the position of the larva head is given by:

$$\begin{aligned} x_n^h &= x_n + \frac{l}{2}\cos(\theta_n) \\ y_n^h &= y_n + \frac{l}{2}sin(\theta_n)\,, \end{aligned} \tag{15}$$

where l is the average length of larva at the 3rd instar developmental stage.

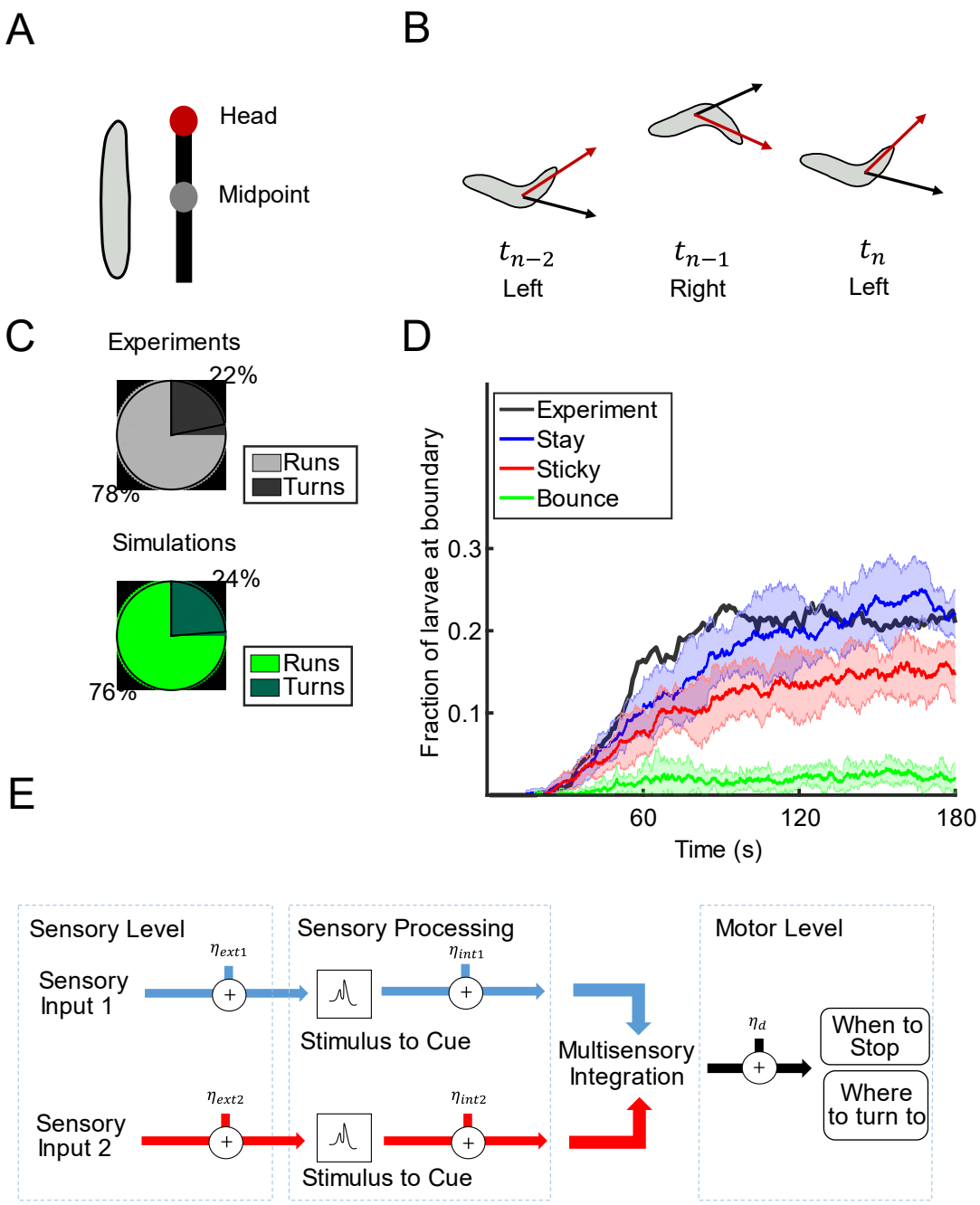

Figure 1: Parameter optimization and performance quantification of the agent-based model for larval navigation. (A) Illustration of the framework of the lateral oscillation

model used for the agent based model. The larva is modelled as two segments: the anterior (midpoint to the head) and the posterior (tail). **(B)** The larva alternates between left and right head-casts between every timestep. The black arrow illustrates the direction of motion at the previous timestep while the red arrow is the heading vector at the indicated timestep. **(C)** Ratio of runs and stops observed in real larvae versus in simulations in the absence of stimuli. (n = 100 larvae) **(D)** Simulation results for the fraction of larvae at the walls of the arena for hypothetical boundary conditions tested when designing the agent-based model. Larvae are defined as being at the boundary if they are within one larva-length from the edge of the arena. Lines represent the mean and shaded error bars represent one standard deviation (n = 10 groups of 100 larvae). **(E)** Stages at which noise is added in the agent-based model.

Stopping

For the lateral oscillation model developed in ref. [21], it was noted that stopping was not essential for chemotaxis except for improving orientation by enabling larger turns in their paths. Thus, this mechanism was ignored as a simplifying assumption and larvae were simulated to run continuously at a fixed speed. However, in order to accurately represent larvae navigation about odor sources in our experimental paradigms, it was necessary to incorporate the mechanism of stopping. We make the following modelling assumptions regarding larvae runs and stops:

1. During runs, larvae move along the anterior heading direction at a constant speed (as before).
2. During stops, larvae remain stationary at the midpoint but are still able to cast the anterior body in either direction.
3. The casting amplitude is larger during stops than during runs.

To capture the behaviors associated with running and stopping in our agent-based model, we assume that larvae not only update their heading direction at each time-step, but also make a

decision to run or to stop. Therefore, there are two decisions that must be made at every time-step:

1. *When to Stop*: Should the larva be in a running or stopping state?
2. *Where to Turn*: Given the state of the larva, what adjustment should be made to the current heading?

When to stop

We modeled running and stopping in larvae as a binary Markov process, with transition probabilities dependent on the same decision variable d (Figure 7E). The transition probabilities between states were given by the following logistic functions:

$$p_{run}(d) = \frac{1}{1 + e^{-d+c_{run}}}$$
$$p_{stop}(d) = \frac{1}{1 + e^{-d+c_{stop}}}. \quad (16)$$

The parameters c_{run} and c_{stop} are constants that determine the statistics of running and stopping in the absence of sensory stimuli (i.e. d = 0). Using the classification algorithm of the closed loop tracker from ref. [23], we quantified the statistics of running and stopping in unstimulated larvae (Figure 1C). We then used maximum likelihood estimation to fit parameters c_{run} and c_{stop} in our model (Figure 2A-D). We verified that the negative binomial distribution of running and stopping durations resulting from the simple Markov model showed a reasonable agreement with actual data.

Where to turn to

Using experimental data generated with a closed loop tracker [23], we observe differences in both casting amplitude and casting speed in the two states. Given that the dynamics of head casting differ in running and stopping, separate schemes are required to describe the casting amplitude of these two states:

$$\delta_\theta(d) = \begin{cases} \delta_{\theta,run}(d) & during\ runs \\ \delta_{\theta,stop}(d) & during\ stops \end{cases} \tag{17}$$

$$\delta_{\theta,run}(d) = \frac{\theta_{M,run}}{1+e^{-\gamma d}}$$

$$\delta_{\theta,stop}(d) = \frac{\theta_{M,stop}}{1+e^{-\gamma d}}.$$

Here, we use a smooth approximation of the hard limit ramp function in Wystrach et al. [21]. The parameter θ_M can be viewed as a physical constraint on the maximum casting amplitude or head casting speed in running and stopping states. These constants were estimated to fit the physical constraints of the head casting speeds of real larvae. γ is a tuning parameter that governs the slope of the ramp and allows for differences in how the decision variable d modulates casting amplitude compared to stopping. The resulting head-casting speeds generated by our model were in agreement with real unstimulated larvae from the closed loop tracker.

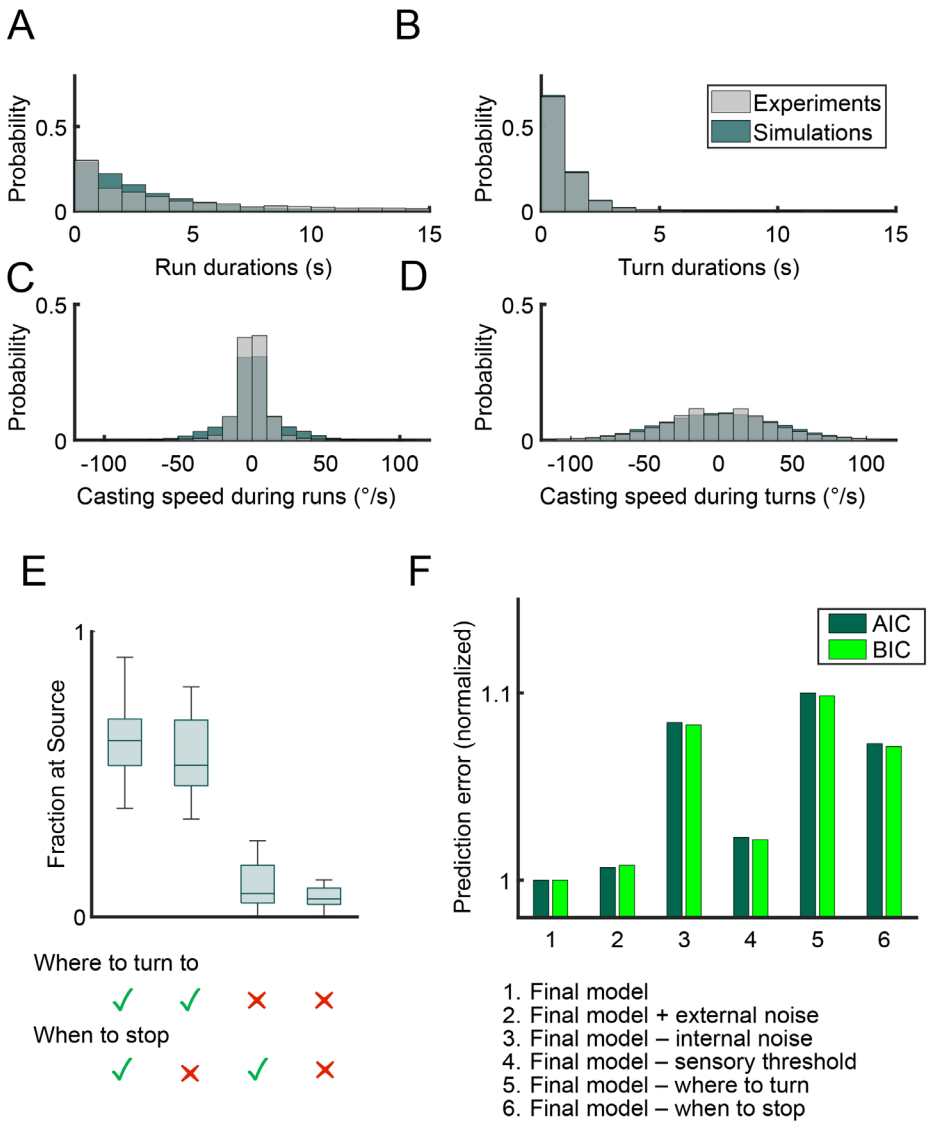

Figure 2: Parameter optimization and performance quantification of the agent-based model for larval navigation. (A-D) The histograms compare the behavioral statistics of real larvae to simulated larvae (n = 100 larvae): (A) run durations, (B) turn durations, (C) casting speed during runs, (D) casting speed during turns. (E) Performance of the agent-based model with the removal of its constituent mechanisms ("*where to turn to*", "*when to stop*") to direct larvae up gradients. When either mechanism is removed, a smaller fraction of larvae reach the source. (Odor + odor congruent, n = 19 groups of 20 larvae). (F) Justification of model

complexity. The plot indicates the change in prediction error as quantified by the AIC/BIC as variables are removed or added to the agent-based model. (Odor + odor congruent, n = 19 groups of 20 larvae)

Sensory Stimulus

In the present section, we outline the models used to describe the stimulus presented to the larvae. In each experimental paradigm, we presented combinations of dynamic real odor gradients, with static virtual odor gradients and static temperature gradients. At each timestep, we assume that the larva receives a sensory input $C_n(x_n^h, y_n^h)$ that is dependent on its head position $\{x_n^h, y_n^h\}$ in the assay at timestep n.

Odor

Two different odors were used in experiments, 1-hexanol and ethyl butyrate. In each experiment, a small odor droplet was placed in an enclosed assay and gradually diffused over the course of three minutes. Since we observed changes in the behavioral response to the odor stimulus over the course of each experiment, we could not assume that the odor gradient was static. Hence, we modeled the evolution of an odor gradient as a diffusion process from a point source as outlined in ref. [23]. At timestep n, the solution to diffusion partial differential equation is:

$$C_n(x_n^h, y_n^h) = \int_0^n \frac{J_{odor}}{(4\pi D n)^{3/2}} e^{-\frac{r^2}{4Dn}} dn, \tag{18}$$

where r denotes the Euclidean distance from the larva head to the odor source $r = \sqrt{\left(x_s - x_n^h\right)^2 + \left(y_s - x_n^h\right)^2}$ and J_{odor} is the flux of the odor droplet. D is the diffusion

coefficient of the odor droplet in air, which differs slightly between *1-hexanol* and *ethyl butyrate*. These values were estimated using the method in ref. [24].

Temperature

The behavioral experiments feature a linear temperature gradient that varied from $T_{\min} = 16^{o}\mathrm{C}$ to a maximum of $T_{\max} = 30^{o}\mathrm{C}$ (aversive to larvae). For example, a temperature gradient increasing in the positive x-direction would be given by:

$$C_n(x_n^h, y_n^h) = T_{\min} + (T_{\max} - T_{\min})(\frac{x}{2R}), \tag{19}$$

where R is the radius of the arena. Under the rearing conditions of the experiments, larvae are drawn to the cooler end of this temperature range.

Virtual Odor

In the experiments with real larvae, we passed emitted light from a LED through an exponential filter to create a Gaussian source for optogenetic virtual odor experiments. This is modelled as:

$$C_n(x_n^h, y_n^h) = J_{light} e^{-\frac{r^2}{2\alpha^2}}, \tag{20}$$

where *r* is again the distance to the source $= \sqrt{\left(x_s - x_n^h\right)^2 + \left(y_s - x_n^h\right)^2}$, J_{light} specifies the intensity of the light stimulus, and α is the standard deviation of the Gaussian function. This mathematical fit is supported by measurements of the physical gradient using a photodiode.

Sensory Threshold

For experimental conditions involving real odors, we noticed that there was a slight delay in the behavioral response of real larvae at the onset of the experiment. Given that the odor source is introduced in the assay at the same time as larvae, we speculate that the lag in directed behavior is due to the time required for the odor to build up to detectable levels in the arena. To account for this effect, we introduced a sensory threshold parameter β such that:

$$C_n(x_n^h, y_n^h) = 0 \quad if\ C_n(x_n^h, y_n^h) < \beta. \tag{21}$$

For consistency, we included this threshold as a parameter to be optimized by the framework for all three sensory modalities. However, the effect is significant only for real odors.

Stimulus to Percept

For each sensory modality presented to the larvae, we assume that the resulting percept (internal intensity representation of the odor) is proportional to relative changes in stimulus strength [25]. Thus, we assume that the perceptual response to the real odor, virtual odor, and temperature gradients will be of the form $f(\Delta C/\bar{C})$, where $\bar{C}$ is the background signal level (see eq. (22) below). The validity of this relationship has been established in adult flies [26], [27] and it appears to hold for larval olfactory sensory neurons (OSN) that respond to a normalized form of the stimulus derivative [23], [28]. Although this feature has not been explicitly shown for thermosensation, there is evidence that the behavioral response to an absolute change in temperature increases the larger the deviation from preferred background

temperatures [18]. It was shown further that this process is mediated by cross-inhibition between warming cells and cooling cells [29], activated by positive and negative temperature gradients respectively, and a model was developed to show that the relative contributions of each corresponding signal towards behavior increased as larvae moved away from preferred temperatures. In our experimental paradigm, this would imply that a temperature change of $\Delta C = 1^o\mathrm{C}$ at $T_{\max} = 30^o\mathrm{C}$ would trigger a stronger behavioral effect than an identical change of $\Delta C = 1^o\mathrm{C}$ at the preferred temperature $T_{\min} = 16^o\mathrm{C}$. We incorporate this perceptually in our agent-based model by rescaling the temperature signal as $C \leftarrow T_{\max} - C$. In our simulations, we compute the relative change in stimulus between two consecutive timesteps $n,\ n-1$ as the following:

$$s_n = \frac{C_n - C_{n-1}}{\bar{C}}. \tag{22}$$

We compute the background signal level as the midpoint between two timesteps, $\bar{C} = \frac{C_n + C_{n-1}}{2}$. To be able to compare signals from different sensory modalities and stimulus ranges, we define a gain G associated with each sensory modality that represents the perceptual sensitivity of larvae. The perceptual (internal) representation of an odor cue, for example, is modelled as:

$$s_{odor,n} = G_{odor} \frac{C_n - C_{n-1}}{\bar{C}}. \tag{23}$$

This quantity can be both positive and negative depending on the direction of the sensory gradient. As we do not explicitly model firing rates, we assume that this perceptual representation is encoded by different elements of the peripheral olfactory circuit of the larva. The exact mechanism is unknown; it is not accounted for in the agent-based model.

Cue Combination

Finally, we model the link between the sensory experience of the larva and its orientation behavior. The mode transitions and casting amplitudes of larva in our agent-based model are described as functions of a decision variable d_n, which is dependent on some combination of the sensory modalities perceived by the larva. In subsequent sections, all variables are computed at timestep n and we drop the subscript to avoid cluttered notation (e.g. we refer to the decision variable as $d \equiv d_n$). We describe the combination of the two different sensory modalities s_1, s_2 using the linear model:

$$d = w_1 s_1 + w_2 s_2, \tag{24}$$

where w_1, w_2 are weights associated with each cue. We hypothesize that larvae may have a bias for one sensory modality over another. Furthermore, we hypothesize that larvae are able to measure the reliability of individual signals when integrating multiple sources of information. We assume that the "reliability" of a sensory signal represented by a time series is inversely proportional to its variance σ^2 (see below). Thus, we test three different plausible weighting strategies:

1. Fixed Weights (FW):

$$w_1 = a \quad , \quad w_2 = 1 - a \tag{25}$$

2. Shut Weights (SW):

$$w_1 = \begin{cases} 1 & if\ \sigma_1^2 < \sigma_2^2 \\ 0 & if\ \sigma_1^2 \geq \sigma_2^2 \end{cases} \quad , \quad w_2 = \begin{cases} 0 & if\ \sigma_1^2 < \sigma_2^2 \\ 1 & if\ \sigma_1^2 \geq \sigma_2^2 \end{cases} \tag{26}$$

3. Variance Minimization (VM):

$$w_1 = \frac{\sigma_2^2}{\sigma_1^2 + \sigma_2^2} \quad , \quad w_2 = \frac{\sigma_1^2}{\sigma_1^2 + \sigma_2^2} \tag{27}$$

The first weighting strategy proposes that larvae combine cues with fixed preferences that are independent of the signal variance. The latter two strategies imply that larvae are also able to adapt their response according to the estimated variance of the sensory inputs, which has been demonstrated in previous studies [17]. The SW strategy assumes that larvae place absolute priority on the cue that is observed to be more reliable. The VM strategy is based on the optimal linear combination rule for minimizing the variance of the combined signal, given certain assumptions [7]. In the SW and VM models, we assume the larva accumulates sensory evidence over some time window as it navigates the environment and uses this to estimate the variability of each sensory modality. For simplicity, we assume that the variance is estimated through sampling as

$$\sigma^2 = \frac{1}{\tau} \sum_{i=n-\tau}^{n} (s[i] - \mu)^2, \tag{28}$$

where μ is the sample mean, and τ is the time sampling window, which was estimated as $\tau = 11s$ for *Or42a* OSN activation and was shown to be similar in duration for other sensory modalities [17]. In the case of a real odor whose concentration is below the detection threshold, the odor would not be perceived as being present and hence the variance σ would be assumed to be infinite. This equation assumes that larvae integrate both the temporal variance of the sensory signal itself and self-motion induced spatial fluctuations due to continuous head casting. While it has been suggested that larvae may be able to filter sensory inputs in sync with the frequency of its own peristaltic motion [17], it is unknown how this filtering adapts to motion as the rhythm of head casting is variable and not strictly coupled to peristalsis [21]. Given that it is a weighting of the variances of both channels as

ratios that is used to compute cue weights, we assume that the distortions in the estimated variation due to head casting are negligible compared to the true temporal variance of the sensory signal.

Variance Minimization

For model 3, the decision rule maximizes the reliability of the combined sensory modalities, with the assumption that both gradients originate from a single source [7]. Let s_1 and s_2 denote the observed cues for attraction from two different gradients, which can be congruent (if the two signs coincide, or incongruent, if the two signs are different). We assume that larvae associate the hedonic value of both gradients in an overall level of attraction, which we denote as z. To decide whether to continue in a given direction of motion (heading) or to reorient, larvae infer the latent variable z from the observed cues s_1 and s_2. The optimal estimate of the source of attraction z can be obtained by applying Bayes rule:

$$p(z \mid s_1, s_2)p(s_1, s_2) = p(s_1, s_2 \mid z)\, p(z). \tag{29}$$

Given that s_1 and s_2 are independent cues as their fluctuations are driven by different physical processes affecting distinct sensory modalities (we neglect joint odor fluctuations due to turbulence, as our assay is far from that regime), we have:

$$p(z \mid s_1, s_2)p(s_1)p(s_2) = p(s_1 \mid z)p(s_2 \mid z)\, p(z). \tag{30}$$

Since $p(s_1)$ and $p(s_2)$ do not depend on z, the variable of interest, we can treat them as proportionality constants:

$$p(z \mid s_1, s_2) \propto p(s_1 \mid z)p(s_2 \mid z)p(z). \tag{31}$$

In addition, we assume that the prior $p(z)$ is flat at every time step, as experiments are performed in an environment that is new to the larvae and there is no evidence that larvae can form spatial memory from previous time steps. We assume that the cues s_1 and s_2 are normal random variables with variances σ_1^2 and σ_2^2. To obtain the optimal estimate of the source of attraction, we calculate the value of z that maximizes the posterior probability (maximum a posteriori estimate):

$$\begin{aligned} &\underset{z}{\operatorname{argmax}}\, p(z \mid s_1, s_2) = \frac{d}{dz}\, ln\, [p(s_1 \mid z) p(s_2 \mid z)\,] = \\ &\frac{d}{dz}\, ln \left[e^{-\frac{(s_1 - z)^2}{2\sigma_1^2}} e^{-\frac{(s_2 - z)^2}{2\sigma_2^2}} \right] = \frac{2(s_1 - z)}{2\sigma_1^2} + \frac{2(s_2 - z)}{2\sigma_2^2} = 0. \end{aligned} \tag{32}$$

Rearranging, we have:

$$z = \frac{\left(\frac{1}{\sigma_1^2}\right) s_1 + \left(\frac{1}{\sigma_2^2}\right) s_2}{\left(\frac{1}{\sigma_1^2}\right) + \left(\frac{1}{\sigma_2^2}\right)} = \frac{\sigma_2^2}{\sigma_1^2 + \sigma_2^2}\, s_1 + \frac{\sigma_1^2}{\sigma_1^2 + \sigma_2^2} s_2 \tag{33}$$

Reward Maximization

An alternative strategy without assuming a common origin of the two sources is to maximize the expected reward by following each of the two gradients, where reward is defined as the probability that the larva is moving up-gradient. We use the same assumption that the cues s_1 and s_2 are Gaussian random variables with variances σ_1^2 and σ_2^2. Given any trajectory, the probability that the larva is travelling up-gradient for each of two modalities is $\Phi\left(\frac{s_1}{\sigma_1}\right)$ and $\Phi\left(\frac{s_2}{\sigma_2}\right)$, where

$$\Phi(x) = \frac{1}{\sqrt{2\pi}} \int_{-\infty}^{x} e^{-\frac{x^2}{2}} dx \,, \tag{34}$$

is the standard normal cumulative density function. Assuming that there is an equal preference for reaching either source, the reward of continuing at the current heading is the sum of the probabilities of travelling up-gradient in each of the two sources

$$z = \Phi\left(\frac{s_1}{\sigma_1}\right) + \Phi\left(\frac{s_2}{\sigma_2}\right). \tag{35}$$

Conversely, the reward of stopping and reorienting is

$$z' = \left(1 - \Phi\left(\frac{s_1}{\sigma_1}\right)\right) + \left(1 - \Phi\left(\frac{s_2}{\sigma_2}\right)\right). \tag{36}$$

The optimal decision that maximizes reward is therefore to continue at the current heading if $z > z'$, and to reorient otherwise. We implement this at the motor level in the agent-based model by defining the decision variable as the reward $d = \Phi\left(\frac{s_1}{\sigma_1}\right) + \Phi\left(\frac{s_2}{\sigma_2}\right)$, so that the agent will have a low probability of stopping if d is large, and will have a high probability of stopping in the opposite case.

Comparing $p = 1$ (Reward-Maximization) and $p = 2$ (Variance-Minimization) rules

To compare these two strategies, we make several approximations. For maximizing reward, we make the following approximation given $\sigma_1 \gg s_1$ and $\sigma_2 \gg s_2$,

$$d = \Phi\left(\frac{s_1}{\sigma_1}\right) + \Phi\left(\frac{s_2}{\sigma_2}\right) \approx \frac{s_1}{\sigma_1} + \frac{s_2}{\sigma_2}. \tag{37}$$

The $p = 1$ rule corresponds to Reward Maximization. For maximizing reliability, we obtain a different decision variable, namely

$$d = \frac{\sigma_2^2}{\sigma_1^2 + \sigma_2^2} s_1 + \frac{\sigma_1^2}{\sigma_1^2 + \sigma_2^2} s_2 \tag{38}$$

$$\propto \frac{\sigma_1^2+\sigma_2^2}{\sigma_1^2\sigma_2^2}\left(\frac{\sigma_2^2}{\sigma_1^2+\sigma_2^2}\, s_1 + \frac{\sigma_1^2}{\sigma_1^2+\sigma_2^2} s_2\right) = \frac{s_1}{\sigma_1^2} + \frac{s_2}{\sigma_2^2}.$$

The combination rule with $p = 2$ corresponds to Variance Minimization. In general, we can embed both rules into a single rule with free parameter p as

$$d = \frac{\sigma_1^p+\sigma_2^p}{\sigma_1^p\sigma_2^p}\left(\frac{\sigma_2^p}{\sigma_1^p+\sigma_2^p}\, s_1 + \frac{\sigma_1^p}{\sigma_1^p+\sigma_2^p} s_2\right) = \frac{s_1}{\sigma_1^p} + \frac{s_2}{\sigma_2^p}. \quad (39)$$

In our simulations, we will optimize the free parameter p, as well as compare the $p = 1$ and $p = 2$ rules. We propose to call p the *bimodal-contrast parameter*.

Noise

As we propose that larvae are sensitive to the variance of sensory inputs, an important aspect of this model is to account for noise in the sensory signal. We model noise as Gaussians η with zero-mean. For generalizability, we consider noise added at several stages of the flowchart (Figure 1E):

1. Additive external sensory noise: $C_n + \eta_{ext}$
2. Additive internal sensory noise: $s_n + \eta_{int}$
3. Decision noise: $d + \eta_d$

The first is additive external noise η_{ext} that does not scale with the sensory input. This may be more prominent in experimental paradigms with virtual odor gradients for example, where the noise might result from fluctuations in the action of the LED light on the light-gated ion channel (Chrimson [30]). The fixed amplitude light flashes used to perturb the larvae in experimental paradigms with noise can be also modelled with this approach.

The second is additive internal sensory noise η_{int} due to the assumption that larvae perceive relative changes in stimulus in the agent-based model. Noise that scales with the sensory input would be more plausible for experimental paradigms with real odors, as the

fluctuations in odorant molecules tend to fluctuate according to a Poisson distribution, resulting in noise that is dependent on odor concentration.

The third is decision noise, which models the inherent stochasticity of larvae behavior in its mode transitions and variability in casting amplitudes. In our model, we have found similar predictions when incorporating all levels of noise (1 + 2 + 3) and the reduced scheme (2 + 3). While the quality of the predictions may change, we find that the hierarchy of the performance of the weighting strategies does not change with the variations in the framework. This is illustrated in the comparison of AIC and BIC in Figure 2F.

Optimization Framework

Below is a list of constants used to model larva motion in the simulations:

Parameter		Value
Run velocity	v	1.3 mm/s
Larva length	l	3.86 mm
Run transition constant	c_{run}	1.46
Stop transition constant	c_{stop}	0.16
Maximum casting amplitude during runs	$\theta_{M,run}$	0.75 rad/s
Maximum casting amplitude during stops	$\theta_{M,stop}$	2.93 rad/s
Variance sampling time window	τ	11 s

Decision noise	η_d	0.32

Table 1: Constant parameters in the agent-based model

These parameters model the movement patterns of foraging 3rd instar larvae in the absence of any stimulus recorded at high spatio-temporal resolution with the closed-loop tracker from ref. [23], and are assumed to be constant across all experimental conditions. The run velocity v and larva length l were chosen to match the mean observed in wildtype w^{1118} larva (n = 100 larvae). The parameters c_{run}, c_{stop}, $\theta_{M,run}$, $\theta_{M,stop}$, and η_d were fit using maximum likelihood estimation as illustrated in Figure 2A-D. The variance sampling time window τ was estimated based on the timescale of variance adaptation in [17].

For each experimental paradigm, there are four free parameters associated with each of the two sensory modalities (unimodal conditions):

- η_{int}: Internal additive noise
- G: Perceptual gain
- γ: Sensitivity to Turning
- β: Sensory threshold

Each experimental paradigm has a unimodal condition with each sensory modality presented independently and then a bimodal condition with both sensory modalities presented at the same time. Our approach is to use the data from the unimodal conditions to fit the free parameters of our model, and then use the data from bimodal conditions to evaluate the goodness of fit of the different weighting strategies. Therefore, there are a total of eight free parameters for each experimental paradigm – one set of four parameters for each unimodal condition. We consider the signal and noise of each sensory modality regardless of the test condition (unimodal, bimodal), but we assume that the signal-to-noise

ratio is what allows the larva to determine whether a stimulus is present or whether the larva is only perceiving white noise.

To evaluate the goodness of fit of our models, we compared the preference index and the spatial distributions between the experimental data and the simulation.

- **Preference Index:** The preference index (PI) is the fraction of larvae on the preferred side of the arena. The error in the preference index is given by computing the mean squared error between the simulated PI and the experimental PI at different intervals over the course of the experiment.
- **Spatial Distribution:** We use the Kullback-Leibler (KL) divergence to compare the error between the simulated and experimental spatial distributions over the entire course of the experiment. The X and Y dimensions are considered separately when computing the KL divergence.

Because the preference index only measures the fraction of larvae that are on the preferred side of the arena, we find that the spatial distributions give a more accurate representation of the quality of fit. All parameter fitting was performed using the Global Optimization Toolbox in MATLAB.

Simulating Wall (Boundary) Conditions

Since the arena is small, one last component of our model is accounting for larvae behavior at the edges for the arena. We noted that a significant fraction of larvae remained close to the arena boundary (its wall), particularly in conditions with a linear temperature gradient. We considered several possibilities if a larva's path is obstructed by the arena wall (Figure 1D):

1. The larva remains stationary in a stopping state as long as its position at the next timestep is outside the bounds of the arena.

2. The larva moves tangent to the edge of the arena at a velocity $v_{edge} = \cos(\psi)\, v$, where v is the larva's original speed, and ψ is the angle between the larva's heading direction and the direction tangent to the arena.
3. The larva "bounces" off the edge of the arena at the angle of incidence (ballistic collision model).

Through numerical simulations, we found that the first approach is the closest representation of the behavior observed in our experimental data based on the stopping statistics of larvae at the boundary.

Fraction-at-Source and Reward Metrics

The *"Fraction at Source"* is defined as the number of larvae within bounded regions near the peak of the gradients divided by the total number of larvae:

$$\text{Fraction at Source} = \frac{N_{cue}}{N_{cue}+N_{nocue}}. \quad (40)$$

For odor configurations, this bounded region is defined as an area within radius r of the source. For temperature configurations, the bounded region associated with the comfortable (targeted) temperature is any location $x < r$, where $x = 0$ corresponds to the leftmost, coolest side of the arena. The radius r was chosen such that the areas of the bounded regions were identical for both odor and temperature configurations ($r = 1.8cm$). The *"reward"* for each sensory modality is defined as the mean perceived sensory experience of all larvae relative to the peak sensory experience in the arena. In the bimodal condition, the reward is calculated as the average reward across both sensory modalities. For N_j number of sensory modalities, the reward is given by:

$$\text{Reward} = \frac{1}{N_j}\sum_{j=1}^{N_j}\frac{C_{\text{mean},j} - C_{\text{min},j}}{C_{\text{max},j} - C_{\text{min},j}}, \tag{41}$$

where $C_{\text{mean},j}$ is the mean sensory experience of all larva for sensory modality j, while $C_{\text{min,j}}$ and $C_{\text{max,j}}$ denote the least and most preferred sensory experience in the arena respectively for sensory modality j.

Model Selection with AIC/BIC

The prediction error for the AIC/BIC [31], [32] was computed for the Variance Minimization rule across all bimodal experimental paradigms:

$$\begin{aligned} AIC &= 2k - 2\ln(\hat{L}) \\ BIC &= k\ln(N) - 2\ln(\hat{L}). \end{aligned} \tag{42}$$

Where k is the number of model parameters, N is the number of simulated larvae for each experimental paradigm, and $\hat{L}$ is the likelihood function given the actual observed spatial distributions of larvae. In each model variant, one component of the model was added/removed, and the model parameters were re-optimized. The resulting prediction error was then compared to that of the final model. All variations of the model resulted in a higher prediction error, as shown in Figure 2F.

Results

An experimental assay to quantify multisensory combination in the larva

A behavioral assay was developed to study larval navigation in spatial gradients of temperature, a real odor, and a virtual odor induced optogenetically by expressing Chrimson in genetically-targeted olfactory sensory neurons (OSNs). Red light elicited virtual-odor stimulations in the *Or67b*-expressing OSN which is not activated by ethyl butyrate [33], [34]., the real odor used in this study. As a result, the real and virtual odor activated a distinct and independent set of OSNs. In each experiment, larvae at the third developmental instar were uniformly distributed in groups of 10 individuals near the center of a circular behavioral arena coated with agarose (Figure 3A). The motion of the group of larvae was video-monitored during exposure to single or combined sensory gradients. The trajectories of larvae in the arena were then extracted using a custom image processing and tracking software. Larvae were analyzed individually as, given the low density of animals, group effects were found to be negligible in the context of these gradients (see 'Materials and methods').

In conditions where single gradients were presented, which we will refer to as unimodal conditions, larvae navigate unimodal odor, virtual-odor, and temperature gradients by locating the "source": the region associated with the highest concentration of the attractive odor or the most comfortable temperature in the arena. When placed near the center of the arena, larvae innately navigated to the location of highest odor concentration, highest virtual-odor intensity, or the location with the most preferred temperature, which was slightly higher than 16^{o}C in our experimental conditions (Figure 3B). In the range of

temperatures used in the present work, larvae demonstrated robust thermotaxis down temperature gradients toward the coolest region of the arena.

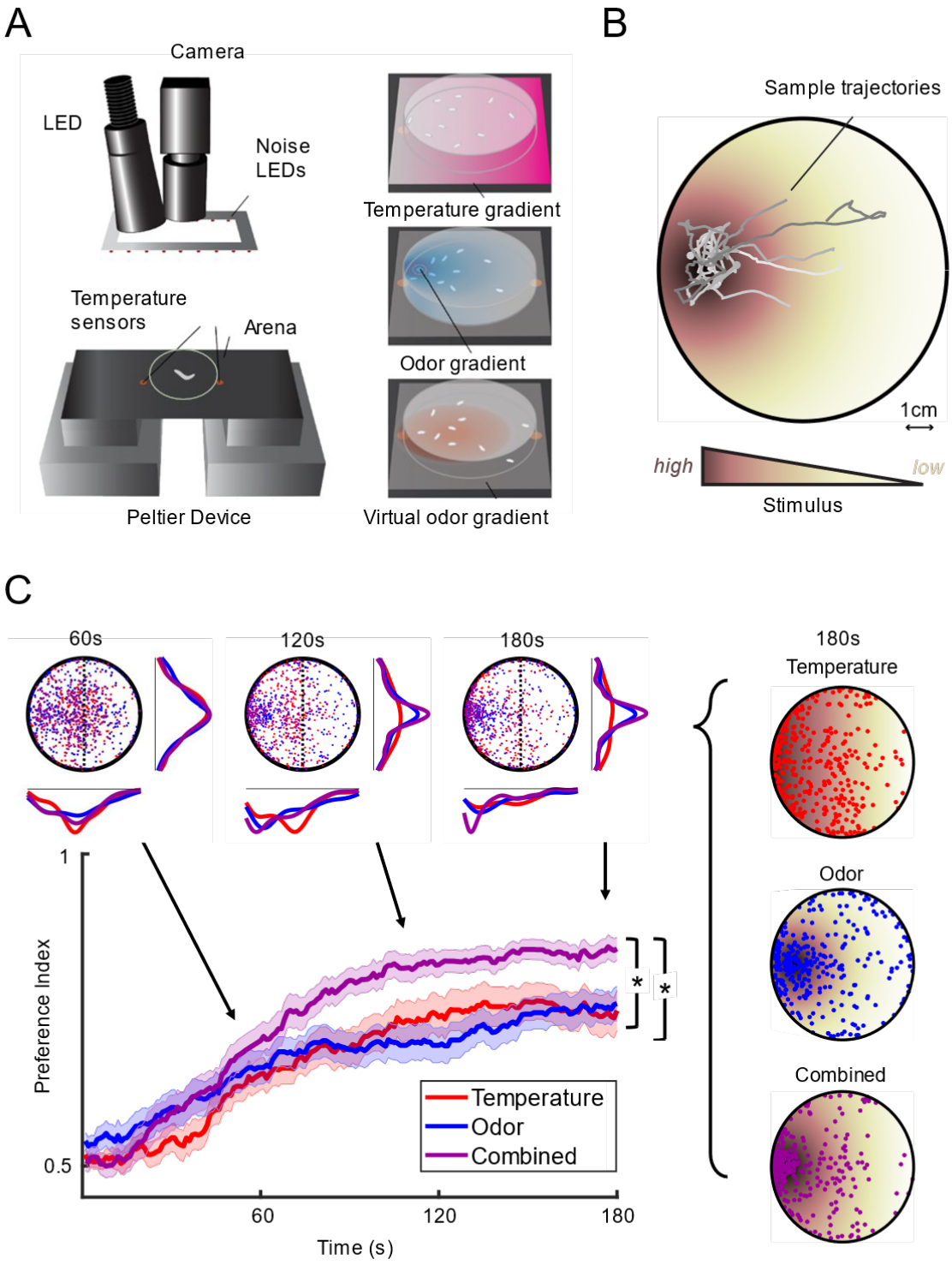

Figure 3: Assay to identify how larvae navigate unimodal (single) and bimodal (combined) gradients. (A) Schematic of the behavioral assay, which features gradients of

real odor, optogenetically-induced virtual odor, and temperature. **(B)** Representative trajectories of third-instar wild-type (w^{1118}) larvae responding to the combination of an odor and a temperature gradient over a period of 3 minutes. **(C)** Behavioral response of wild-type larvae to the individual odor and temperature gradients and both odor and temperature combined (Odor: Ethyl butyrate, 10^{-3} M; Temperature range: 16-30^{o}C). Larvae were tested in groups of 10 individuals (Odor: n = 27 groups of 10 larvae; Temperature: n = 35; Combined: n = 27). In all subsequent figures, the shaded regions around the preference index curves represent the error bars of the SEM. The asterisks indicate that the preference index of the combined condition was significantly higher than the preference indices of either unimodal condition (after the first minute of the experiment), as assessed using a *t*-test ($p < 0.025$ upon Bonferroni correction). Also illustrated are the overlayed spatial distributions of larvae for each condition at 60, 120, and 180 s (top), and the spatial distributions for each individual condition at 180 s (right).

In situations where two gradients are presented at the same time, which we will refer to as bimodal conditions, we initially arranged the gradients in congruent configurations such that both sources were on the same side of the arena with colinear gradients. At the start of the experiment, larvae were placed near the center of the arena and over time distributed in a way similar to the unimodal conditions. Notably, larvae in bimodal conditions demonstrated improved performance in navigating towards the congruent sources compared to the unimodal conditions. For example, the attraction towards the source increased upon combination of an odor and a temperature gradient (Figure 3C). This result is quantified by the preference index, which is the fraction of larvae on the targeted side of the arena (i.e. odor source or preferred temperature) as a function of time:

$$PI(t) = \frac{N_{cue}(t)}{N_{cue}(t) + N_{nocue}(t)} \tag{43}$$

Sluggish larvae displaying an average speed lower than 0.1 mm/s are excluded from the preference index calculation to avoid counting inactive outliers sitting near the starting location. For convenience of notation, we omit the time variable t and simply refer to the preference index as the PI in the rest of the text. We observed a similar improvement in preference index across all other experimental paradigms with congruent gradients of two distinct odors, a real odor and a virtual odor, as well as a virtual odor and temperature (Figure 4, Figure 5).

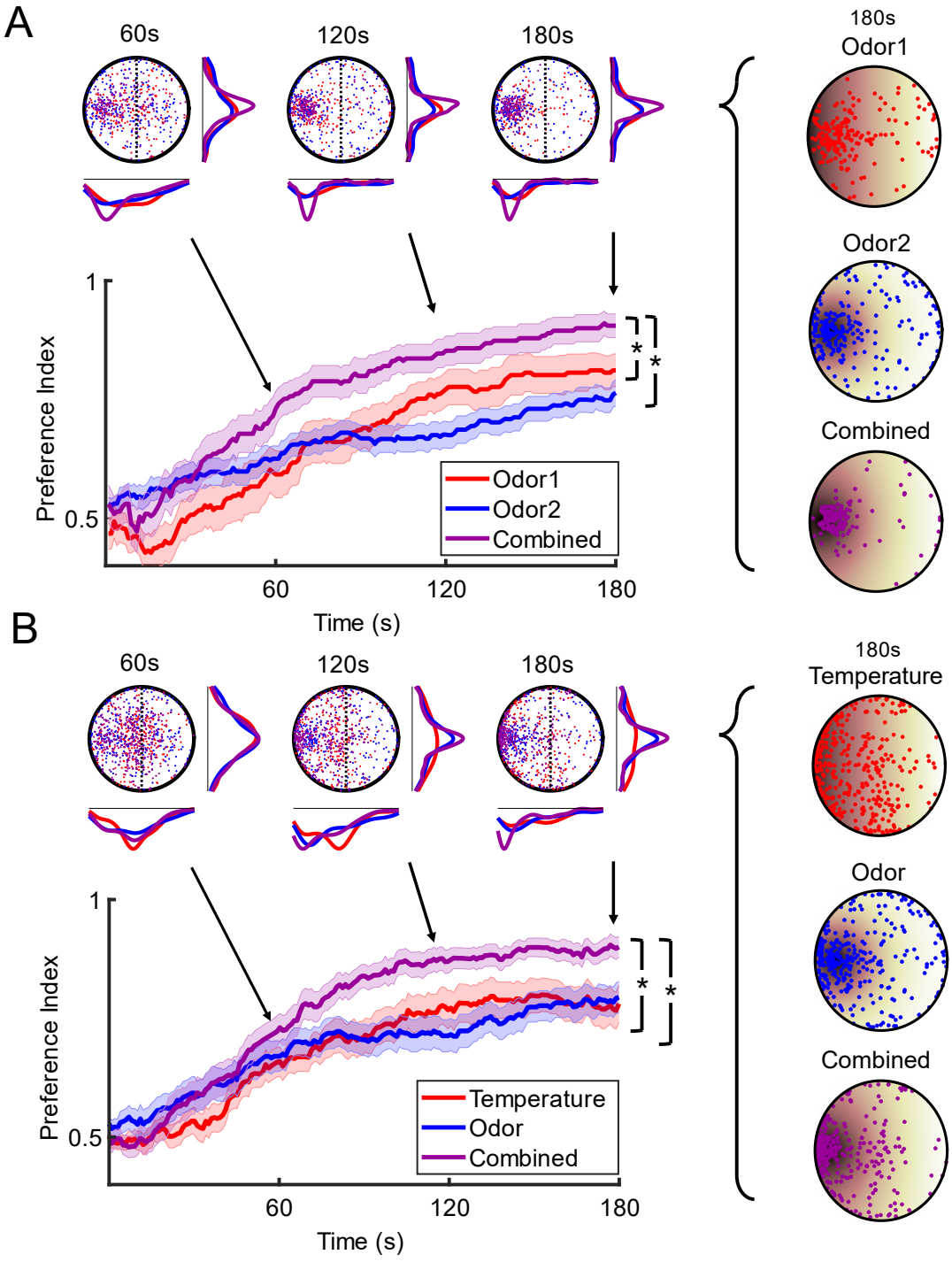

Figure 4: Preference indices corresponding to the performances of wild-type larvae for congruent gradients: odor + odor and odor + temperature. When two congruent

unimodal gradients are combined, the final preference index is significantly higher than the preference indices of either unimodal condition as indicated by the asterisks (t-test with Bonferroni correction, $p < 0.025$). The shaded regions around the preference index curves indicate the error bars of the SEM. **(A)** Odor + odor (odor 1: 1-hexanol, 10^{-2} M, n = 20 groups of 10 larvae; odor 2: ethyl butyrate, 10^{-3} M, n = 26; combined: n = 19). **(B)** Temperature + odor (odor: ethyl butyrate, 10^{-3} M, n = 27; temperature: 16-30ºC, n = 35; combined: n = 27).

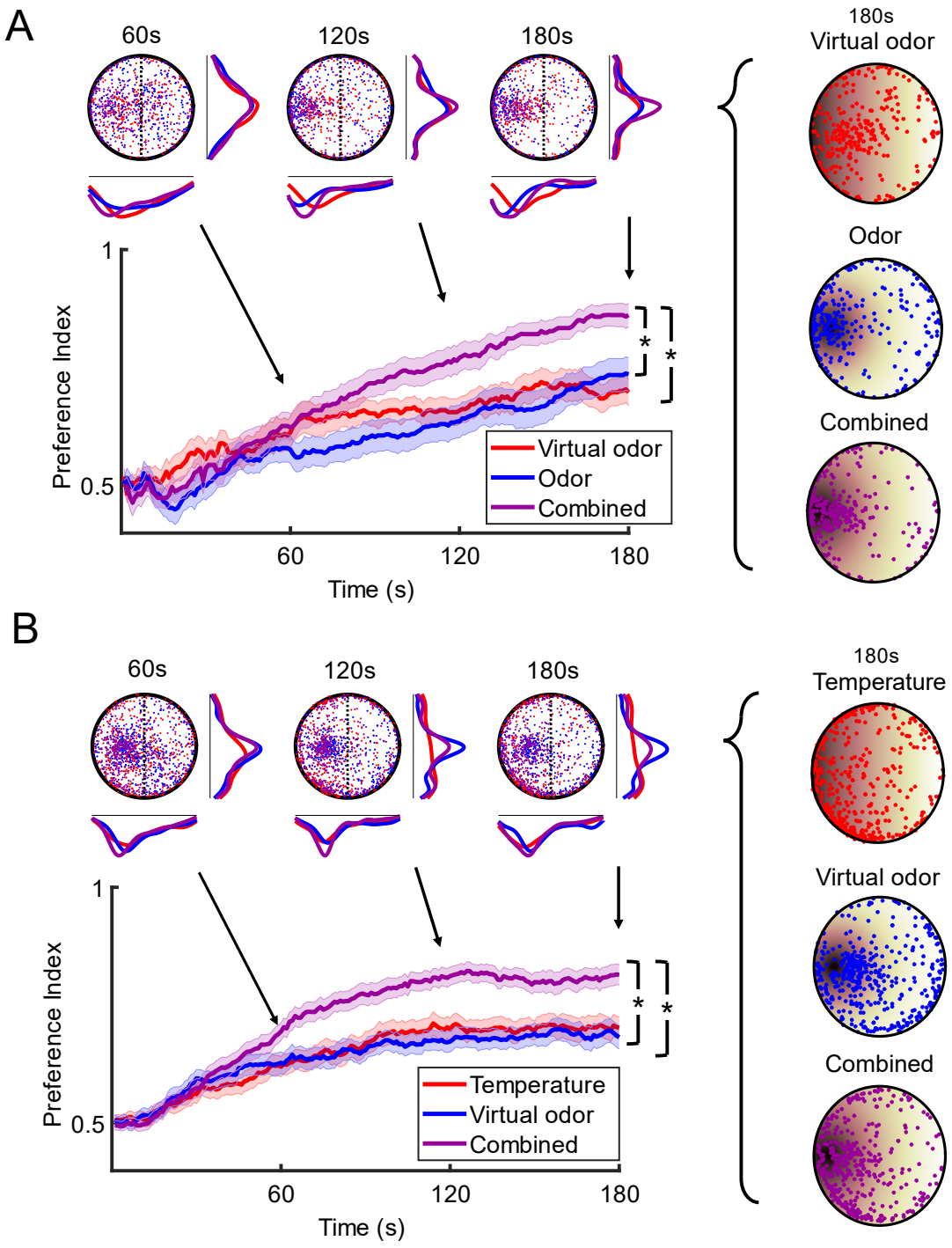

Figure 5: Preference indices corresponding to the performances of wild-type larvae for congruent gradients: virtual odor + odor and virtual odor + temperature. When two

congruent unimodal gradients are combined, the final preference index is significantly higher than the preference indices of either unimodal condition as indicated by the asterisks (*t*-test with Bonferroni correction, $p < 0.025$). **(A)** Virtual odor + odor (virtual odor: *Or67b*>Chrimson, light 625nm, n = 30; real odor: ethyl butyrate, 2.5 x 10^{-4} M, n = 30; combined: n = 30). **(B)** Temperature + virtual odor (virtual odor: *Or42a*>Chrimson, n = 49; temperature: 20-40ºC, n = 49; combined: n = 49).

A coarse-grained model suggests that larvae account for cue uncertainty when combining multimodal cues

To characterize how heightened attraction emerges from the combination of olfactory and thermosensory cues in congruent gradients, we started by developing a parameter-free theoretical model using the principle of Bayesian inference to estimate the probability distribution of the positions of individual larvae in the arena (see section Parameter-Free Model in Materials and Methods). The model predicts that the weighting of the information from different gradients is dependent on the uncertainty associated with each gradient. As described in the Materials and Methods, this coarse-grained model estimates the PI of the response to the combined-gradient condition based on the PI of the corresponding unimodal conditions PI_1 and PI_2:

$$PI_{1+2,Model} = \frac{PI_1 \times PI_2}{PI_1 \times PI_2 + (1 - PI_1) \times (1 - PI_2)}. \quad (44)$$

As shown in Figure 6B, we found that the parameter-free model reproduces the behavioral improvement observed in the experimental preference index for the congruent temperature and odor gradient presented in Figure 3C. In addition, we applied the parameter-free model to predict the behavior of larvae tested in congruent gradients

featuring two real odors (Figure 6A), a real and a virtual odor, a real odor and temperature, or a virtual odor and temperature (Figure 6B-D). In all four experimental conditions, the results of the model were in excellent qualitative agreement with the behavior elicited by congruent bimodal gradients, suggesting that real larvae use probabilistic inference to combine sensory information.

Building an agent-based model to characterize how the combination of sensory cues directs navigation

To analyze the plausibility of different mechanisms of sensory combination and dissect the control of individual reorientation maneuvers, we developed an agent-based model that offers a more realistic description of larval navigation in response to both unimodal and bimodal conditions (Figure 7A). The starting point of our agent-based model is an existing mechanical model of chemotaxis in the *Drosophila* larva [21], which provides a general framework for describing orientation ("taxis") behavior elicited by unimodal stimuli. Based on evidence that larvae display continuous lateral oscillations of the anterior body segment during peristalsis, the agent-based model established that a direct sensory modulation of the oscillation amplitude of head-casts could reproduce many signatures of chemotaxis observed in larvae.

$$PI_{1+2,\,Model} = \frac{PI_1 PI_2}{PI_1 PI_2 + (1 - PI_1)(1 - PI_2)}$$

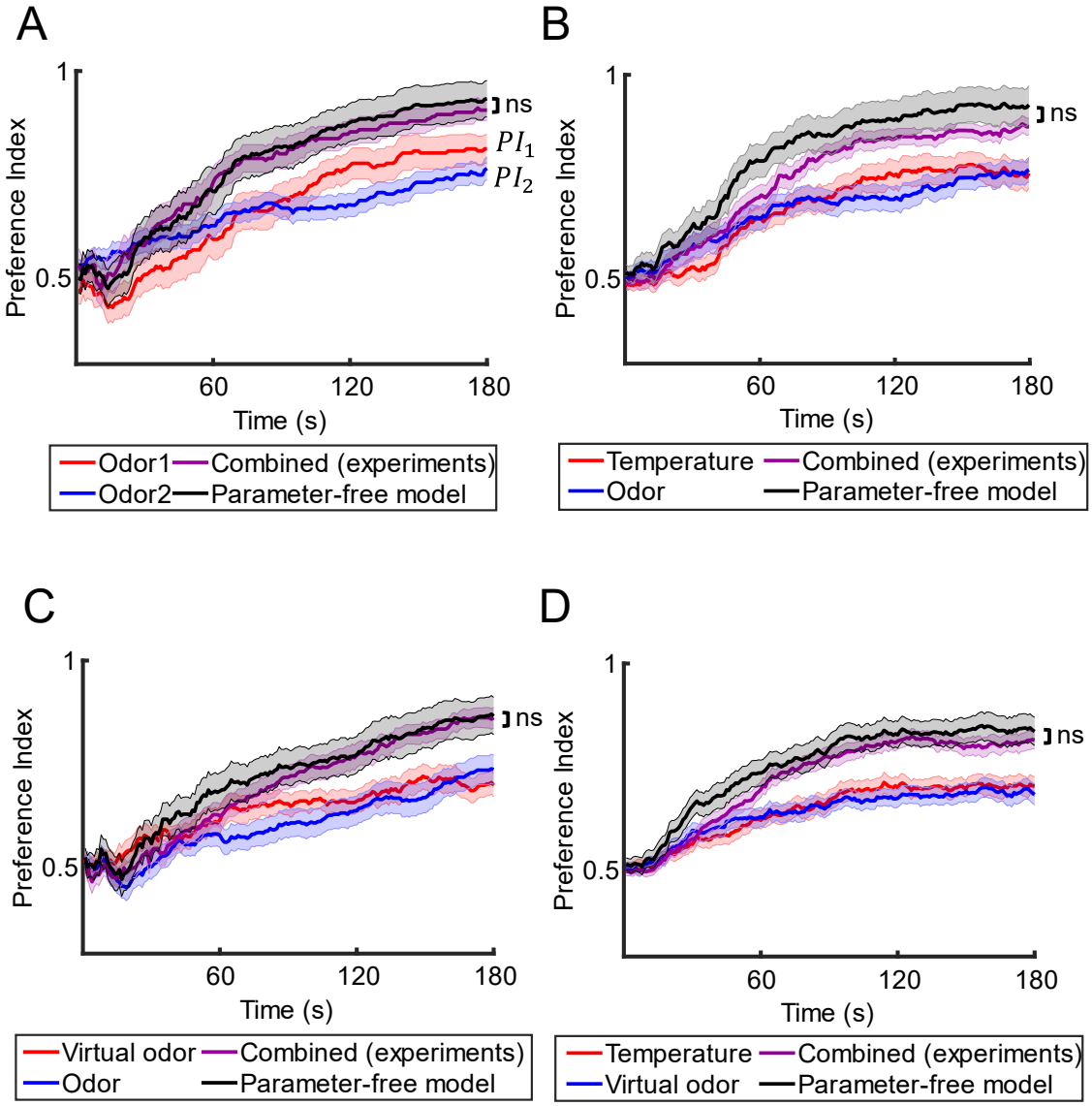

Figure 6: Comparison of the combined preference indices of wild-type larvae with predictions from a parameter-free model for the four configurations outlined in Figure

4 and Figure 5. In all configurations (A-D), there is no significant difference between the final preference indices of the experimental data and the parameter-free model (*t*-test, $p > 0.05$).

As detailed in the Agent-based Model section of the Materials and Methods, we adapted the model of Wystrach et al. [21] based on the quantification of our behavioral data to account for a multimodal setting by capturing more closely how different sensory gradients are perceived by the larva, and then by modelling how graded information from two different sensory modalities are combined to drive reorientation maneuvers. In our expanded agent-based model, *Drosophila* larvae alternate between straight runs and directed turns. The alternation between these two behaviors is modulated by the detection of temporal increases or decreases in sensory input. Active sensing is achieved primarily through lateral movements of the head, which assesses the local environment to reorient toward the direction of the gradient. To achieve a realistic representation of the sensorimotor control of larval navigation, we incorporated behavioral mechanisms to describe both how larvae determine *when* to initiate a turn and *where* to turn to.

In the model developed here (Figure 1), the larva is represented as a single segment from its midpoint to its head — the body segment from the tail to the midpoint is assumed to passively follow the head segment, which is reasonable in first approximation. The agent-based larva may be in one of the following two states: running, where the larva moves at a fixed speed in the direction of its head segment while making small adjustments to its heading, and stopping, where the body segment is stationary but the body segment is free to rotate around the midpoint. The behavioral state of the agent-based larva is updated in discrete time steps. At each time step, the head segment alternates between rotations on the

left and the right side of the body axis to mimic the active sampling of sensory conditions surrounding the head. At any given timestep n, the larva perceives the sensory input C_n given by the intensity of the stimulus detected at the tip of the head segment where the olfactory organs are located.

In each experimental paradigm, we simulated the behavior elicited by combinations of real-odor gradients with static virtual-odor gradients or static temperature gradients (Figure 7B). While the profiles of the virtual-odor gradients created with a LED and temperature gradients created with a Peltier element were stationary, the real-odor gradients were created by placing an odor droplet on the side of the source. To simulate the dynamics of the odor gradient during the course of an experiment, we used a biophysical model for the odor diffusion introduced in previous work [23] (see Sensory Stimulus section of the Materials and Methods).

For each sensory modality presented to the larva, we hypothesized that the resulting percept —the internal representation of the odor— is proportional to relative changes in stimulus strength [25]. More specifically, the model assumes that the perceptual response to the real-odor, virtual-odor, and temperature gradients will be of the form $f(\Delta C/\bar{C})$, where $\bar{C}$ is the background signal level and ΔC is the signal difference (Figure 7C). This sensory property is equivalent to Weber law, which has been established in the peripheral olfactory system of the adult fly [26], [27], [35]. We assume that the larval olfactory system detects relative changes in odor concentration, which is supported by the response properties of larval OSNs [23], [28] and the apparent concentration-invariance of reorientation maneuvers [28]. For temperature, we make the assumption in our agent-based model that the larva perceives relative changes zeroed at the maximum temperature of the behavioral assay (i.e.

$C \leftarrow T_{\max} - C$). This results in a perceptual response that increases as larvae move away in a temperature gradient from preferred temperatures. Although the sensitivity of the thermosensory system to relative changes has not been explicitly demonstrated, there is evidence that the magnitude of the behavioral response scales with the difference in temperature relative to the deviation from preferred background temperatures [18], [29]. In our simulations, we computed the relative change in stimulus between two consecutive timesteps $n-1$ and n as the following variable:

$$s_n = \frac{\Delta C}{\bar{C}} = \frac{C_n - C_{n-1}}{\bar{C}}. \tag{45}$$

The background signal level $\bar{C}$ is computed as the midpoint between two timesteps, $\bar{C} = \frac{C_n + C_{n-1}}{2}$. At every time step of the stimulations, the information collected by the two different sensory modalities s_1 and s_2 is combined in a decision variable d by using the linear model:

$$d = w_1 s_1 + w_2 s_2, \tag{46}$$

where w_1 and w_2 are weights associated with each cue. Using the model, we examine the three most common weighting strategies, each representing a qualitatively different approach to cue combination:

4. Fixed Weights (FW):

$$w_1 = a \quad , \quad w_2 = 1 - a \tag{47}$$

5. Shut Weights (SW):

$$w_1 = \begin{cases} 1 & if\ \sigma_1^2 < \sigma_2^2 \\ 0 & if\ \sigma_1^2 \geq \sigma_2^2 \end{cases} \quad , \quad w_2 = \begin{cases} 0 & if\ \sigma_1^2 < \sigma_2^2 \\ 1 & if\ \sigma_1^2 \geq \sigma_2^2 \end{cases} \tag{48}$$

6. Variance Minimization (VM):

$$w_1 = \frac{\sigma_2^2}{\sigma_1^2 + \sigma_2^2} \quad , \quad w_2 = \frac{\sigma_1^2}{\sigma_1^2 + \sigma_2^2} \tag{49}$$

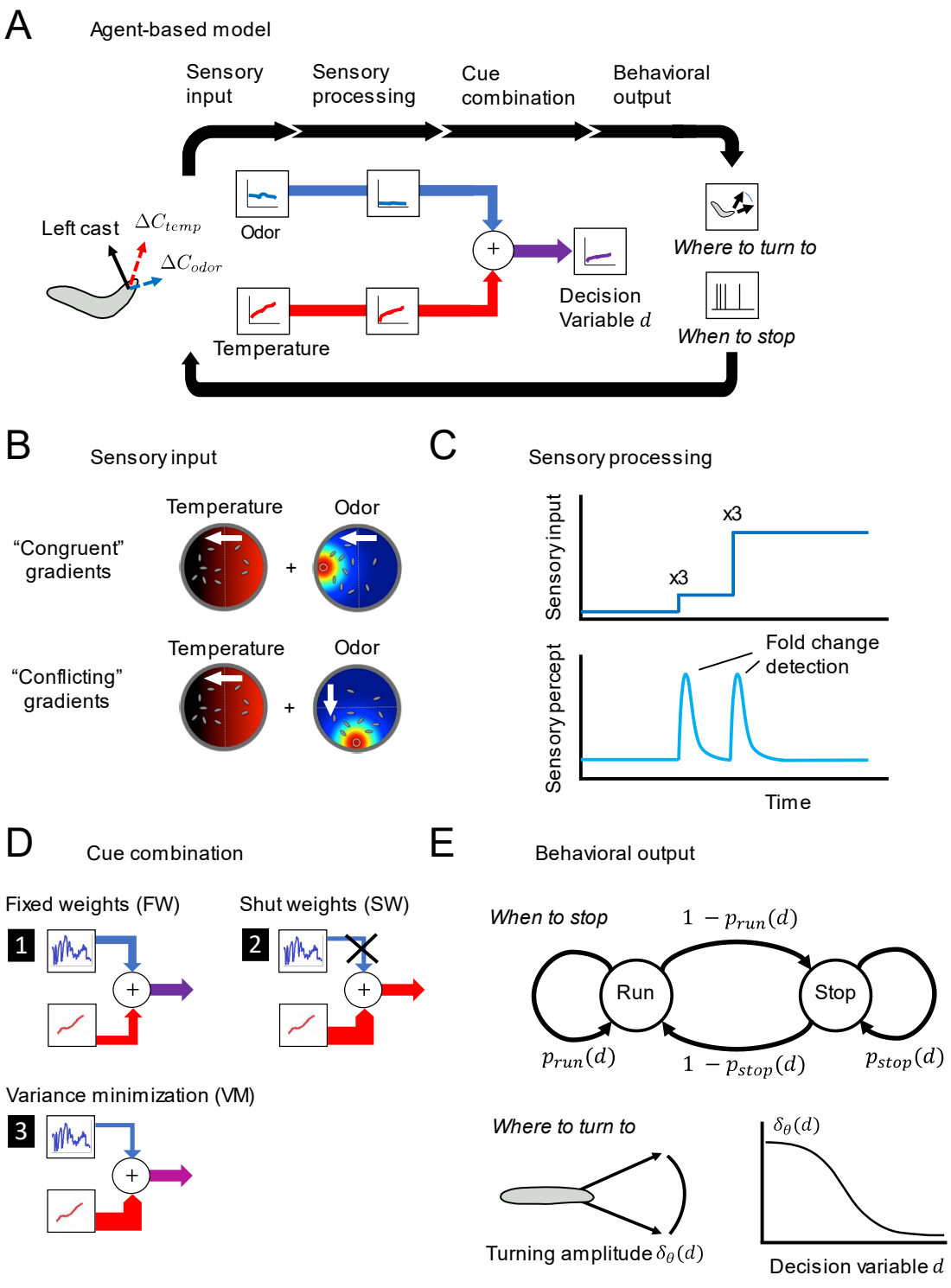

Figure 7: Outline of agent-based model for *Drosophila* larval navigation and set of plausible cue-combination models. (A) The different stages of the agent-based model are

represented in a flowchart from sensory input to behavioral output. The illustration depicts the sensory experience during a left head cast in an odor and a temperature gradient. (B) Gradients presented in each experimental paradigm can be congruent (co-linear) or conflicting (90-degree angle). (C) Sensory inputs are processed individually with the assumption that the resulting perceptual cue is proportional to relative changes in stimulus strength. (D) The perceptual cues from each sensory modality are combined as a weighted linear combination, with weights dependent on the cue combination rule. (E) The decision variable determines the amplitude of head casts $\boldsymbol{\delta_\theta}$ ("where to turn to") and the probability of mode transitions $\boldsymbol{p_{run}}$, $\boldsymbol{p_{stop}}$ ("when to stop") of the agent larva.

The Fixed-Weights (FW) strategy [36] proposes that larvae combine cues with fixed preferences that are independent of the signal variances σ_1^2 and σ_2^2. The latter two strategies imply that larvae are also able to adapt their response according to the estimated variance of the sensory inputs accumulated over a time window (for numerical implementation, see Materials and Methods), as established in a previous study [17]. Being sensitive to the reliability of sensory inputs is a hallmark of probabilistic inference, a powerful form of computation when dealing with inputs subject to sensory uncertainty. The Shut-Weights (SW) also known as Winner-Take-All strategy [37], [38] assumes that larvae place absolute priority on the cue that is observed to be more reliable and suppresses the weakest one. The Variance-Minimization (VM) strategy is a linear combination rule that minimizes the variance of the combined signal [7]. By considering the validity of these three cue-combination strategies for different sensory modalities, we can examine whether variance adaptation is present, and then test the degree to which variance modulates cue combination of multimodal signals.

Finally, the transition rates between the two states, running p_{run} and stopping p_{stop}, ("*when to stop*") and the amplitude of head casts δ_θ ("*where to turn to*") are described as

functions of the decision variable d using a generalized linear model (Figure 7E). The transition probabilities between states and the amplitude of orientation maneuvers are modulated adaptively based on whether the perceived stimulus is attractive ($d > 0$) or aversive ($d < 0$). The direction of head casts alternates at every time step as proposed in Wystrach et al. (2016).

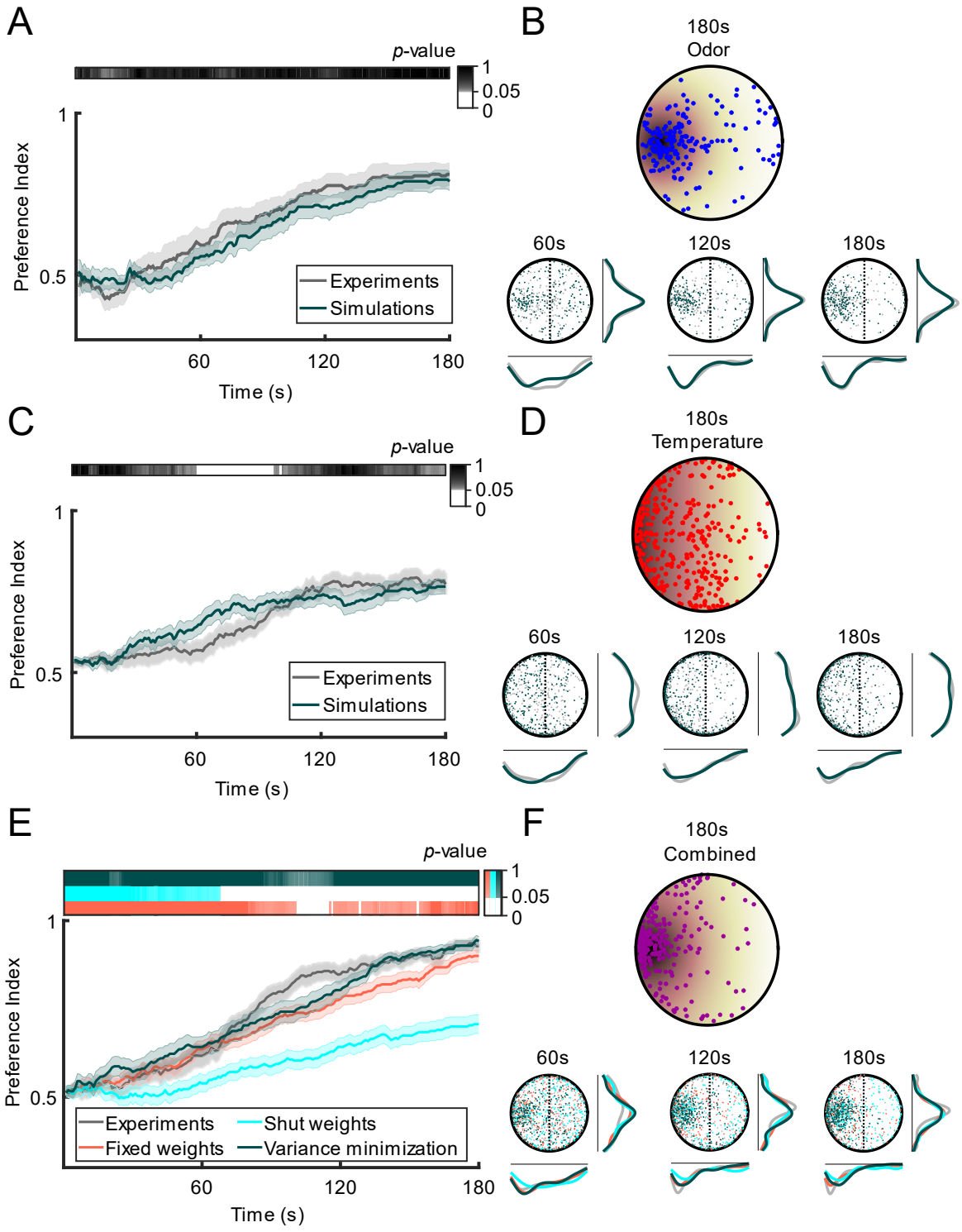

Figure 8: Framework for parameter optimization and testing of the agent-based model for larval navigation. (A) Sample simulations for the unimodal odor condition (Odor: Ethyl

butyrate, 10^{-3} M) after the free parameters associated with each condition were fit (n = 27). The preference index of simulated larvae was similar to the actual preference indices of wild-type larvae for the entire simulated odor condition (*t*-test, $p > 0.05$). The color bar above the plot indicates the significance of differences between the preference indices of the data and a given fit model. **(B)** The histograms at 60s, 120s and 180s illustrate the spatial distributions of simulated agent larvae and real larvae (gray) for the unimodal odor condition. (C) Sample simulations for the unimodal temperature condition (Temperature: 16-30^{o}C) after the free parameters associated with each condition were fit (n = 35). The preference index of simulated larvae was similar to the actual preference indices of wild-type larvae for over 80% of the duration of the simulated temperature condition (*t*-test, $p > 0.05$). The color bar above the plot indicates the significance of differences between the preference indices of the data and a given model. **(D)** The histograms of the spatial distributions of simulated agent larvae (colored) and real larvae (gray) for the unimodal temperature condition. **(E)** Predicted behavioral response of larvae to the combined odor and temperature conditions for each cue-combination rule compared to the actual preference index (n = 27). The preference indices of the simulated Variance-Minimization (VM) and Fixed-Weights (FW) strategies were indistinguishable with the data for over 90% of the entire time course (*t*-test, $p > 0.05$), while the Shut-Weights (SW) strategy remained significantly different from the data after the first minute of the simulation (*t*-test, $p > 0.05$). The color bars above the plot indicate the significant difference between the preference indices of the data and each model. **(F)** Histograms of the spatial distributions of simulated agent larvae (colored) and real larvae (gray) for the combined odor and temperature condition.

Application of the agent-based model to explore how sensorimotor integration is implemented in the *Drosophila* larva

The motor parameters of the agent-based model were first optimized to match the behavior of freely foraging larvae. Motor parameters were fit to model the movement patterns of wild-type (w^{1118}) larvae in the absence of any stimulus recorded at high spatio-temporal resolution with the closed-loop tracker from [23] and are assumed to be constants across all experimental conditions. The constants derived from the parameter optimization to model larval motion in the simulations are listed in Table 1 in the Materials and Methods.

The free parameters of the model associated with the multisensory stimuli from each condition (noise, sensitivity) were fit by minimizing the Kullback-Leibler (KL) divergence measured between the spatial distributions and preference indices of simulated and actual larvae. This was achieved by comparing the simulations to actual experimental probability distributions of larvae at different time intervals. We fit the free parameters using the datasets from unimodal conditions (Figure 8A-D). As part of this procedure, the variance associated with each signal was computed using the time course of the stimulus experienced by the agent larva (see Materials and Methods). We then tested each variant of the agent-based model using the three most-common cue-combination rules (Figure 7D) in the combined condition (Figure 8E-F). Based on a process of elimination, we observed that certain cue-combination rules matched the data in some gradient configurations but not others. For example, Figure 8E shows a condition where the experimental PI can be accounted for by the VM rule, but not the FW and SW rules. Additional details about how the models were constrained to capture the behavior of real larvae are provided in Materials and Methods together with Figure 1 and Figure 2.

We experimentally tested different combinations and configurations of multimodal gradients, including congruent gradients that point in the same direction and conflicting gradients that point in different directions. The KL divergence was used to quantify the degree of similarity between the spatiotemporal distribution of simulated larvae with that of real larvae. By testing paradigms with a variety of gradient geometries, we concluded that the Fixed-Weights model fails to predict behavior in conflicting gradients, such as a conflict between a virtual-odor and a real-odor gradient, (Figure 9A). The Shut-Weights (SW) model underperforms the Variance-Minimization (VM) model in congruent gradients as illustrated

with the congruent temperature and real-odor gradient shown in Figure 9B. By comparing the performances on all six experimental paradigms, the VM model gave the most consistent predictions of the three candidate solutions (Figure 9C, bottom panel), even though it did not produce the best fit for all conditions.

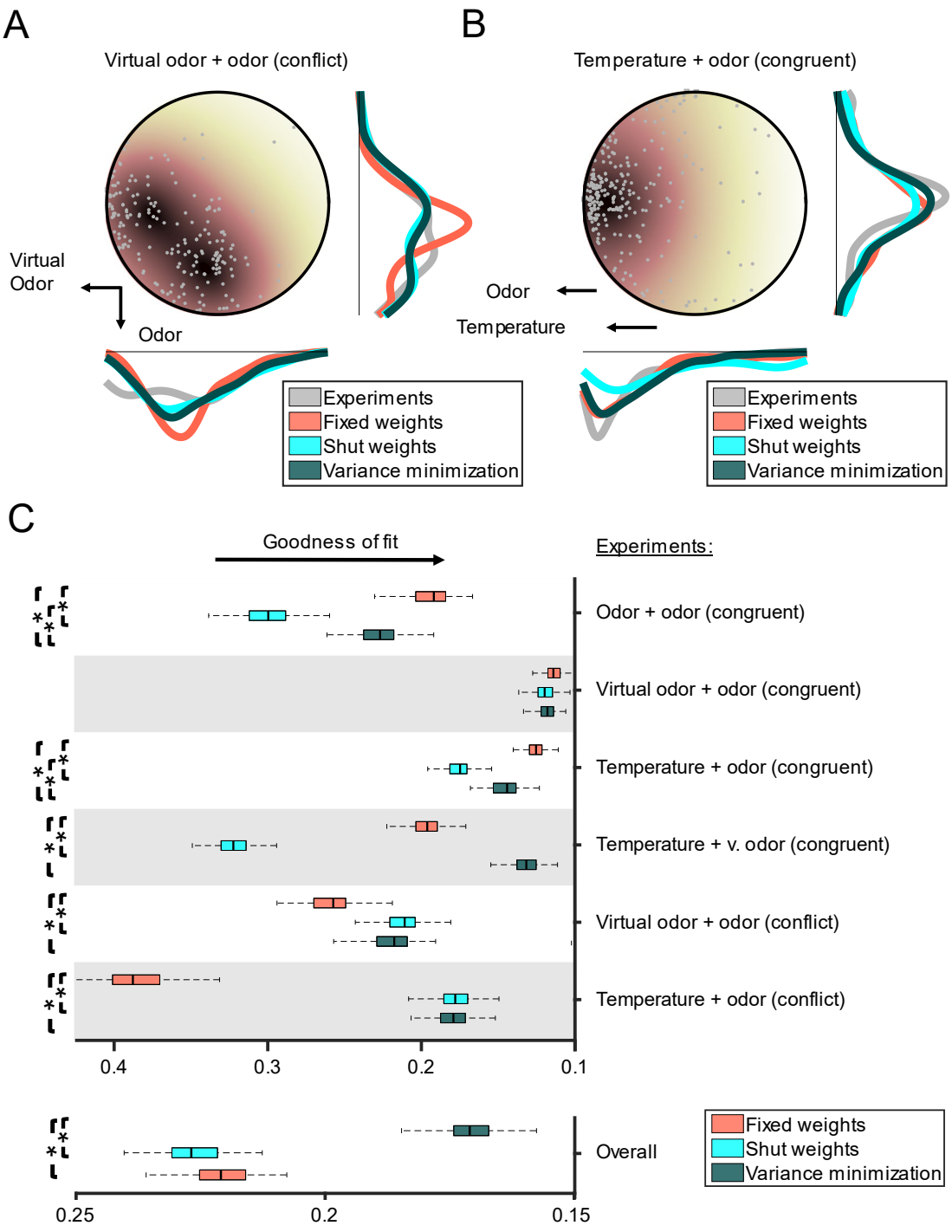

Figure 9: Comparison of the model performances for three cue-combination rules across different experimental paradigms. Final distributions of larvae for each simulated

cue-combination rule in a conflicting virtual-odor and real-odor gradient (Virtual Odor: Or67b>Chrimson, Light 625nm; Real Odor: Ethyl butyrate, 7.5 x 10-5M) in comparison to actual Or67b-functional larvae (n = 20). The FW strategy led to the poorest fit and was significantly different from both the SW and VM strategies (t-test, $p < 0.05$). **(B)** Final distributions of larvae for each cue combination rule in a congruent temperature and odor gradient (Temperature: 20-40oC; Odor: Ethyl butyrate, 10-3M) in comparison to actual Or42a single functional larvae (n = 30). The SW strategy gave the least accurate predictions and was significantly different from both the FW and VM strategies (t-test, $p < 0.05$). **(C)** Comparison of the goodness of fit, as measured by the KL divergence, for cue-combination rules across all experimental paradigms (1-6). The predictions of the VM strategy produced the closest goodness of fit on average to the data (overall), and the VM strategy was significantly different to the FW and SW strategies (t-test, $p < 0.05$). Asterisks indicate significant differences between each model to the best fitting model for each experimental paradigm.

Since the VM model combines information with cues that are weighted according to their relative level of reliability (eq. (7)), this scenario suggests that larvae are capable of measuring and processing the variance of their sensory inputs. To test this hypothesis, we experimentally modulated the variability associated with the olfactory cue by optogenetically corrupting sensory encoding in the olfactory sensory neuron (OSN) expressing the *Or42a* odorant receptor, which is tuned to the fruity odor ethyl butyrate [34], [39]. As described in the Materials and methods, the additive noise consisted in brief random flashes of light inducing the transient depolarization of the *Or42a* OSN expressing Chrimson, while the OSN was responding to the real-odor gradient. As expected, we observed that the chemotaxis of real larvae was weakened when olfactory noise was added to the odor gradient. More surprisingly, we found that thermotaxis improved as quantified by the PI when olfactory noise was added to the detection of a temperature gradient in the absence of any odor gradient (Figure 11A). This seemingly counterintuitive improvement in thermotactic performance illustrates that the weight of each cue is defined by its relative

level of reliability: as the noise level increases in the olfactory channel, the reliability of the encoding of genuine dynamic changes due to the odor gradient decreases. In eq. (7), we observe that an increase in σ_1 produces an increase in w_2 irrespective of the presence of any directional signal s_1. Therefore, the injection of pure noise into the olfactory system decreases the weight of this modality and enhances the salience of the thermosensory information.

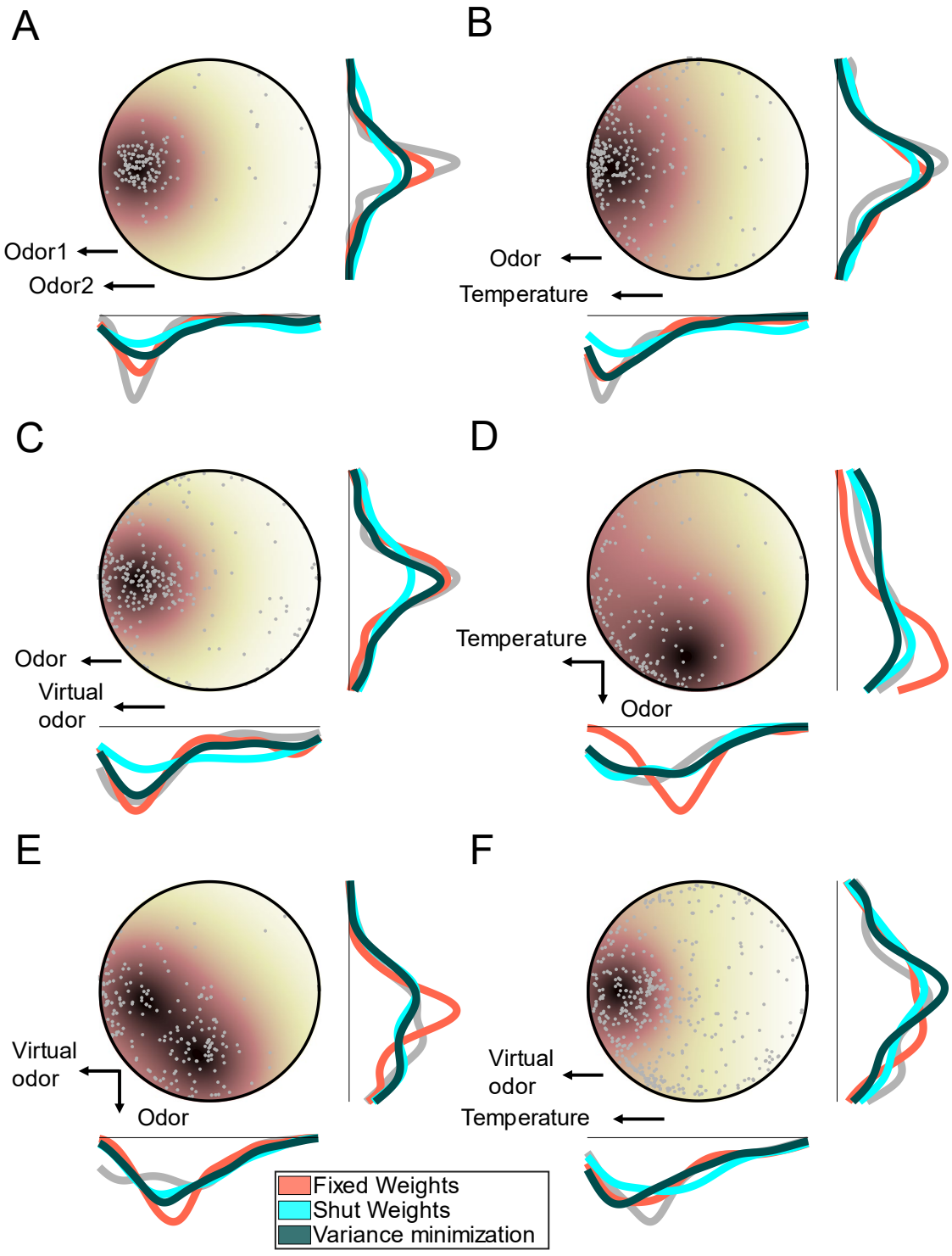

Figure 10: Comparison of final distributions of simulated larvae for each cue-combination rule across different experimental paradigms. (A) Odor + odor congruent

(odor 1: 1-hexanol, 10^{-2} M; odor 2: ethyl butyrate, 10^{-3} M; n = 19). **(B)** Temperature + odor congruent (odor: ethyl butyrate, 10^{-3} M; temperature: 16-30ºC; n = 27). **(C)** Virtual odor + odor congruent (virtual odor: *Or67b*>Chrimson, light 625nm; real odor: ethyl butyrate, 2.5 x 10^{-4} M; n = 30). **(D)** virtual odor + odor conflict (virtual odor: *Or67b*>Chrimson, light 625nm; real odor: ethyl butyrate, 7.5 x 10^{-5} M; n = 20) **(E)** Temperature + odor conflict (temperature: 20-36ºC; odor: ethyl butyrate, 2.5 x 10^{-4} M; n = 20). **(F)** Temperature + virtual odor congruent (virtual odor: *Or42a*>Chrimson; temperature: 20-40ºC; n = 49).

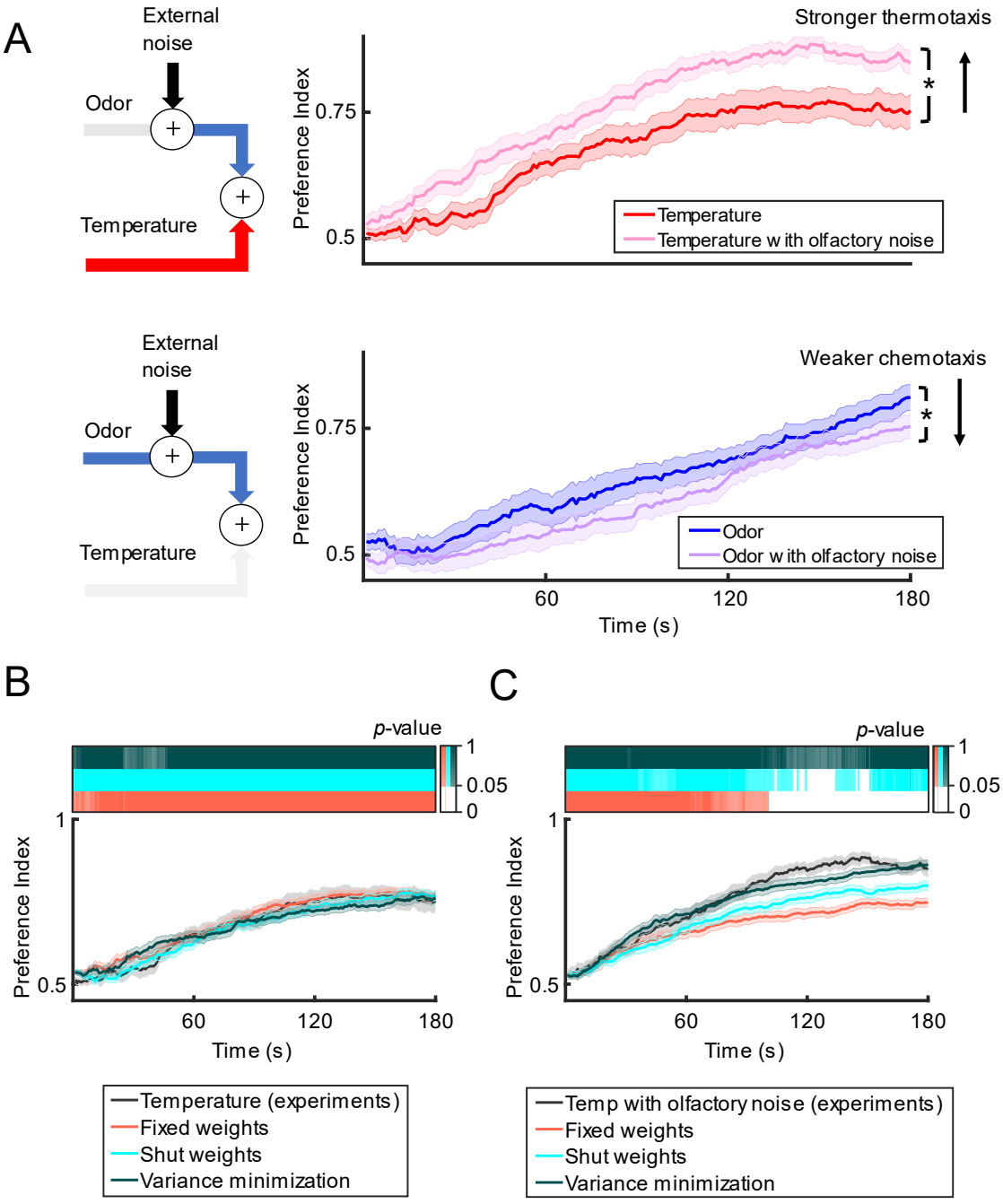
A
External noise
Odor
Temperature
Stronger thermotaxis
Preference Index
0.75
0.5
*
Temperature
Temperature with olfactory noise
External noise
Odor
Temperature
Weaker chemotaxis
Preference Index
0.75
0.5
*
Odor
Odor with olfactory noise
60
120
180
Time (s)
B
p-value
1
0.05
0
1
Preference Index
0.5
60
120
180
Time (s)
Temperature (experiments)
Fixed weights
Shut weights
Variance minimization
C
p-value
1
0.05
0
1
Preference Index
0.5
60
120
180
Time (s)
Temp with olfactory noise (experiments)
Fixed weights
Shut weights
Variance minimization

Figure 11: Drosophila larvae adapt their orientation responses to the variance of sensory inputs. (A) Or42a-functional larva navigated odor and temperature gradients while pure noise was injected into the olfactory system via the Or42a neuron in the form of optogenetic light flashes. The top graph compares the preference indices for larvae navigating a temperature gradient with and without olfactory noise (Temperature: 20-40oC; Olfactory noise injected through the Or42a OSN with light flashes at 625nm, 11.15W/m2). The bottom plot compares the preference indices for larvae in an odor gradient versus the same odor gradient with olfactory noise (Odor: Ethyl butyrate, 10-3M; Olfactory Noise: Or42a, Light 625nm, 11.15W/m2). The preference indices for conditions with and without noise are significantly different from one another at the end of the experiment as indicated by the asterisks (t-test, $p < 0.05$). **(B)** Actual and simulated response for larvae in a temperature gradient based on the preference index. The FW, SW, and VM strategies are all in agreement with the data for the entire duration of the simulation (t-test, $p > 0.05$). **(C)** Actual and simulated response for larvae in a temperature gradient with olfactory noise based on the preference index. The VM strategy is indistinguishable from the data for the entire duration of the simulation (t-test, $p > 0.05$), but the FW and SW strategies are significantly different in the latter half of the simulation (t-test, $p < 0.05$). The statistical significances of differences between the data and each model are indicated by the color bars above the plots.

To simulate the effects of the olfactory noise on the thermotaxis of agent-based larvae, random disturbances in the activity of the *Or42a* OSN were modeled by the addition of an internal Gaussian noise term to the olfactory signal (see Materials and Methods). In this framework, numerical simulations established that only the VM model was able to qualitatively capture an improvement in thermotactic performances upon injection of pure noise to the olfactory channel (Figure 11B-C). This result strongly supports our hypothesis that the *Drosophila* larva uses an uncertainty-weighted mechanism to integrate multimodal stimuli.

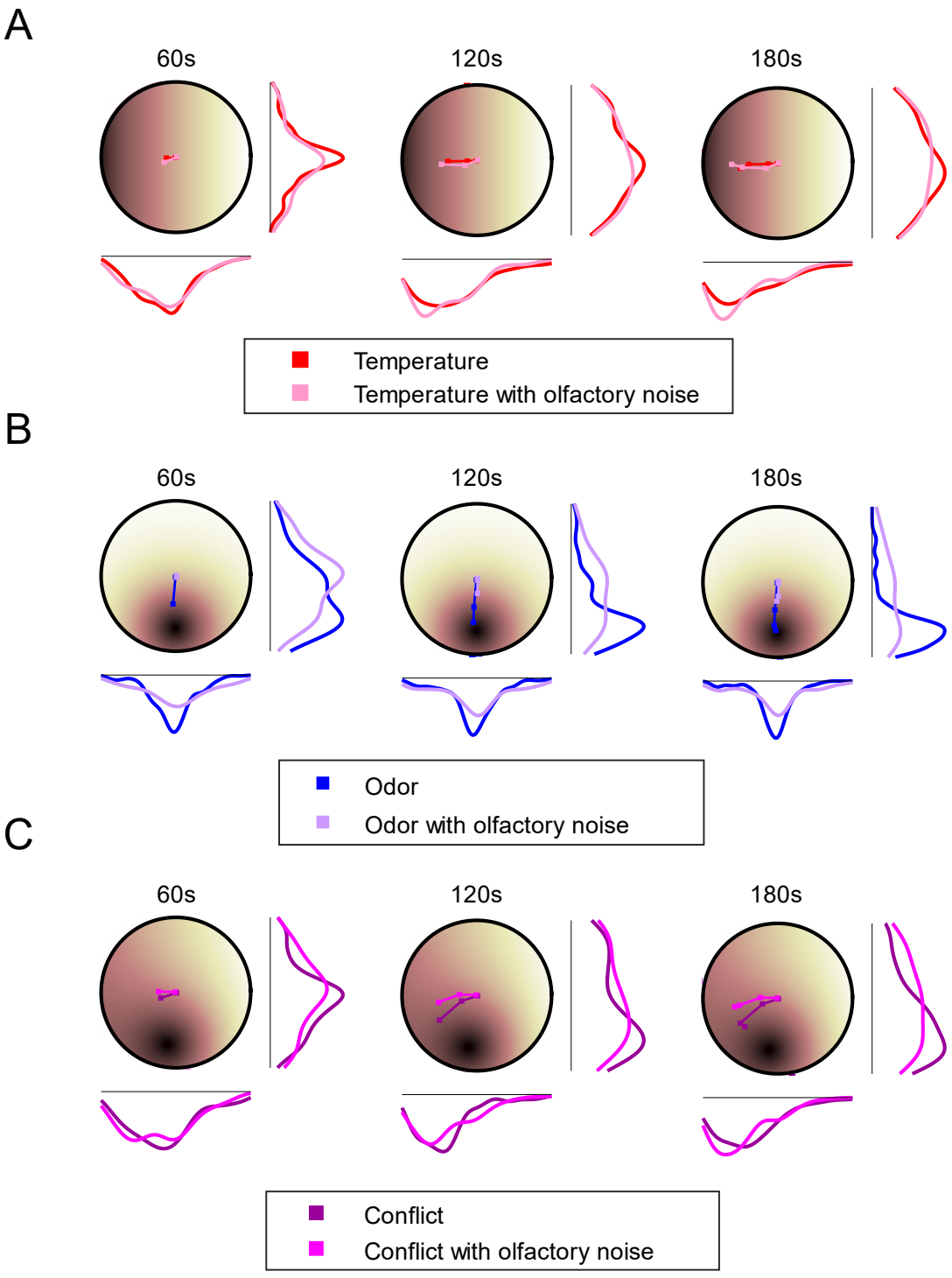

Figure 12: The effect of olfactory noise on navigation in a temperature gradient, an odor gradient, and a conflicting temperature and odor gradient. Each figure shows a

comparison of the distributions of real larvae in gradient configurations with and without olfactory noise applied optogenetically (optogenetic olfactory noise: *Or42a*>Chrimson). The mean trajectory of all larvae is shown in the arena over each time interval (60s, 120s, 180s). **(A)** Temperature: 20-36ºC, n = 20. **(B)** Odor: ethyl butyrate, 2.5 x 10^{-4} M; n = 20. **(C)** Temperature + odor conflict (Temperature: 20-36ºC; odor: ethyl butyrate, 2.5 x 10^{-4} M; n = 20)

Two alternative strategies to navigate multimodal gradients optimally

Next, we asked whether the larval nervous system might have evolved to optimize other objectives besides the reliability of each sensory signal to navigate multimodal gradients, and how other strategies might compare to the VM rule (Figure 13). More specifically, we examined whether the exact cue-combination strategy used by larvae is dependent on the nature of the sensory modalities that are combined. Figure 13B illustrates how the VM rule combines a noisy olfactory cue (blue, broader distribution) with mean s_2 and a less noisy temperature cue (red, narrower distribution) with mean s_1 into the decision variable d. As a result of eq. (7), the temperature cue has a higher weight than the olfactory cue since $\sigma_1 < \sigma_2$.

An alternative objective that a larva could plausibly maximize during navigation is reward. More concretely, we define reward as the probability that motion is directed toward a direction favorable to the encounter of food (motion oriented up an odor gradient) or away from the punishment of potentially noxious heat (motion down a temperature gradient). This strategy, which we call Reward Maximization (RM), is illustrated in Figure 13A with the same two cues configuration presented in Figure 13B. For each of the two cues, the probability that the gradient is positive is equal to the cumulative probability that the cue is greater than zero. Given that the experiments are set up by design for each gradient to be

similar in attraction, we make the modeling assumption that there is an equal preference for reaching either favorable sensory condition — whether it is food at the peak of an odor gradient or a temperature range suitable to development. Thus, the reward associated with the maintenance of an ongoing heading is the sum of the probabilities of following a favorable gradient for each of the two modalities. As shown in the Materials and Methods, the sum of these cumulative probabilities can be approximated as the following decision variable:

$$d = \frac{\sigma_1+\sigma_2}{\sigma_1\sigma_2} \times \left(\frac{\sigma_2}{\sigma_1+\sigma_2}\, s_1 + \frac{\sigma_1}{\sigma_1+\sigma_2} s_2\right). \quad (50)$$

To facilitate a comparison with the reward maximization strategy, the VM rule can be rewritten as:

$$d = \frac{\sigma_1^2+\sigma_2^2}{\sigma_1^2\sigma_2^2} \times \left(\frac{\sigma_2^2}{\sigma_1^2+\sigma_2^2}\, s_1 + \frac{\sigma_1^2}{\sigma_1^2+\sigma_2^2} s_2\right). \quad (51)$$

More generally, we note that the VM and RM rules can be written in the form:

$$d = \frac{\sigma_1^p+\sigma_2^p}{\sigma_1^p\sigma_2^p} \times \left(\frac{\sigma_2^p}{\sigma_1^p+\sigma_2^p}\, s_1 + \frac{\sigma_1^p}{\sigma_1^p+\sigma_2^p}\, s_2\right), \quad (52)$$

where the value of p determines the exact decision rule used. We will hence also refer to the RM strategy as the $p = 1$ rule and the VM strategy as the $p = 2$. Furthermore, the FW strategy can be obtained by setting $p = 0$, while the SW strategy is obtained in the limit as p approaches infinity. The decision variable of eq. (52) is generic: it captures a variety of cue-combination strategies defined by the value of a parameter p called a *bimodal-contrast parameter*.

The decision rule applied by a larva is modality-dependent

For a congruent gradient with real odors, the simulated behavior of agent larvae directed by the RM rule reproduced the behavior of real larvae more accurately than agent larvae implementing the VM rule (Figure 13D). This is consistent with the initial results where we showed that the multiplicative combination rule captured the combined PI and that its decision rule corresponds to the case $p = 1$. On the other hand, the VM rule was more accurate than the RM rule to reproduce larval behavior for a conflicting gradient of odor and temperature (Figure 13E). To generalize this analysis, we set out to compare the goodness of fit of both of the RM and VM rules across all experimental paradigms considered in Figure 9. In addition, we systematically computed the performances associated with specific cases of the decision rule captured by eq. (10), with $p = 1$ representing the RM rule, $p = 2$ representing the VM rule, and the FW and SW rules defining the lower and upper bounds as the value of p approaches zero and infinity, respectively. By following this approach, we aimed to determine whether the same rule produced the best fit with the behavior of real larvae for all experimental conditions.

By evaluating the goodness of fit of the simulations to the data for decision rules with different values of p (Figure 13C), we made the striking observation that the decision rule applied by real larvae may be dependent on the sensory modalities being combined. While experimental paradigms combining odor and temperature gradients were on average best predicted by decision rules with a value of the bimodal-contrast parameter p close to 2, experimental paradigms combining two odor gradients had a goodness of fit curve that suggested the use of a decision rules with a bimodal-contrast parameter close to 1.

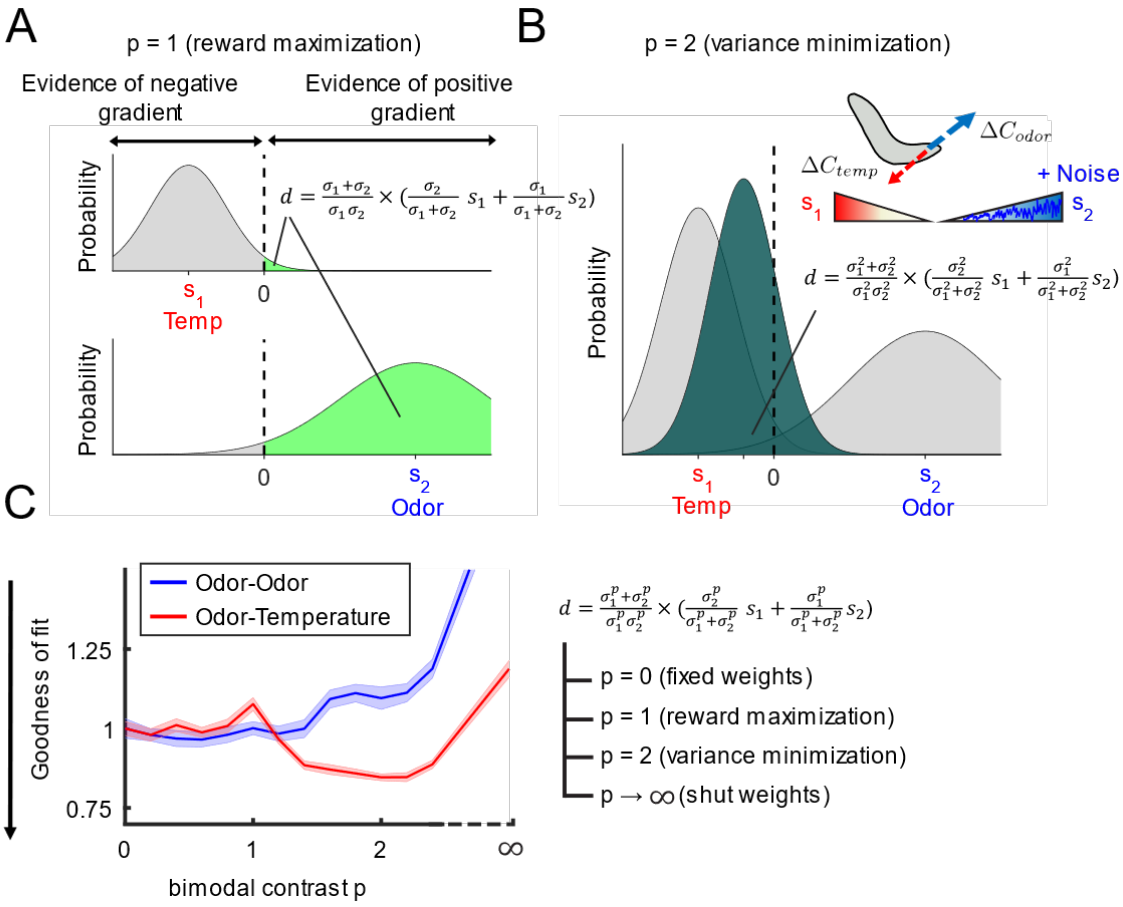
A
p = 1 (reward maximization)
Evidence of negative gradient
Evidence of positive gradient
Probability
$d = \frac{\sigma_1+\sigma_2}{\sigma_1\sigma_2} \times (\frac{\sigma_2}{\sigma_1+\sigma_2} s_1 + \frac{\sigma_1}{\sigma_1+\sigma_2} s_2)$
s1
Temp
0
Probability
0
s2
Odor
B
p = 2 (variance minimization)
ΔC_{odor}
ΔC_{temp}
+ Noise
s1
s2
Probability
$d = \frac{\sigma_1^2+\sigma_2^2}{\sigma_1^2\sigma_2^2} \times (\frac{\sigma_2^2}{\sigma_1^2+\sigma_2^2} s_1 + \frac{\sigma_1^2}{\sigma_1^2+\sigma_2^2} s_2)$
s1
Temp
0
s2
Odor
C
Odor-Odor
Odor-Temperature
Goodness of fit
1.25
1
0.75
0
1
2
∞
bimodal contrast p
$d = \frac{\sigma_1^p+\sigma_2^p}{\sigma_1^p\sigma_2^p} \times (\frac{\sigma_2^p}{\sigma_1^p+\sigma_2^p} s_1 + \frac{\sigma_1^p}{\sigma_1^p+\sigma_2^p} s_2)$
p = 0 (fixed weights)
p = 1 (reward maximization)
p = 2 (variance minimization)
p → ∞ (shut weights)
D
Odor1
Odor2
Experiments
p = 1
p = 2
E
Temperature
Odor
Experiments
p = 1
p = 2

Figure 13: Exploring two different notions of optimality for navigation in sensory gradients. (A) Visualization of the reward maximization (RM) rule (p = 1) combining two noisy signals. **(B)** Example of the variance minimization (VM) rule (p = 2) combining a noisy odor signal (blue) and a less noisy temperature signal (red). **(C)** The goodness of fit across experimental paradigms to decision rules with different non-integer values of p. **(D)** Final distributions of larvae in a congruent odor and odor gradient (Odor 1: 1-hexanol, 10-2M; Odor 2: Ethyl butyrate, 10-3M) for the simulated RM and VM rules in comparison to actual wild-type larvae (n = 19). **(E)** Final distributions of larvae in a conflicting temperature and odor gradient (Temperature: 20-36oC; Odor: Ethyl butyrate, 2.5 x 10-4M) for the simulated RM and VM rules in comparison to actual Or42a-functional larvae (n = 20).

To understand why *Drosophila* larvae may use different cue combination strategies depending on the environmental context, we turned to numerical simulations. We quantified how well agent larvae navigated toward favorable gradients using each strategy. To compare how the $p = 1$ rule (equivalent to RM) performed with respect to the $p = 2$ rule (equivalent to VM), we defined two additional metrics quantifying larval behavior to explore and reveal the nuances between the two strategies (Figure 14A-B). The first is "*Reward*", which would presumably be maximized under the $p = 1$ rule; the second is "*Fraction at Source*", which is a generalization of the PI beyond congruent gradients. The "*Fraction at Source*" metric, like the PI, quantifies the proportion of larvae that are within specified regions defining favorable conditions (peak of the odor gradient or region with a comfortable temperature, see Materials and Methods). The "*Fraction at Source*" metric is binary: either an animal is inside or outside a favorable region. The "*Reward*" metric defines in a graded way how well larvae remain near or at a favorable location on average. For conflicting gradients, the *Reward* metric can take relatively large values when a larva is located in a region representing a trade-off between the odor and the temperature gradients, whereas the *Fraction at Source* metric leads to 0 values unless the larva has focused on one of the two

gradients. Thus, these two metrics tell us how effective each cue combination strategy is at achieving a trade-off between two gradients.

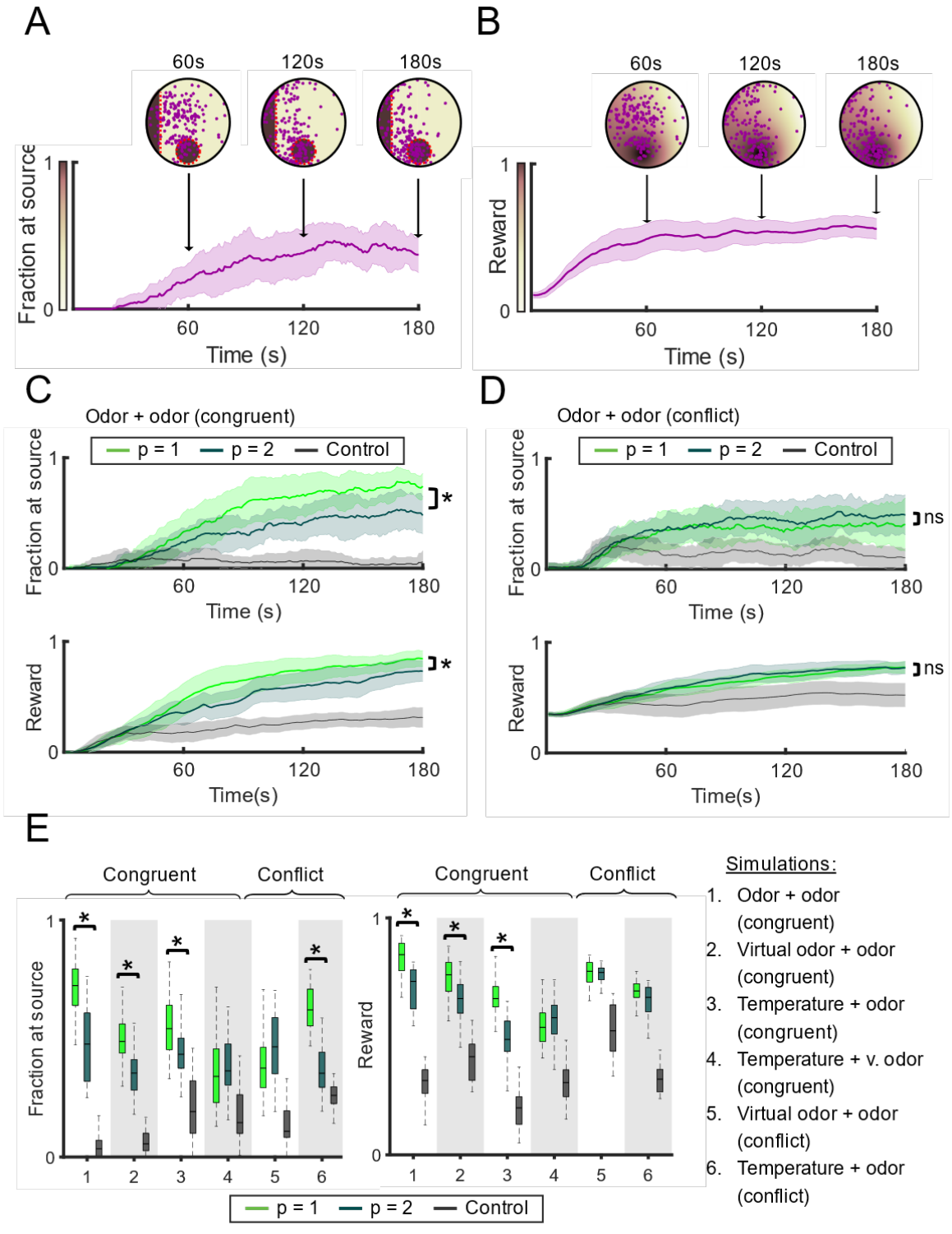

Figure 14: Comparison of the overall performances and characteristics of the RM rule ($p = 1$) and the VM rule ($p = 2$) directing the behavior of simulated agent-based

larvae. Metric quantifying the "Fraction at Source" metric to quantify how well larvae remain near the source for conflicting temperature + odor gradients. Red dotted lines indicate the boundaries of the two sources. The color gradient indicates the performance of larvae at each location in the arena. **(B)** Metric quantifying the "Reward" for the same data as panel A. In both panel A and B, a higher score implies a better performance. **(C)** Comparison of the Fraction at Source and Reward for a pair of congruent odor + odor gradients. The control condition refers to the performance of simulated agent-based larvae in the absence of any sensory (C-E) information (i.e., decision variable $\boldsymbol{d} = \mathbf{0}$). Simulations of the RM and VM rules lead to a significant difference in both the final Fraction at Source and Reward (t-test, $p < 0.05$). **(D)** Comparison of the Fraction at Source and Reward metrics for a pair of conflicting odor + odor gradients. Both rules result in a significant difference in the final Fraction at Source (t-test, $p < 0.05$) but not the reward (t-test, $p > 0.05$). **(E)** Comparison of the Fraction at Source and Reward across all experimental paradigms. The RM rules and VM rules were significantly different for all conditions by both metrics (t-test, $p < 0.05/6$ upon Bonferroni correction) except for conditions with conflicting gradients. The asterisks indicate significant differences between the RM rule ($p = 1$) and the VM rule ($p = 2$) for each condition.

When we applied the two metrics to quantify the behavior of simulated agent larvae directed by the $p = 1$ (RM) and $p = 2$ (VM) rules, we observed that the differences between the two rules were more significant in congruent gradients than in conflicting gradients (Figure 14C-D). The reward gained by using $p = 1$ instead of $p = 2$ was more significant for congruent gradients compared to conflicting gradients (Figure 14E). We also numerically validated this effect through simulations of a fictive scenario where the conflict angle was sequentially modulated from 0 to 90 degrees (Figure 15). This hints that the advantages of $p = 1$ over $p = 2$ are situational. When comparing these metrics across experimental paradigms, we observed that in general, the $p = 1$ rule performs equally well or better than $p = 2$ when it comes to maximizing the net reward that arises from the combination of two modalities. Effectively, the RM rule achieves a tradeoff between the hedonic value associated with each sensory gradient.

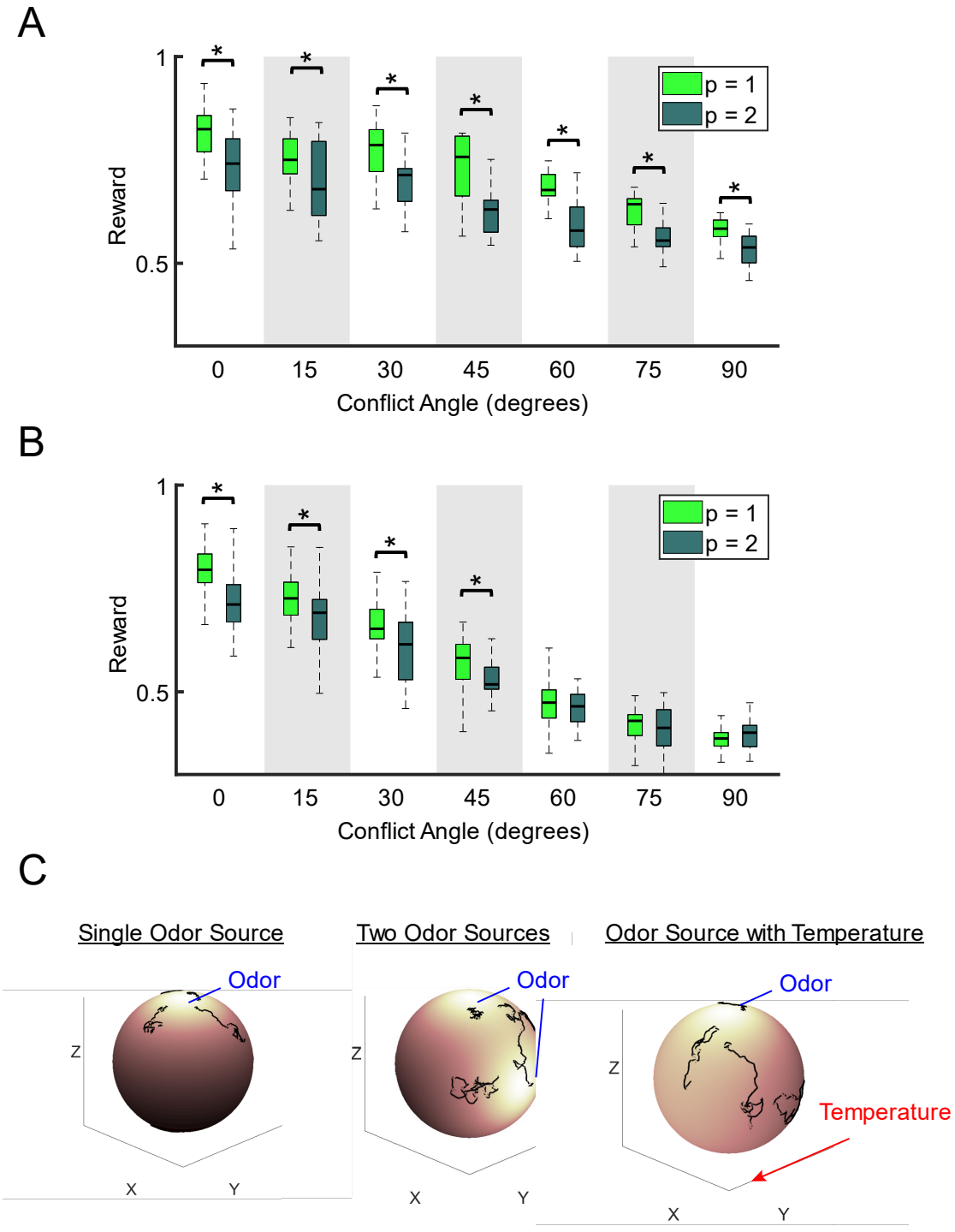

Figure 15: Agent-based model as a testing environment for simulating hypothetical gradient configurations with different conflicting angles. (A) Virtual odor + odor conflict

(n = 19). The mean reward at the end of the simulation is compared between the reward maximization ($\boldsymbol{p = 1}$) and variance minimization ($\boldsymbol{p = 2}$) rules. The asterisk indicates a significant difference by a t-test ($p < 0.05$) **(B)** Temperature + odor conflict (n = 19). **(C)** Simulations of larvae navigation on the surface of a sphere for different stimulus landscapes (randomly sampled larvae trajectories indicated in black): a single odor source (left), two odor sources (middle), and a single odor source with a linear temperature gradient along the y-axis (right). Color gradient indicates attractiveness of each region (bright = high reward, dark = low reward).

Discussion

In the present work, we developed an experimental paradigm to quantify the behavior of larvae experiencing congruent or conflicting spatial gradients of odor and temperature. Using this paradigm, we demonstrated that larvae are capable of adjusting the sensitivity of individual sensory channels to changes in the variance of signals transmitted by each modality. In a similar vein as the model delineated in [17] for larvae stimulated by nondirectional white noise with different statistical properties, we establish that the mechanism for variance adaptation can also be described as a weighted sum of sensory cues with weights modulated by signal variance.

While previous work in the larva analyzed multisensory combination mechanisms by observing one specific behavior — the "*when to turn*" mechanism that controls the timing of sensory-driven transitions from running (crawling) to turning [16], [17], we extended this analysis to directional cues and showed that variance adaptation generalizes to the navigation algorithm as a whole including the mechanism of "*where to turn to*" that creates a turning bias towards favorable sensory gradients. Through numerical simulations, we used a data-driven agent-based model to establish that both of these orientation mechanisms are necessary to account for the navigation of real larvae in multimodal stimuli as removing either component leads to a reduction in performance (Figure 2E). Similar to the adult fly [40], the ability to bias turning toward the gradient ("*where to turn to*") was found to be critical for larvae to navigate toward and accumulate near the odor source.

We tested different plausible strategies for combining sensory inputs, starting with a comparison between the Variance-Minimization (VM), the Fixed-Weights (FW) and the

Shut-Weights (SW) rules. The FW and SW rules can be viewed as opposite extremes in the framework of Bayesian cue integration [7]: while the FW rule always integrates both sensory stimuli, the SW rule systematically discards the less reliable sensory stimulus. This explains why the SW rule is sometimes called Winner-Take-All rule. Similar comparative approaches have been used in the past to compare and evaluate how well different cue combination models fit behavior, for example in human behavior in a two-alternative-forced-choice task [41]. In our results across experimental paradigms, the VM rule accounted best for the behavioral data, while we found that the FW and SW rules were insufficient on their own to adequately reproduce the navigational behavior of larvae for all tested conditions. Next, we introduced the Reward-Maximization (RM) rule, which differs from the VM rule in that it does not assume that the two gradients originate from the same object and location, and seeks to maximize the expected reward of the two gradients (see Figure 13A-B and Materials and Methods). Given the assumptions of the model, both the VM and RW rules are optimal with respect to the objectives they seek to maximize: in the case of the RM rule, it is the reward —strength of the odor stimulus and comfort level of the temperature— that is optimized whereas in the case of the VM rule, it is the reliability of the combined signal.

Since the cue-combination strategies compared in the present study could simply represent four mechanisms out of a limitless set of possible models, we developed a framework to map all four models into a canonical model described in eq. (10) defined by the value of a *bimodal-contrast parameter* p. With this generalized set of models, we showed that our results remained the same in that the RM ($p = 1$) and VM ($p = 2$) were most representative of the way cue combination is implemented by real larvae. Furthermore,

we found that some experimental paradigms were better accounted for by the RM rule while others appeared to be more compatible with the VM rule, depending on the pairs of sensory modalities combined by the animal. In particular, the behavior of larvae in a real-odor gradient combined with a congruent temperature gradient was better explained by a principle of variance minimization (VM rule). We believe that this gradation in the decision rule across sensory modalities might reflect the existence of different noise-suppression mechanisms on the underlying behaviors.

Intuitively, larvae may have developed mechanisms of sensory cue combination resembling the RM and the VM rules to exploit different aspects of the sensory conditions that favor their survival in complex natural environments. This hypothesis was tested numerically by evaluating the performance of simulated agent larvae directed by either of the RM ($p = 1$) and VM ($p = 2$) rules in each experimental paradigm (Figure 14C-E), as well as in hypothetical scenarios not tested with real larvae (Figure 15) that include more realistic three dimensional environments. Not surprisingly, we found that larvae experienced a larger "reward" on average with the RM ($p = 1$) rule compared to the VM ($p = 2$) rule. However, the comparison between the RM and VM rules led to more ambiguous results when performances were evaluated based on the fraction of larvae reaching the "source", as differences in performances between the two rules vanished in conflicting gradients compared to congruent gradients. This result is consistent with the fact that increasing the spatial proximity between cues leads to a smaller improvement in signal reliability during cue combination [42].

In the extreme scenario where gradients are pointing at a 90-degree angle, both the RM and VM rules perform similarly as the combination of sensory information becomes

less advantageous (Figure 14D and Figure 15A-B). In addition, the two rules differ in that the RM ($p = 1$) rule is closer to the FW ($p = 0$) rule, which always integrates information from both sensory inputs. By contrast, the VM rule leads to a choice of one source over the other resembling the SW ($p = \infty$) rule. When presented with two sources of sensory information, virtual larvae using the RM rule were more prone to remain in between two attractive sources while larvae using the VM rule tended to choose one source over the other. Our agent-based model provides a computational platform to investigate larval integration strategies in more realistic settings, such as navigation on the surface of a sphere (i.e. a rotting piece of fruit). For example, we find that our results extend to a conflict between two attractive odor sources on a spherical surface (Figure 15C).

To explain why larvae appear to utilize the more-integrative RM ($p = 1$) rule in odor-odor gradients but use the choice-like VM ($p = 2$) rule in odor-temperature gradients, we speculate that this nuance may be an example of bet hedging, when organisms suffer decreased fitness in comfortable conditions in exchange for increased fitness in stressful conditions [43]. A larva that cannot feed in a region of moderate temperature is less likely to survive than a larva that chooses to either follow an odor gradient predictive of the presence of food even at the cost potential of noxious heat or to navigate toward a cooler region where food might be found eventually. In the case of odor-odor gradients, larvae might have an advantage to combine multiple chemical cues in a more integrative way given that food sources typically release dozens or hundreds of distinct odorant molecules that are detected by the peripheral olfactory system. By contrast, in situations that present possible danger like aversively high temperatures or starvation in the absence of food, it may be more

prudent for larvae to select the more reliable sensory modality earlier as predicted by the VM rule.

Here, we report experimental and modeling-based evidence that *Drosophila* larvae are capable of computing and combining the reliability of sensory inputs to organize orientation behavior in natural conditions. This result suggests that the nervous system of organisms as simple as the *Drosophila* larva can achieve probabilistic inference —a form of computation highly advantageous in uncertain environments. Moreover, the ability of the larva to adapt its navigation strategy to the nature of the perceived multisensory signals offers an opportunity to study differences in the neural implementation of two general rules achieving cue combination based on probabilistic inference, reward maximation and variance minimization. With the availability of the larval brain connectome [1], the *Drosophila* larva sets a path to pinpoint where and how different sensory cues are combined and to investigate how these rules evolve across different development stages, such as for the cue integration of odor and wind in the adult fly [12], [44].

Depolarization block in olfactory sensory neurons expands the dimensionality of odor encoding

Introduction

Animals identify odors based on the combinatorial activation of olfactory sensory neurons, each with distinct chemical receptive fields. Historically, it is commonly believed that the dose response of any olfactory sensory neuron follows a sigmoidal function that grows monotonically until it reaches a plateau. However, this would imply that the subset of olfactory sensory neurons activated by an odor would scale up with the odor concentration, undercutting the efficiency of combinatorial coding at high odor concentrations. Here, we show that olfactory sensory neurons can in fact undergo a silent state upon strong and prolonged excitation called depolarization block, as part of their normal physiological function at ethologically-relevant odor concentrations. This silencing typically occurs at odor concentrations three orders of magnitude above the detection threshold of the olfactory sensory neuron. Using a data-driven model of the olfactory transduction cascade paired with a conductance-based spike generation model, we present a plausible biophysical mechanism that explains the emergence of depolarization block as a dynamical bifurcation. Quantitative predictions related to the history dependence and timescale of depolarization block are validated experimentally, allowing us to predict and simulate the activity of olfactory sensory neurons during larval navigation in odor gradients. We find that the same odor can induce depolarization block in distinct types of olfactory sensory neurons according to a concentration sequence matching their relative sensitivities to the odor, which fractionates

the odor concentration space into domains corresponding to different subsets of active olfactory sensory neurons. As a consequence of the silencing of olfactory sensory neurons that undergo strong olfactory transduction currents, high-odor concentrations do not necessarily recruit increasingly large numbers of olfactory sensory neurons. We argue that depolarization block might facilitate perceptual recognition and discrimination over a large odor concentration range by maintaining sparsity in neural representations. While the role of depolarization block has been largely overlooked in chemosensory systems, our results suggest that this phenomenon creates a new dimension that expands the coding capacity of the peripheral encoding of odors. Altogether, our results indicate that depolarization block fulfills an important physiological function as a feature in sensory neurons rather than as a bug in its involvement in disease states such as epilepsy [45], [46] and migraines [47].

Materials and Methods

Automated FFT spike sorting:

Manual spike sorting was complemented by an automated method to identify the onset of depolarization block in electrophysiology recordings. As illustrated in Figure 16, the method relied on a power spectral analysis implemented with a fast Fourier transform (FFT) algorithm. Trains of tonic spikes originating from the olfactory sensory neuron could be associated with the frequency with the highest power spectral density. In the automated FFT spike sorting, we applied a sliding time window of 1 second on each recording over which the power spectrum was computed. For each time sample, the firing rate was labelled as the

peak non-zero frequency of the signal. To identify the time intervals lacking tonic spiking, a minimum cut-off value in the peak power spectral density was applied to classify whether sustained neural activity was present. For each recording, this cut-off value was defined as the 95th percentile of power spectral values, such that peak spectral densities above this threshold were classified as spiking activity and peak spectral densities below this threshold are filtered out as background noise. To validate the accuracy of the automated FFT spike sorting algorithm to identify the termination of tonic spiking at the onset of depolarization block, we used a set of recordings that had been manually annotated as ground truth (Figure 16B).

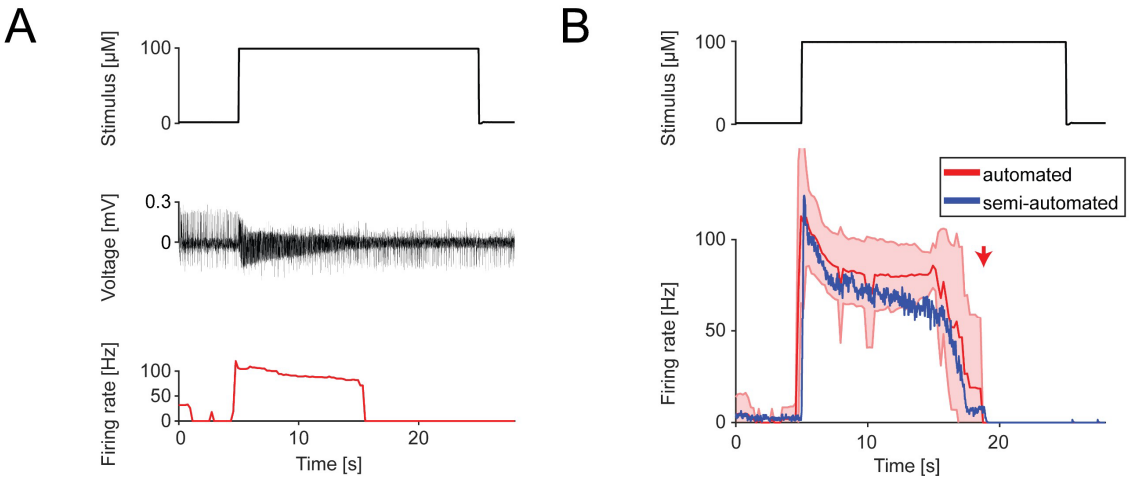

Figure 16: Fully automated spike sorting algorithm. (A) Firing rate estimated by using the automated FFT spike sorting method for a single (n=1) recording (for implementation details, see Methods section). **(B)** Comparison of the semi-automated spike sorting with the automated FFT spike sorting method for all (n=10) recordings. The experimental data used in this figure come from Figure 24C. The shaded error bar indicates the minimum and maximum firing rate observed across all recordings.

Olfactory Sensory Neuron (OSN) Model:

The olfactory sensory neuron (OSN) model was inspired by the work of refs. [48], [49]. Like in the cascade model of ref. [48], the initial conversion of the odor detection into firing activity is viewed as a cascade of an odorant transduction process and a biophysical spike generator. However, while the biophysical spike generator is modelled as a Connor-Stevens point neuron in ref. [48], we instead adopt an alternative model [49] to include the characteristics of depolarization block in regimes of high intensity stimulation. Custom written MATLAB code is available at https://doi.org/10.25349/D92K69.

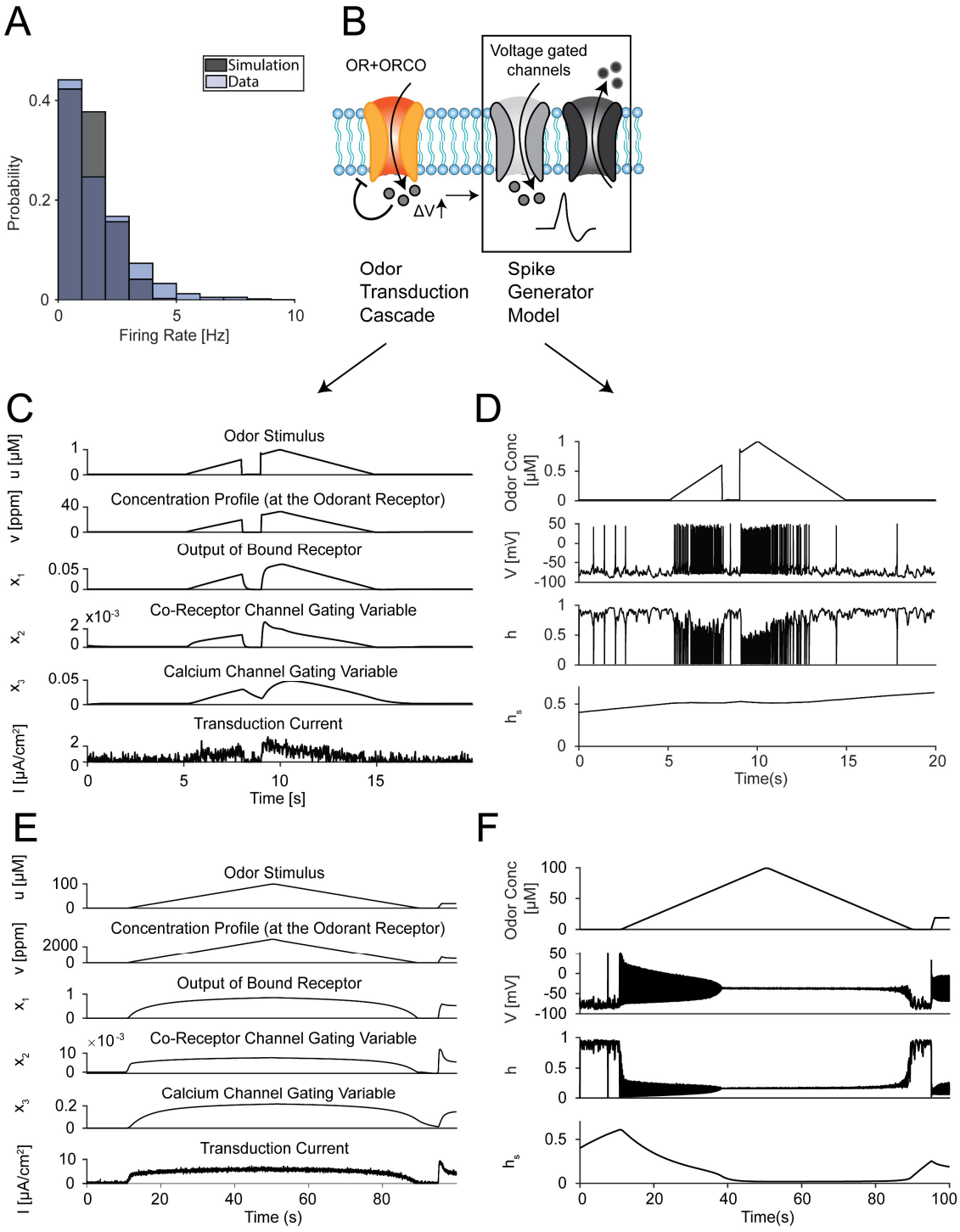

Figure 17: Detailed dynamics of the *Or42b* OSN model. (A) Distribution of recorded (light gray) and simulated (dark gray) spontaneous firing rates in the absence of odor. **(B)** The *Or42b* OSN model consists of the odor transduction model (left) and the spike generator model (right). For more details about each model, see main Figure 23 and the Methods section of the main text. **(C)** Transformation from odor stimulus to transduction

current through the odor transduction cascade for a linear ramp interrupted by a short stimulation gap. **(D)** Simulated *Or42b* OSN response to the stimulus shown in panel (C). **(E)** Transformation from odor stimulus to transduction current through the odor transduction cascade for a long linear ramp at odor concentrations eliciting depolarization block (see main Figure 23H). **(F)** Simulated *Or42b* OSN response to stimulus shown in panel (E). In panels (C) and (E), are the odor concentration (in μM), the corresponding concentration profile at the odorant receptor (in ppm), and the transduction current. The rest of the variables are defined at the top of each subpanel as well as in the Methods section. Note the conversion of units in the first step of the odor transduction cascade from μM to ppm (see also Table S3). In panels (D) and (F), V stands for the membrane potential, h the fast inactivation variable and h_s the slow inactivation of the sodium current (see Methods section).

Odor Transduction Model

We adapted the biophysical cascade model [48] of odor transduction from the adult fly to the larva. Besides the re-optimization of several parameters for the specific odorant-receptor pair in our assay (ethyl butyrate, OR42b), no modifications to the equations were required to reproduce the firing responses in the larval *Or42b* OSN. The model proposes the division of the olfactory transduction process into several mechanisms: (1) the peri-receptor process, (2) odorant receptor binding, and (3) co-receptor channel gating. Collectively, this signal cascade converts an odor concentration into a transduction current mediated by the opening of the co-receptor Orco [50].

The peri-receptor process, which models the diffusion and absorption of odorant molecules by the odorant receptor is described as follows as an odorant concentration profile at the odorant receptor v:

$$v = \int h(t-s)\, u(s)\, ds + \gamma \int h(t-s)\, du(s), \tag{53}$$

where u is the temporal waveform of the odor concentration experienced by the larva (Figure 17C and Figure 17E), $h(t)$ is a low-pass linear filter, and γ is a weighting factor that determines the dependency of the filtered waveform v on the odor concentration u and the odor gradient du/dt. The output odorant concentration profile v then interacts with the "private" odorant receptors (OR42b). This mechanism underlying this interaction is named as the bound-receptor generator, which models the fraction of odorant receptors x_1 that are bound at any given time:

$$\frac{dx_1}{dt} = b_r\, v\, (1 - x_1) - d_r\, x_1, \tag{54}$$

with the assumption that each private receptor only exists in one of two states: bound, or unbound. The equilibrium fraction of bound odorant receptors is driven by the odorant concentration profile v, with the parameters b_r defining the binding rate, and d_r representing the dissociation rate. The fraction of bound odorant receptors x_1 then modulates the opening of the co-receptor channel and calcium channel, modelled by gating variables x_2 and x_3, respectively:

$$\frac{dx_2}{dt} = \alpha_2\, x_1\, (1 - x_2) - \beta_2\, x_2 - \kappa\, x_2^{2/3}\, x_3^{2/3}$$

$$\frac{dx_3}{dt} = \alpha_3\, x_2 - \beta_3\, x_3. \tag{55}$$

In eqs. (3), the gating variable x_2 represents the opening of the ion channel gated by the co-receptor Orco [50]. The opening of the co-receptor is promoted by the odorant binding variable x_1, which interacts with the gating variable x_3 through a feedback loop involving a

calcium channel [48]. The inhibitory term $\kappa\, x_2^{2/3}\, x_3^{2/3}$ models the calcium feedback with κ as a constant. Finally, the parameters α_2, β_2 define the rate of increase and decrease of Orco gating x_2, while α_3, β_3 represent the rate of increase and decrease of calcium gated by x_3. Altogether, the transduction current I resulting from this odorant transduction processed is given as a Hill function of the co-receptor gating variable x_2:

$$I = \frac{I_{max}\, x_2}{x_2 + c^p}, \tag{56}$$

where I_{max} defines the maximum transduction current that can result through the co-receptor channel. The parameters c and p define the half-activation coefficient and Hill coefficient of the co-receptor channel respectively. The different steps of the transduction cascade are illustrated in Figure 17C for an odor ramp featuring a linear increase in odor concentration interrupted by a gap.

Spike Generator Model

In the biophysical cascade model [48], the Connor-Stevens model was used to simulate the transformation of transduction current into biological spikes. Here, we adopt the framework of the Qian 3D model [49], which was proposed to describe depolarization block in midbrain dopamine neurons. Like the original Hodgkin-Huxley model [51], the formulation of Qian *et al.* [49] is a single compartment neuron model with three currents: fast sodium I_{Na}, delayed rectifier potassium I_K, and a leak current I_{leak}:

$$
\begin{aligned}
I_{Na} &= g_{Na}\, m^3\, h\, h_s\, (V - E_{Na}) \\
I_K &= g_K\, n^3\, (V - E_K) \\
I_{leak} &= g_{leak}\, (V - E_{leak}).
\end{aligned}
\tag{57}
$$

In the above equations, E_{Na}, E_K and E_{leak} are the respective Nernst potentials of each channel. g_{Na}, g_K and g_{leak} are parameters modelling the maximal conductance per unit area of each channel. Symbols n, m, h and h_s are dimensionless state variables mediating the gating of the three currents, modelled as time dependent functions of the membrane potential V. For simplicity, the gating variable for sodium activation (m) is set to its steady state value as it is significantly faster than the other gating variables, while the gating variable for potassium activation (n) is dynamically yoked to the timescale of the gating variable h [49]. Thus, the Qian 3D model contains three state variables: V, h, and h_s. The feature of the Qian 3D model that distinguishes this work from other models is the distinction between fast inactivation (h) and slow inactivation (h_s) in the sodium current as a mechanism for explaining the dynamics of depolarization block. The Qian 3D model consists of the following system of ordinary differential equations:

$$
\begin{aligned}
\frac{dV}{dt} &= I - I_{Na} - I_K - I_{Leak} \\
\frac{dh}{dt} &= -(h - h_\infty)/\tau_h \\
\frac{dh_s}{dt} &= -(h_s - h_{s,\infty})/(\rho\tau_{h_s}),
\end{aligned}
\tag{58}
$$

where h_∞ and $h_{s,\infty}$ are voltage-dependent steady state values of the fast and slow inactivation variables associated with the sodium channels. Variables τ_h and τ_{h_s} are voltage-

dependent time constants that modulate the rate of inactivation (the parameters and exact definitions of each gating variable can be found in Table S4 of ref. [5]). Together, these variables determine the rate at which the spike amplitude and frequency changes during depolarization block. In particular, the scaling parameter ρ of the time constant τ_{h_s} modulates the duration for which spiking continues upon the onset of depolarization block. The dynamics of the variables of the spike-generator model is illustrated in Figure 17D and Figure 17F for two representative odor stimuli.

Variability and noise in the spiking activity of the Or42b OSN:

As illustrated by the bifurcation diagram of the OSN model in Figure 23B, the OSN is silent when unstimulated. However, we observe experimentally that basal activity is present on the order of 1-5 Hz even when no olfactory signal is present (Figure 17A), which is consistent with previous observations [23], [52]–[56]. To replicate the basal firing rate of the OSN in absence of odor stimulation, we assume that noise affects the olfactory transduction cascade model of the OSN. We model this by injecting Gaussian noise $\varepsilon \sim N(0, \sigma)$ at the level of the transduction current to simulate basal activity of the OSN in the absence of olfactory input, such that $I \rightarrow I + \varepsilon$. The value of the basal noise σ is modelled by fitting the distribution of firing rates that are observed in the OSN in the absence of odor, by finding σ that minimizes the Kullback-Leibler divergence between recorded and simulated firing rate distributions (as shown in Figure 17A).

In addition, we noted the existence of variability in the sensitivity to odor across experimental trials. This was particularly apparent in conditions displaying depolarization

block, as we observed the OSNs of each animal were firing or silent over different time intervals (Figure 24B-C and Figure 25B). As the variability in OSN responses could not be reproduced with basal noise alone and may be due to variability in olfactory sensitivity across animals, we also assume that each OSN trial we simulate differs slightly in its model parameters. We model this effect by adding uncertainty to the maximum transduction current I_{max} of the OSN in each simulated trial, such that $I_{max} \rightarrow I_{max}(1 + \delta_I)$, where $\delta_I \sim N(0,0.1)$ is a normally distributed random variable. We empirically found that this variability accounted for the sequential onset of depolarization block observed across different experimental trials, such as for 10 μM step stimulus of ethyl butyrate (Figure 23D).

Optimization of model parameters

The parameters of the OSN model were fit on a subset of data from electrophysiology recordings. For each condition, the error was defined as the normalized root mean squared error (NRMSE) between the recorded firing rate and predicted firing rate of the model (Table S2). The objective function was the mean error of all conditions in the training set. All parameters were optimized using global optimization toolbox of MATLAB. In the parameter optimization procedure, we matched the number of simulated trials with the existing number of experimental trials. The full list of optimized parameters of the odor transduction model can be found in Table S3 and the optimized parameters of the spike generator model can be found in Table S4. The results are shown in Figure 23 and Figure 24, Figure 25 and Figure 17.

Physical model for odor diffusion

To quantify the sensory experience of larvae in the rectangular arena at different source concentrations of ethyl butyrate (Figure 19E-F), we modelled the diffusion of odor from the reinforcement ring on the lid to the surrounding air (Figure 18). As in previous work [23], the odor gradient was found to be dynamic with an initial period of diffusion from the source center followed by a gradual depletion of the source. To predict the odor gradient perceived by larvae within the behavioral arena for different source concentrations, we used a generalized version of the physical 3D diffusion model developed in [23]. The simulations of the odor diffusion model were conducted with the partial differential equation toolbox of MATLAB, using an arena geometry generated and imported from an open-source CAD software OpenSCAD [57].

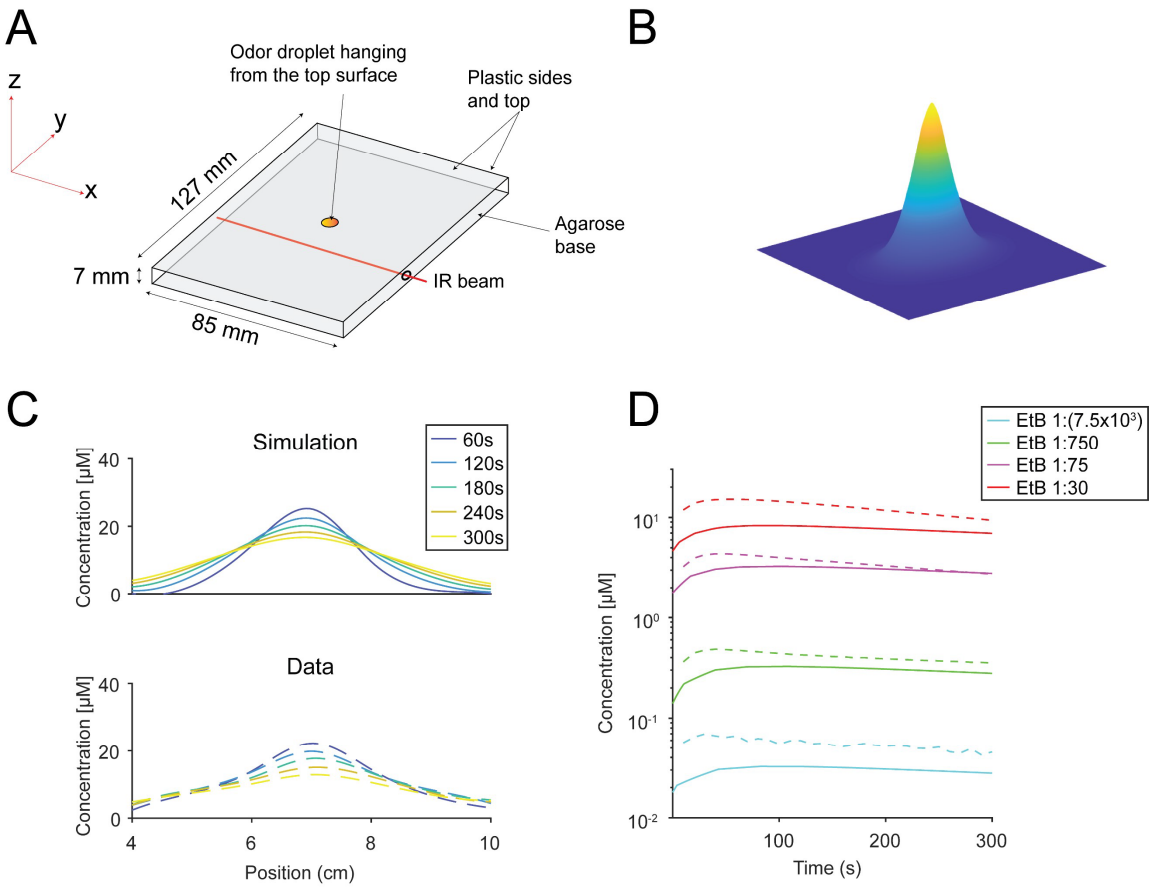

Figure 18: Arena geometry and comparison of simulated odor gradient with measurements. (A) Arena geometry with indicated features used in the simulation, except the IR beam which indicates how the odor intensity was inferred from FT-IR absorption measurements [58]. **(B)** Numerical simulation of odor diffusion from a reinforcement ring on the top surface of the arena (orange disk in panel A). **(C)** Comparison of FT-IR-derived odor concentration profiles (dashed lines) of a high-strength (1:15) source of ethyl butyrate [39] and simulated odor profiles after optimization of the 3D diffusion model (plain lines). **(D)** Comparison of the predicted (plain lines) and measured (dashed line) profiles of odor concentration along the centered cross-section of the arena for various source dilutions.

Diffusion equation and model geometry:

The diffusion processes of the odor within the air and within the droplet are modelled as a diffusion process:

$$\frac{\partial z}{\partial t} = D_i \, \nabla^2 z, \tag{7}$$

where D_i denotes the diffusion constant for either air, D_{air} or the droplet, D_{drop}. A flux continuity condition is applied at the droplet-air boundary on the surface of the droplet. The base of the droplet in contact with the top surface of the arena is modelled as a no-flux boundary. For the interaction of the odor with the plastic surfaces and the agarose surfaces of the arena, we followed the approach described in ref. [23] and modelled adsorption of odor on these surfaces as Robin boundary conditions:

$$\begin{aligned} &\text{Plastic boundary: } -\hat{n} \cdot \vec{J} = k_{plastic}(z_{0,plastic} - z) \\ &\text{Agarose boundary: } -\hat{n} \cdot \vec{J} = k_{agar}\big(z_{0,agar} - z\big), \end{aligned} \tag{8}$$

where $\hat{n}$ is the unit vector in the direction normal to the boundary under consideration. Parameters $k_{plastic}$ and k_{agar} are the reaction rates. $z_{0,plastic}$ and $z_{0,agar}$ are the saturation concentrations of the odorant on the boundary. This boundary condition assumes that desorption at the boundary occurs if the concentration of the odorant in air is less than the saturation concentration, with the boundary acting as an odor source. On the other hand, a higher concentration of the odorant in air would lead to adsorption at the boundary, with the boundary functioning as an odor sink. We noted however that the source concentrations of ethyl butyrate used in some experiments of this study were orders of magnitude smaller than those used in ref. [39]. As a result, the assumption that the plastic and agarose surfaces of the arena act as source terms may not be valid at low source concentrations. In our implementation of the physical 3D diffusion model, we therefore added a conditional

statement to the boundary conditions to account for regions of the arena where saturation at the boundary does not occur:

$$\begin{aligned} &\text{Plastic boundary: If } z < z_{0,plastic},\ -\hat{n}\cdot\vec{J} = 0 \\ &\text{Agarose boundary: If } z < z_{0,agarose},\ -\hat{n}\cdot\vec{J} = 0 \end{aligned} \tag{9}$$

The geometry of the experimental arena is shown in Figure 18A. The rectangular arena has a width of 8.5 cm and a length of 12.7 cm. The height of the arena from the lid to the base of the agarose surface is 0.7 cm. The geometry of the droplet on the lid can be viewed as an inverted half sphere hanging from the top surface of the arena. For simulation purposes, we approximated the droplet as a cone, with a radius of $r_{drop} = 0.3$ cm with a height of $h_{drop} = 0.1$ cm. The droplet therefore has a volume of $V_{drop} = \frac{\pi}{3} r_{drop}^2 h_{drop} \approx 10$ μL. We assume that the initial odorant concentration in the air is zero, while the initial odorant concentration in the droplet is equivalent to the applied source concentration. Thus, the flux of odor at the droplet-air boundary is proportional to the applied source concentration. In each simulation, the odorant diffuses from the droplet into the air over a duration of 30 seconds before each animal is introduced into the arena.

The parameters of the model were fit to match measurements made by Fourier transform-infrared spectroscopy (FT-IR) [58]. To capture the evolution of the shape and magnitude of the odor profile, these measurements were made at different cross sections of the arena at different time intervals. To guide the parameter optimization, we used data for ethyl butyrate in an identical arena recorded from a previous study [39] at source concentrations of 1:30 and 1:15. Parameter optimization was performed using the global

optimization toolbox of MATLAB by minimizing the normalized root mean squared error (RMSE) between the simulated odor concentration to FT-IR spectroscopy measurements. After parameter optimization, we then validated the model with new FT-IR measurements recorded at source dilutions of 1:7.5x10^3, 1:750, 1:75, and 1:30 along the center cross section of the arena (Figure 18D). The 3D diffusion model was found to scale well across orders of magnitude in the source concentration. Parameters of the computation model for 3D odor diffusion can be found in Table S5.

Results

Olfactory sensory neurons undergo depolarization block when stimulated by ethologically-relevant odor concentrations

Fruits that are attractive to *Drosophila melanogaster* emit complex blends of odorant molecules that include esters detected by the *Or42b*-expressing olfactory sensory neurons (OSN) [59]. When exposed to a piece of ripe banana, wild-type larvae quickly locate the source of the odor through directed navigation (Figure 19A-C), as shown in previous work with pure odors [58], [60]–[62]. A drastically different behavior was observed in larvae with olfactory inputs limited to a single OSN by selectively rescuing the expression of the odorant co-receptor ORCO in the *Or42b* OSN of anosmic *Orco* null (*Orco*$^{-/-}$) mutant larvae [63] (see Methods). Instead of locating and readily entering the piece of banana, *Or42b* single-functional (*Or42b* SF) larvae circled at an intermediate distance to the source between the full attraction of wild type and the non-attraction of anosmic larvae (Figure

19B-C). Using an assay where the odor diffusion can be quantified in gaseous phase [58] and modeled numerically [23], we established that wild-type larvae are attracted to ethyl butyrate —a fruity ester released by ripe banana [59], [64] — over a relatively wide range of concentrations (Figure 19D-F). By contrast, *Or42b* SF larvae were repelled by the odor source at high strengths (1:150 and 1:100 source dilutions) that are strongly attractive to wild-type larvae (Figure 19E-F). To confirm this unexpected result, we developed a new genetic strategy to inhibit synaptic transmission in all OSNs except the *Or42b* OSN through selective expression of the tetanus toxin light chain (TNT) [65] (see Figure S1F of ref. [5]). As for the regular *Or42b* SF larvae, we observed that larvae with all but their *Or42b* OSNs functionally impaired are repelled by a source of ethyl butyrate at high strength.

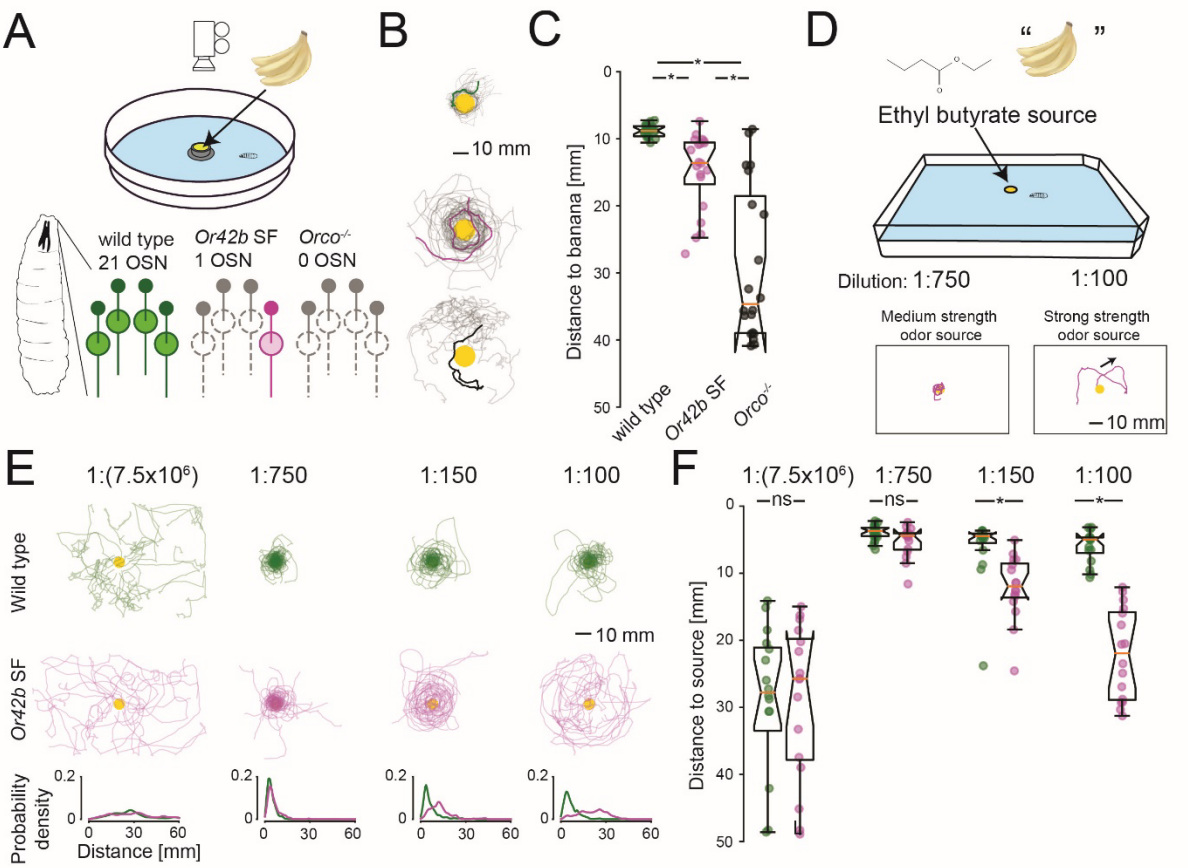

Figure 19: *Drosophila* larvae with a single OSN are attracted to a food source but unable to reach it. (A) Schematic of banana olfaction assay (top). Schematic of larval olfactory systems with full and genetically-manipulated functionality (bottom). **(B)** Trajectories produced by wild type (top), *Or42b* SF (middle), and anosmic *Orco* null (*Orco* $^{-/-}$) mutant (bottom). The yellow disk indicates position of the fruit cup. **(C)** Quantification of distance to cup of wild type (green, n = 20), *Or42b* SF (magenta, n = 20), and *Orco* $^{-/-}$ mutant (gray, n = 20). Statistical differences between genotypes were tested using Kruskal-Wallis H test, followed by Conover-Iman test (*P < 0.05). **(D)** Schematic of assay featuring a single odor source (top). Illustrative trajectories of *Or42b* SF in response to an ethyl butyrate source of medium (1:750) and strong (1:100) strengths. **(E)** Trajectories produced by wild-type (top) and *Or42b* SF (middle) larvae at the indicated source dilutions of ethyl butyrate. Probability density functions of distance to source (bottom) for wild type (green) and Or42b SF (magenta). (F) Pairwise comparisons between wild-type and *Or42b* SF behaviors using Wilcoxon rank sum test (*P < 0.05 upon Bonferroni correction).

To define the basis of the concentration-specific attraction mediated by the *Or42b* OSN, we used suction electrode recordings (Figure 20A) to monitor the activity of the *Or42b* OSN in response to (i) prolonged odor step stimuli at fixed concentrations (Figure 20C-D) and (ii) replays of the time courses of odor concentration experienced by freely-moving larvae in gradients of the ethyl butyrate (Figure 20E-F). For an attractive source dilution ($1:7.5x10^3$), the *Or42b* OSN showed robust firing activity throughout the concentration range of the replay (0.4-1 μM, Figure 20E). Consistent with the response properties of the larval *Or42a* OSN stimulated by dynamic odor profiles [23], the *Or42b* OSN tracked and amplified changes in odor concentration. The OSN dynamics dramatically differed for a stronger odor source (1:150) that elicited behavioral aversion: when stimulated by high-odor concentrations that initially induced strong excitation (>10 μM, Figure 20F), the *Or42b* OSN switched from sustained firing activity to a silent state reminiscent of depolarization block.

For prolonged odor stimulation at fixed concentrations, the firing activity associated with the initial phasic response of the *Or42b* OSN produced a canonical sigmoidal dose-response (Figure 20B, dark blue trace), as reported in previous work [33]. While the firing activity was maintained throughout the 20-second stimulation at odor concentrations lower than 10 μM (Figure 20C), the tonic response of the *Or42b* OSN switched to a block state at concentrations higher than 10 μM (Figure 20B, cyan trace and red arrow; Figure 20D). Even for stimuli of high-odor concentrations, several seconds were necessary for the OSN dynamics to evolve toward depolarization block. But, once developed, the block state persisted throughout the rest of the 20-second odor stimulation.

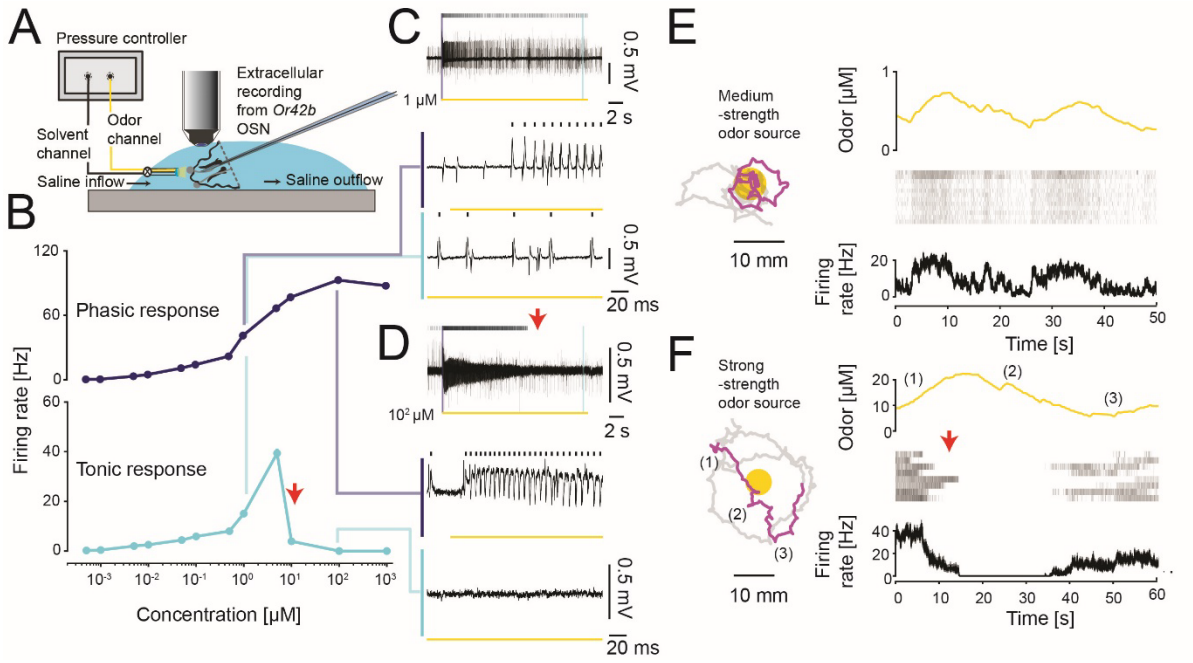

Figure 20: Olfactory sensory neurons undergo depolarization block during chemotaxis. **(A)** Schematic of olfactometer and electrophysiology setup**. (B)** Phasic (top) and tonic (bottom) dose-response profiles of *Or42b* OSN to ethyl butyrate. Data represent mean firing rates ± SEM (500 pM—n=10, 1 nM—n=10, 5 nM—n=10, 10 nM—n=10, 50 nM—n=18, 100 nM—n=18, 1 μM—n=10, 5 μM—n=8, 10 μM—n=9, 100 μM—n=10, 1 mM—n=10). **(C)** Representative recording of *Or42b* OSN stimulated by 1 μM of ethyl butyrate. Raster plot shows the OSN-specific spikes (top). Yellow line below indicates 20-second odor stimulation; thin blue and cyan lines indicate 'phasic response' and 'tonic response', respectively. **(D)** Same as panel C for *Or42b* OSN at 100 μM. **(E)** Replay of concentration time course corresponding to a trajectory segment (magenta) obtained for a medium-strength source ($1{:}7.5\text{x}10^3$, n=12). **(F)** Same as (E) for strong-strength source (1:150, n=8). Red arrow in (D) and (F) indicates onset of depolarization block.

Depolarization block does not arise from inhibition of the olfactory transduction cascade

In the adult *Drosophila*, a feedback loop involving the inhibitory effect of intracellular calcium on the activity of the odorant receptor adaptively regulates the olfactory transduction cascade (*24, 25*). In the larva, modeling suggests that a similar negative feedback contributes to the regulation of the odor-driven activity of the *Or42a* OSN [23], but such feedback is not expected to influence the OSN activity induced optogenetically [63]. To test whether the depolarization block of the *Or42b* OSN stems from a similar negative feedback regulation of the olfactory transduction cascade, we characterized the olfactory behavior of *Or42b* SF larvae expressing the light-gated cation channel ChrimsonR [30] (*Or42b*>Chrimson, Figure 21A-B). For a source of ethyl butyrate at medium strength (1:750), *Or42b*>Chrimson larvae displayed vigorous attraction (Figure 21C-D, left). When combining an odor source of the same strength with a concentric red-light gradient, *Or42b*>Chrimson larvae displayed repulsion (Figure 21C-D, right). We used suction electrode recordings to characterize the response of the *Or42b*>Chrimson OSN stimulated by brief light flashes superimposed onto a step stimulus of ethyl butyrate. For a medium concentration of ethyl butyrate (100 nM and 1 μM), the light flashes elicited reproducible spike trains (Figure 21E). For a high-odor concentration (100 μM) inducing depolarization block, the light flashes did not produce action potentials (Figure 21E). Together, these results indicate that depolarization block of the *Or42b* OSN can be caused by currents originating either from the odorant receptor or from Chrimson, which rules out an inhibitory mechanism that selectively targets the olfactory transduction cascade.

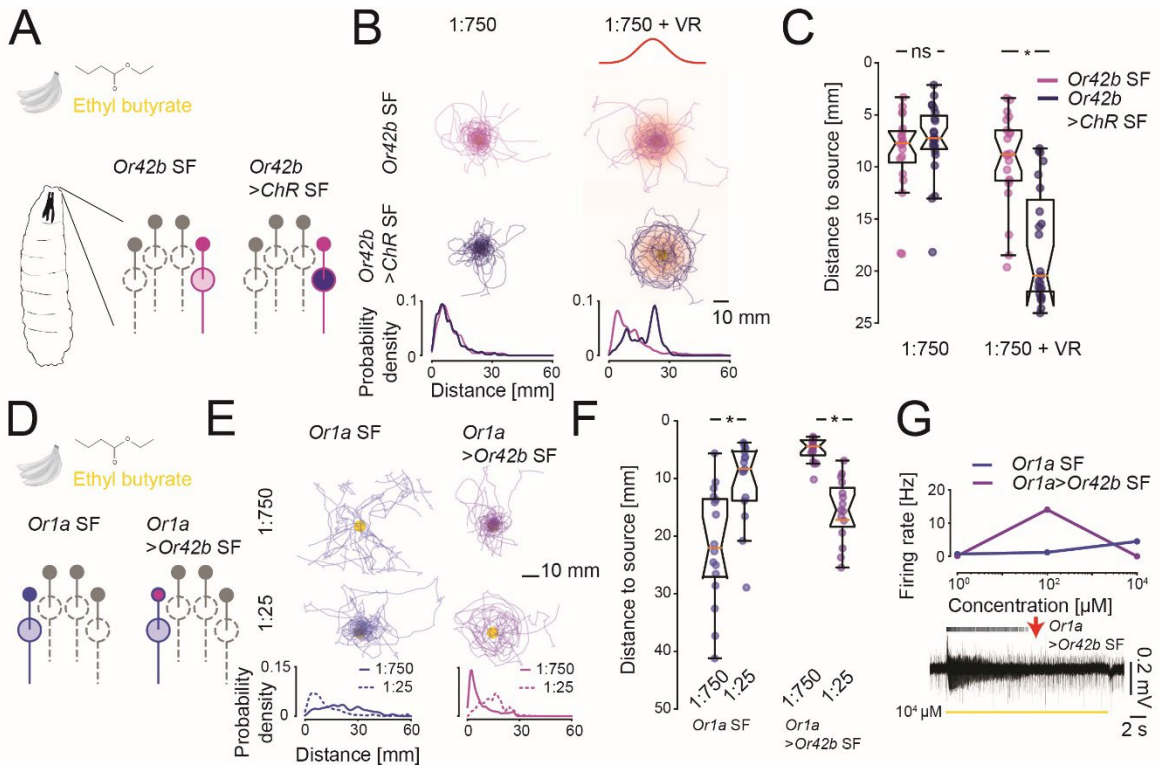

Figure 21: Depolarization block is a property of olfactory sensory neurons. (A) The light-gated cation channel ChrimsonR (red, ChR) is used to test whether the negative feedback involved in regulating the olfactory transduction cascade (orange) is necessary for depolarization block (*24, 25*). **(B)** Expression of ChrimsonR in the *Or42b* OSN. **(C, D)** No difference in attraction level was observed between *Or42b* SF (n=20) and *Or42b>ChR* SF (n=23) without light stimulation. For animals exposed to a virtual light gradient superimposed onto an ethyl butyrate (1:750) gradient, *Or42b>ChR* SF (n=23) is repelled by the gradient peak compared to *Or42b* SF (n=21) (Wilcoxon-ranksum test, *p<0.05 upon Bonferroni correction). VR denotes a virtual light gradient with a peak light intensity of 41 μW/mm^2. **(E)** PSTH of *Or42b>ChR* OSN elicited by prolonged stimulus of ethyl butyrate at a concentration of 100 nM (left, n=12), 1 μM (center, n=10) and 100 μM (right, n=10) with red light flashes of 0.5 second. When the *Or42b* OSN has undergone depolarization block (right), red light flashes fail to elicit action potentials. **(F)** Ectopic expression of OR42b in the *Or1a*-expressing OSN. **(G, H)** *Or1a* SF is significantly less attracted to low-strength (1:750—left, n=16) than high-strength (1:25—right, n=17) sources. Following the ectopic expression of OR42b in *Or1a* SF, larvae become repelled at high source strength (1:25, n=15) compared to medium strength (1:750, n=16). Wilcoxon ranksum test (*p<0.05 upon Bonferroni correction). **(I)** Top: mean±SEM tonic firing rates recorded from *Or1a* SF (1

μM—n=10, 10^2 μM—n=11, 10^4 μM—n=10) and for *Or1a>Or42b* SF (1 μM—n=10, 10^2 μM—n=10, 10^4 μM—n=10). Bottom: representative voltage traces. Red arrow indicates onset of depolarization block. Raster plot reports the OSN-specific spikes and yellow bar indicates timing of odor stimulation. The bottom row of panels C and G show the probability density functions of distance to source.

Depolarization block is commonly observed in larval olfactory sensory neurons

Next, we asked whether depolarization block can be induced in olfactory neurons other than the *Or42b* OSN. To this end, the OR42b receptor was ectopically expressed in the *Or1a* OSN (Figure 21F), a neuron which normally has a low sensitivity to ethyl butyrate [33]. Larvae directed by the endogenous single functional *Or1a* OSN displayed attraction to a very strong (1:25) but not a medium (1:750) source of ethyl butyrate (Figure 21G, blue and Figure S2A of ref. [5]). Upon ectopic expression of OR42b in the *Or1a* OSN (*Or1a>Or42b* SF), the attraction observed for the very strong (1:25) source of ethyl butyrate was converted into repulsion (Figure 21G-H, magenta). In suction electrode recordings, the wild-type *Or1a* OSN responded with a low but significant firing rate to both low and high concentrations of ethyl butyrate (10^2 and 10^4 μM, Figure 21I). Upon ectopic expression of OR42b in the *Or1a* OSN, the *Or1a>Or42b* OSN was strongly activated by low concentrations of ethyl butyrate but underwent depolarization block in the tonic phase when presented with high-odor concentrations (10^4 μM, Figure 21I, red arrow). Therefore, the high conductance of OR42b gated by one of its high-affinity ligands [34], [66] was sufficient to induce depolarization block in an OSN that had an endogenously low affinity to the same odor. This result suggested that any OSN excited by strong transduction currents can switch to a block state.

To establish the relevance of depolarization block for different ligand-odorant-receptor pairs, we selected 4-hexen-3-one — a fruity-smelling ketone with a high-affinity for the OR42a odorant receptor [33] (Figure 22A). While strong attraction was observed in *Or42a* SF larvae at a source of medium strength ($1{:}9x10^4$), strong aversion was triggered by a stronger source ($1{:}9x10^2$) (Figure 22B-C). Larvae followed concentration isoclines — they circled — around a strong source of 4-hexen-3-one, driven by the attraction to the odor at low concentrations and its aversion at high concentrations (Figure 22B). Electrophysiological recordings of the *Or42a* OSN revealed that depolarization block is elicited at high concentrations of 4-hexen-3-one (Figure 22D, red arrow). Next, we generalized the relevance of depolarization block to a third odorant receptor, OR13a, which recognizes the fruity ester pentyl acetate [34] (Figure 22E). While *Or13a* SF larvae are attracted by a source of pentyl acetate at medium strength ($1{:}7x10^2$), the same larvae are repelled by a stronger (1:23) source (Figure 22F-G). Behavioral aversion correlated with the onset of depolarization block when the *Or13a* OSN was stimulated by a high concentration of pentyl acetate (Figure 22H, red arrow). For all conditions that elicited repulsion at high-odor concentrations leading to circling behavior in single functional OSN larvae, we verified that wild-type larvae displayed strong attraction whereas anosmic larvae showed no signs of attraction (see Figure S2 of ref. [5]).

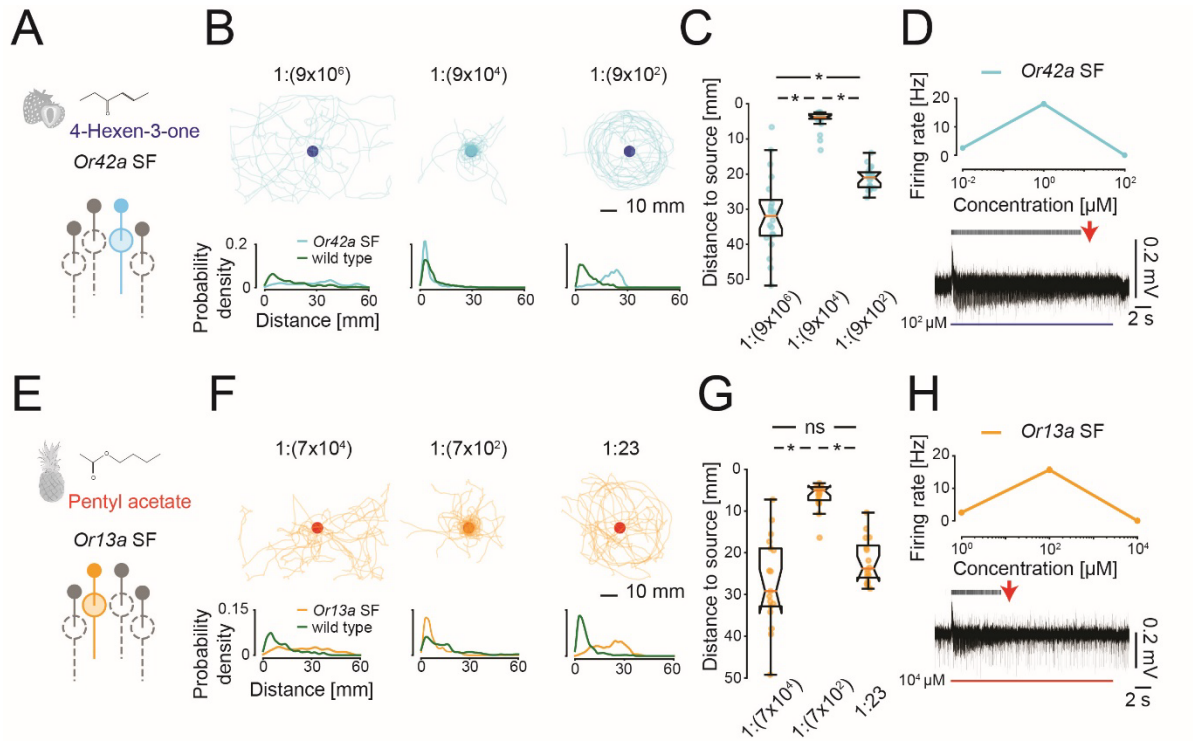

Figure 22: Depolarization block induced with high-affinity ligands in different OSNs. **(A)** *Or42a* SF larvae tested with sources of 4-hexen-3-one. **(B)** Trajectories recorded for *Or42a* SF larvae for sources (blue disks) of different strengths. **(C)** Attraction of *Or42a* SF larvae to 4-hexen-3-one at a medium-strength source (1:9x10^4, n=21), but repulsion at a higher-strength source (1:9x10^2, n=19). **(D)** Top: mean±SEM tonic firing rates recorded of *Or42a* OSN (10 nM—n=10, 1 μM—n=10, 100 μM—n=10). Bottom: representative voltage traces. Red arrow indicates onset of depolarization block. Raster plot reports the OSN-specific spikes and blue bar indicates timing of odor stimulation **(E)** *Or13a* SF larvae tested with sources of pentyl acetate. **(F)** Trajectories recorded for *Or13a* SF larvae for sources (red disks) of different strengths. **(G)** Attraction of *Or13a* SF to pentyl acetate source of medium strength (1: 7x10^2, n=17), but repulsion for high-strength source (1:23, n=16). **(H)** Same as panel D for mean±SEM tonic firing rates for *Or13a* OSN (1 μM—n=10, 100 μM—n= 10, 10 mM—n=10). In panels C and G, statistical comparisons were conducted with Kruskal-Wallis H-test followed by Conover-Iman test (*p<0.05 upon Bonferroni correction). The bottom row of panels B and F show the probability density functions of distance to source.

A computational model elucidates the mechanistic origin of depolarization block in olfactory sensory neurons

In dopamine neurons of the midbrain of rats, depolarization block is mediated by the cumulative effects of slow inactivation of the voltage-gated sodium channels [49]. Given that the depolarization block affecting an OSN does not appear to be caused by negative regulation of the olfactory transduction cascade (Figure 21A-E), we speculated that the block of OSNs resulted from the inhibition of sodium channels associated with the spike-generation machinery. In *Drosophila*, voltage-gated sodium channels are thought to be the products of complex patterns of alternative splicing of a single gene called *paralytic* [67], [68]. As described in Figure 23A-B, we developed a computational model for the larval *Or42b* OSN that combines a realistic olfactory transduction module [48] with a conductance-based neuron model modified to account for the slow inactivation of sodium channels [49]. The free parameters of the model were optimized to fit the responses of the *Or42b* OSN stimulated by dynamic odor ramps created with a microfluidics system (Figure 23C and Figure 24A) together with a subset of dose responses elicited by concentrations ranging from subthreshold to high activity yielding depolarization block (Figure 23D and Figure 24B).

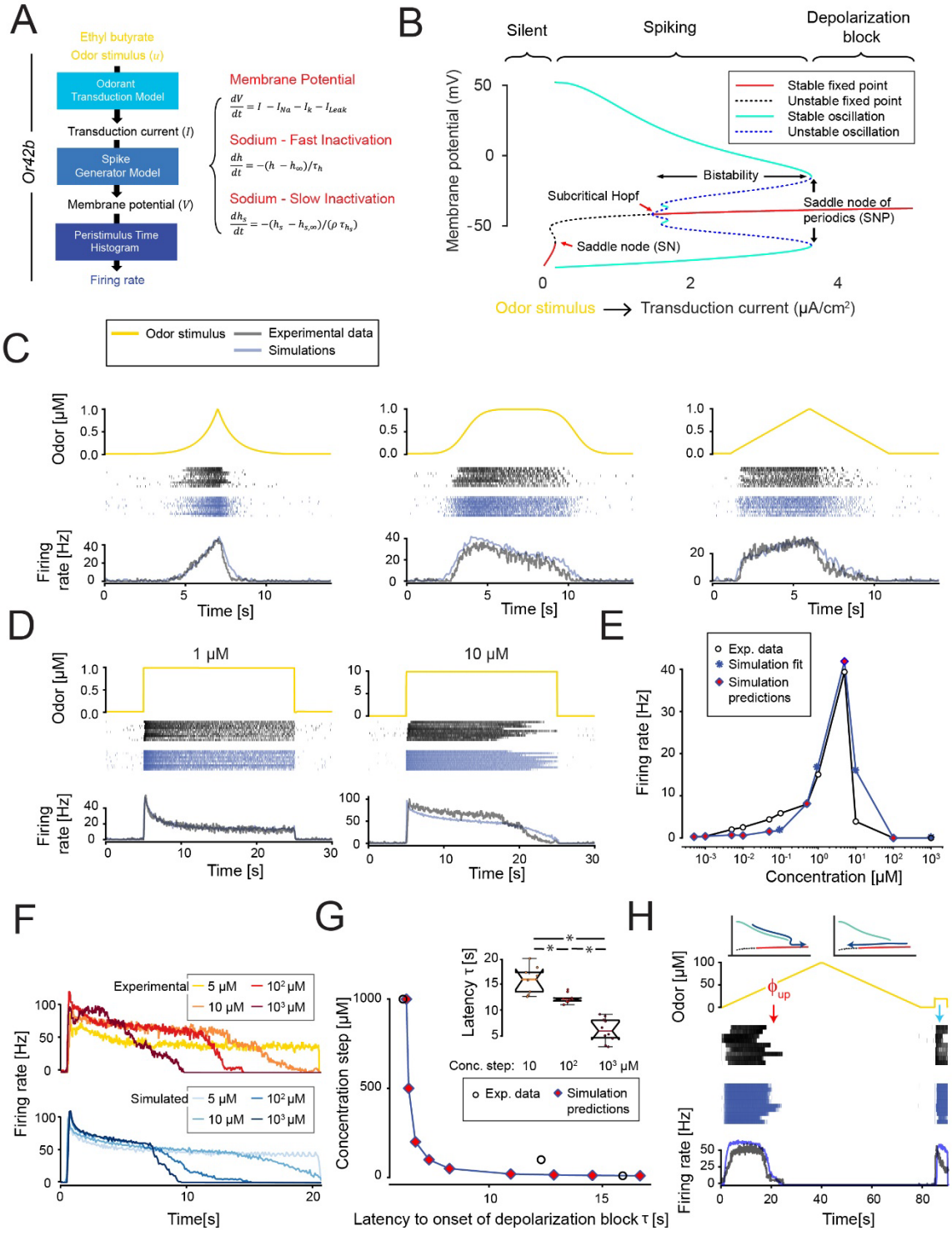

Figure 23: Development and validation of a computational model reproducing depolarization block in *Or42b* OSN stimulated by ethyl butyrate. (A) Framework of the

integrated *Or42b* OSN model accounting for the conversion of an odor stimulus into the generation of action potentials through the cascade of an odorant transduction model followed by a spike generator model. **(B)** Bifurcation diagram of the *Or42b* OSN model. The spiking regime terminates at the saddle node of periodics (SNP) bifurcation. **(C-D)** Experimental data (black) used for model fitting (blue) (exponential ramp—n=10, sigmoid ramp—n=8, linear ramp—n=10, 1 μM—n=10 and 10 μM—n=9). **(E)** Dose responses of mean tonic firing rates of real (white circles) and simulated *Or42b* OSN. Blue stars indicate conditions used for model fitting. Red diamonds represent predictions of the model. Sample sizes: 500 pM—n=10, 1 nM—n=10, 5 nM —n=10, 10 nM—n=10, 50 nM—n=18, 100 nM—n=18, 500 nM—n=10, 1 μM—n=10, 5 μM—n=8, 10 μM—n=9, 100 μM—n=10 and 1 mM—n=10. **(F)** Experimental (top) and simulated (bottom) dynamic toward depolarization block for different odor concentrations (5 μM, 10 μM, 100 μM and 1 mM). **(G)** Quantitative relationship between the latency to depolarization and the concentration of the odor simulations for experimental data (white circles) and model predictions (red diamonds). Inset: boxplots of latency to depolarization block for different odor stimulations (Kruskal Wallis test followed by Conover-Iman test, *$p<0.05$). **(H)** Hysteretic nature of *Or42b*-OSN firing rate dynamics in the response to a slow linear odor ramp of ethyl butyrate (n=9 recordings). ϕ_{up} denotes the concentration where depolarization block arose during the up-gradient phase of the ramp. The cyan arrow highlights the effect of the odor stimulation, which brings the OSN dynamics back to a firing regime (limit cycle).

The integrated *Or42b* OSN model recapitulated the dynamical properties of the firing activity of the real OSN (Figure 23, Figure 24 and Figure 25). When stimulated with high concentrations of ethyl butyrate (10 μM), the model of the *Or42b* OSN underwent depolarization block (Figure 23D). The model led to predictions of the firing activity of *Or42b* OSN in excellent quantitative agreement with the experiments for odor steps below and above the threshold for depolarization block (predictions shown as red diamonds, Figure 23E). In particular, the model accurately predicted sustained firing rate at ~5 μM and the occurrence of depolarization block at 100 μM. In the real *Or42b* OSN, we observed that the latency to the onset of depolarization block decreased as a function of the concentration of the odor stimulation (Figure 23F-G). Remarkably, the OSN model accounted for the

quantitative relationship observed between the latency to depolarization block and the stimulus concentration (Figure 23G). When stimulated by a replay of the concentration time course that elicited behavioral aversion in Figure 20F, the OSN model entered and exited a depolarization block state with dynamics like the real OSN (Figure 25B).

In the framework of dynamical systems theory [69], a stable limit cycle corresponds to the neuron firing periodic action potentials, and a stable fixed point corresponds to the absence of action potentials (i.e., depolarization block). To inspect the dynamical properties of the OSN model, we computed the bifurcation diagram shown in Figure 23B where the concentration of the odor determines the transduction current (Figure 23A). The bifurcation diagram establishes the existence of a bistable domain of odor concentrations below the so-called saddle node of periodics (SNP) threshold where depolarization starts. In the bistable domain, the OSN can adopt either a periodic behavior where it fires sustained trains of action potentials or a state of depolarization block. The exact state of the system depends on its history (hysteresis): if the *Or42b* OSN is stimulated by increasing odor concentrations, it will maintain a regime of persistent firing activity until the SNP threshold is passed; by contrast, the *Or42b* OSN can remain in a state of depolarization block while decreasing odor concentrations bring the transduction current from values higher than the SNP threshold to lower values located within the bistability domain (Figure 23B).

To experimentally test the existence of the predicted hysteresis in the response of the *Or42b* OSN, we stimulated the real neuron with a slow linear odor ramp ranging from 0 to 100 μM, which encompassed concentrations well below the detection threshold and well above the SNP threshold. Based on Figure 23E, we expected that the SNP threshold would

correspond to a concentration higher than 10 μM. We found that, indeed, the firing activity of the real *Or42b* OSN increased monotonically up to a threshold value (ϕ_{up} ~50 μM) where it switched to a state of depolarization block. During the down-gradient phase of the odor ramp, the firing activity of the OSN was not restored until the end of the concentration ramp. More specifically, the OSN remained silent for concentrations ranging between ϕ_{up} and 0 μM where strong firing activity was observed during the up-gradient phase of the ramp — a hallmark of hysteretic dynamics.

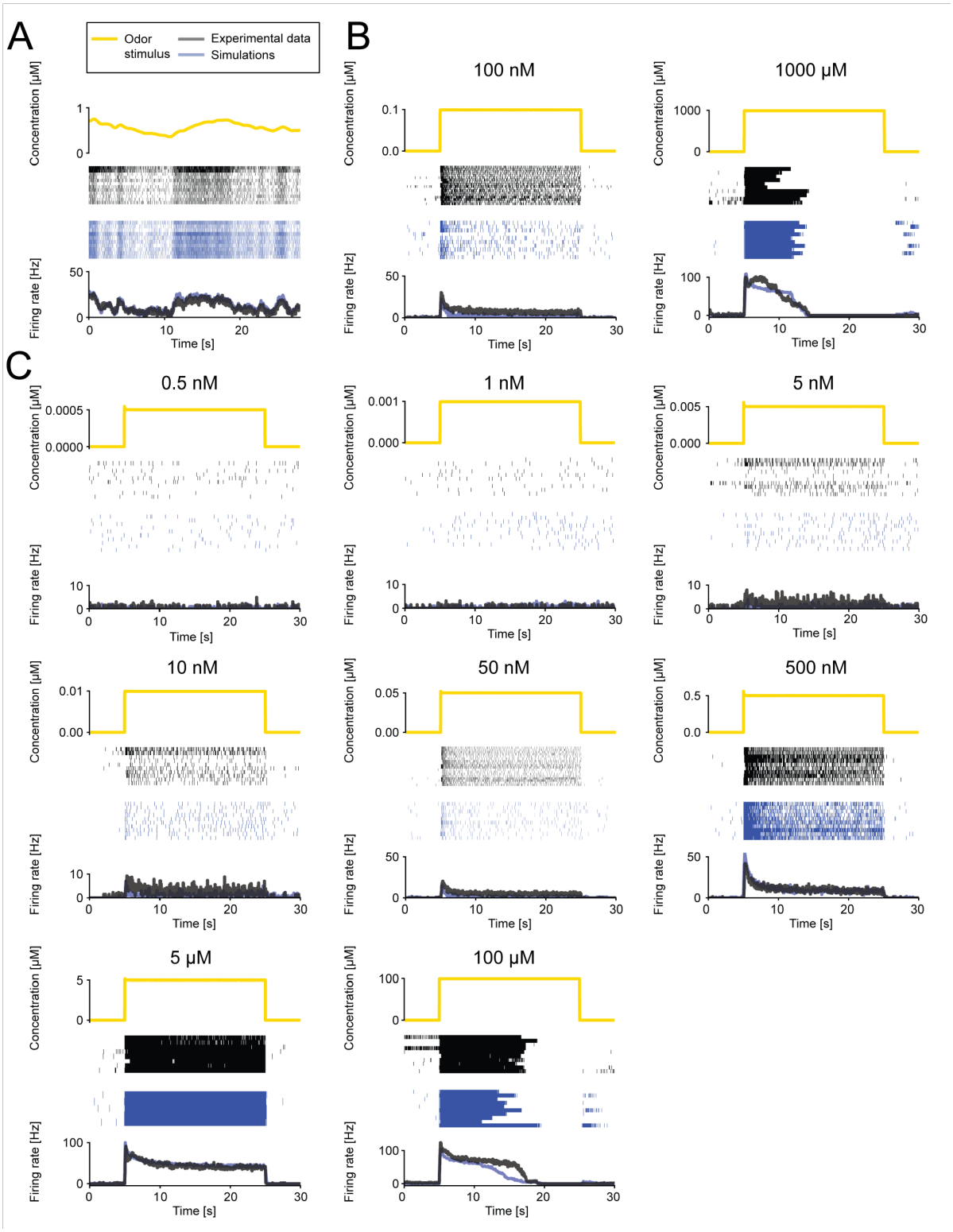

Figure 24: Additional conditions used to train and validate the *Or42b* OSN model in response to ethyl butyrate. (A) Training set: Replay of trajectory segment corresponding to

the attractive behavior shown in Figure 20E (partial time course). Experimental data (black) and simulated responses (blue). **(B)** Training set: Prolonged odor step stimuli of low (100 nM) and very high (1000 μM) concentrations used to fit the parameters of the *Or42b* OSN model. (C) Validation dataset of the model: Predictions of the model (blue) and experimental data (black) for the firing rate activity of the *Or42b* OSN data in response to a 20-s prolonged odor stimulation for increasingly high odor concentrations. This training dataset includes Figure 23C-D. The validation dataset includes conditions shown in Figure 23E-H and Figure 25.

The history-dependence of the OSN response to the slow linear odor ramp was reproduced by the model with remarkable accuracy (Figure 23H, blue). During the up-gradient phase of the ramp, the OSN model maintained a strong firing activity until the transduction current crossed the SNP threshold and switched from a stable periodic orbit (spiking activity) to a fixed point (depolarization block) (Figure 23B). Starting with a transduction current above the SNP threshold, the down-gradient phase of the ramp induced a shift of the system's state along the branch of the fixed points, which maintained the state of stable depolarization block —or quasi-stable depolarization block below the subcritical Hopf— while the transduction current decreased to the silent range (Figure 23B). When the concentration increased again at the end of the ramp, the transduction current returned to a value above the saddle node (SN) threshold, which restored the firing activity of the neuron. Following the same logic, hysteresis was observed when the real and simulated *Or42b* OSNs were stimulated by a series of three concentrations steps below and above the SNP threshold that locked the system in a state of depolarization block (Figure 25C).

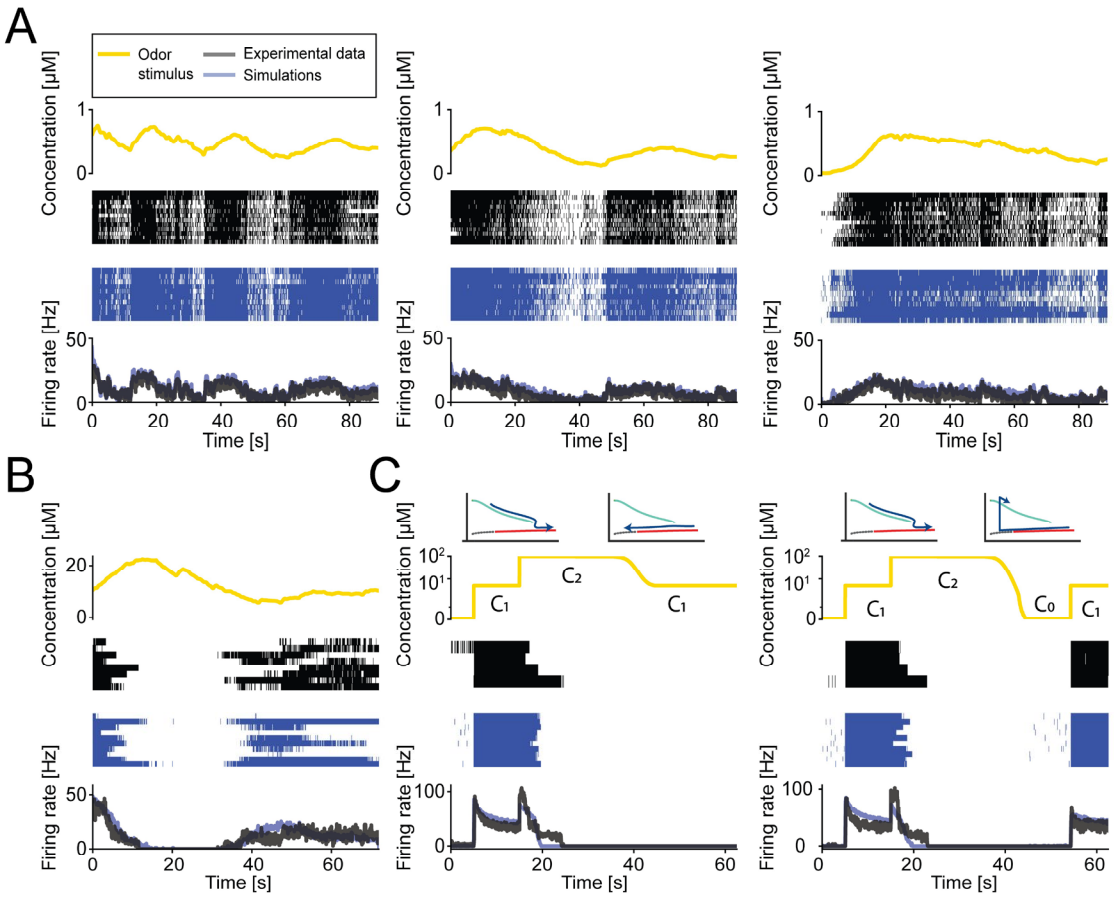

Figure 25: Additional conditions used to validate the *Or42b* OSN model in response to ethyl butyrate. (A) Predictions of the *Or42b* OSN model on trajectories from behavioral replays with concentration below depolarization block threshold (n=12 trials). **(B)** Same as panel A with concentration replay above depolarization block threshold (n=8 trials). **(C)** Stimulation protocol designed to reveal the hysteretic nature of the OSN dynamics. Combination of step conditions bringing the system into a depolarization block state at a super-threshold concentration C_2 (fixed point in Figure 23B) followed by a decrease to a sub-threshold concentration C_1 maintaining the OSN in block state. The same concentration C_1 led to sustained firing activity at the start of the stimulation when the system started in the limit-cycle (firing) regime. Upon depolarization block induced by concentration C_2, firing activity of the OSN can be restored when the odor concentration is brought back to 0 μM for several seconds, which forces the OSN back to its limit cycle regime. The top inserts illustrate the state of the system in the bifurcation diagram of Figure 23B. Recordings for the two step combinations were paired (conditions C_1-C_2-C_1 and C_1-C_2-C_0-C_1 were recorded one after the other, n=4 trials). Throughout the figure, experimental data are shown in black and simulations are shown in blue.

Partitioning of the odor concentration by the activity domains of olfactory sensory neurons

The implication of the depolarization block is that high-sensitivity OSNs that are strongly activated at low concentrations of an odor can drop out from the subset of active OSNs at high concentrations of the same odor. To test this hypothesis, we screened published response profiles of larval OSNs [33], [34] to identify pairs of neurons with different sensitivities to the odors studied in Figure 19, Figure 21 and Figure 22 and compared their respective contribution to chemotaxis across concentration ranges. As illustrated in Figure 19, ethyl butyrate is a high-affinity ligand of the odorant receptor OR42b [34]. By contrast, OR1a has a low affinity for this odor. For strong sources of ethyl butyrate (1:150 and higher) eliciting repulsion in *Or42b* SF larvae (magenta) compared to wild type (green), *Or1a* SF larvae (blue) displayed increasingly strong attraction (Figure 26A and Figure S5A of ref. [5]). Consistent with this behavior, the firing activity of the *Or1a* OSN was higher than baseline at concentrations where *Or42b* OSN underwent depolarization block (Figure 26B and Figure S6A of ref. [5]). This observation suggested that the ectopic expression of the OR42b odorant receptor in all 21 OSNs should elicit repulsion at high concentrations of ethyl butyrate while wild-type larvae remained attracted (Figure 26A, 1:75). We confirmed this prediction experimentally (Figure S7 of ref. [5]).

The same relay principle applied to the *Or13a* and *Or42a* OSNs in response to pentyl acetate. While *Or13a* SF larvae (orange) were attracted by sources of pentyl acetate at medium strengths ($1:7x10^3$ and $1:7x10^2$), attraction was elicited in *Or42a* SF larvae (blue) for strong sources (1:70 and higher) that induced repulsion in *Or13a* SF larvae (Figure 26C

and Figure S5B of ref. [5]). In agreement with the behavior, the firing activity of the *Or13a* OSN underwent depolarization block at high-odor concentrations while *Or42a* OSN showed sustained firing activity (10^4 μM) (Figure 26D and Figure S6B of ref. [5]). The detection of 4-hexen-3-one involves a sensory sequence of three OSNs to recapitulate the wide range of attraction of wild-type larvae (Figure 26E and Figure S5C-D of ref. [5]). In response to this odor, *Or42a* SF larvae (cyan) were attracted by sources at low strength ($1{:}9x10^4$) but repelled at medium and high strengths ($1{:}9x10^2$ and higher) for which *Or42b* SF larvae (magenta) became attracted (Figure 26E and Figure S5C of ref. [5]). When *Or42b* SF larvae showed signs of repulsion (1:4), *Or1a* OSN larvae (blue) showed a stark increase in attraction to the source. The dose responses of the firing activity of *Or42a*, *Or42b* and *Or1a* OSNs mirrored this behavioral sequence with *Or42a* and *Or42b* OSNs undergoing depolarization block at medium and high concentrations, respectively (Figure 26F and Figure S6C of ref. [5]).

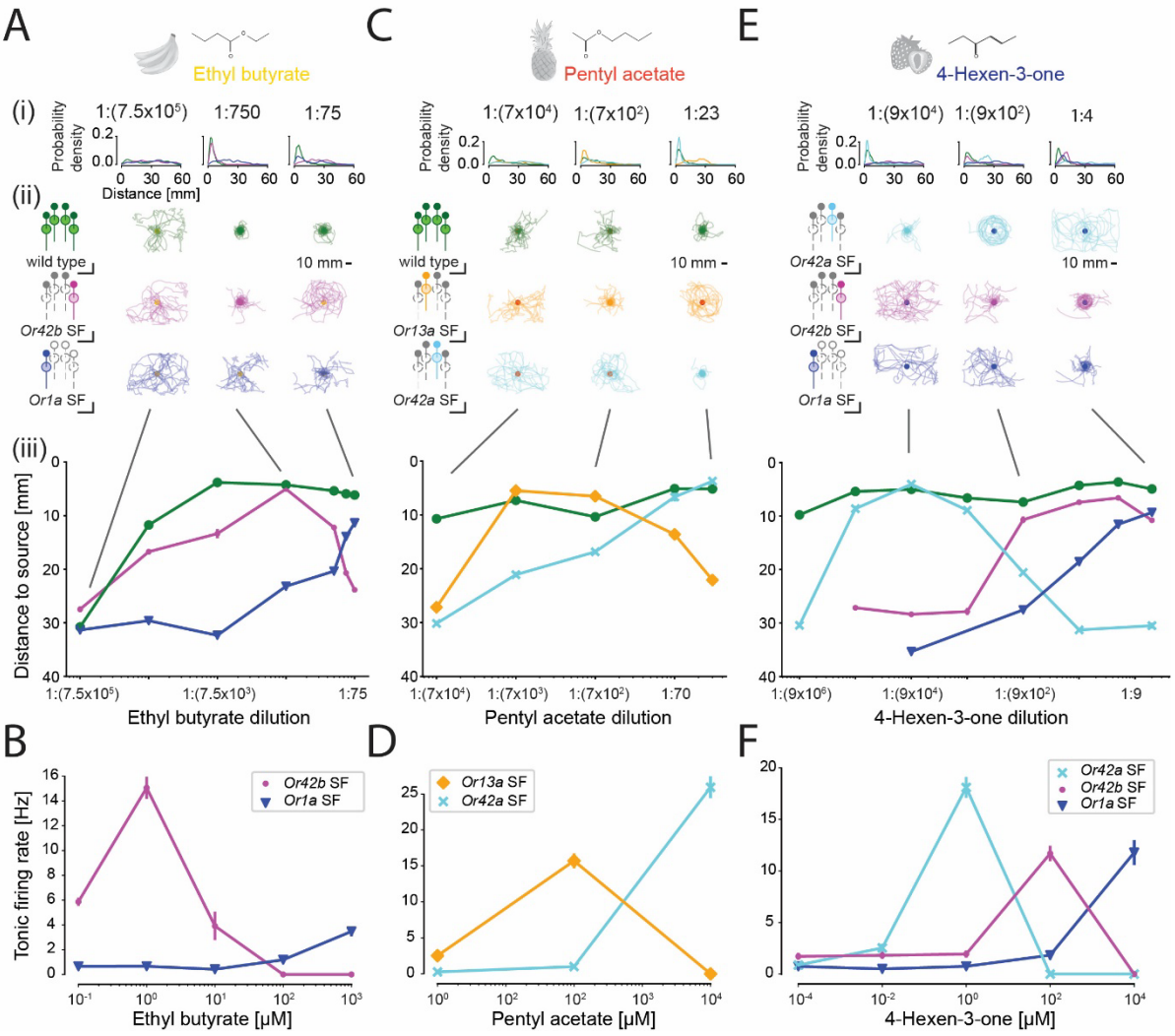

Figure 26: Depolarization block maintains sparse odor encoding by tiling the activity domains of OSNs responsive to the same odor. (A) Behavioral response of wild type (green), *Or42b* SF (magenta) and *Or1a* SF (blue) to a series of ethyl butyrate sources of increasingly higher strength. (Ai) Probability density function of distance to source for the trajectories shown in panel Aii. (Aiii) While *Or42b* SF is strongly attracted by source of medium strength (1:750), attraction dramatically decreases for high-strength source (1:75). By contrast, the attraction level of *Or1a* SF increases monotonically from low to high-strength sources (mean±SEM). **(B)** In electrophysiology recordings, *Or42b* OSN enters depolarization block for odor concentrations where *Or1a* OSN shows robust and persistence firing activity. **(C)** Behavioral responses of wild type (green), *Or13a* SF (orange) and *Or42a* SF (cyan) to pentyl acetate sources of increasingly higher strengths. *Or13a* SF displays attraction at medium-strength sources ($1:7x10^3$—$1:7x10^2$) but it is repelled at high-strength source (1:70) that produces attraction in *Or42a* SF. **(D)** *Or13a* OSN enters depolarization

block for odor concentrations where *Or42a* OSN shows robust and persistent firing activity. **(E)** Behavioral responses of wild type (green), *Or42a* SF (cyan), *Or42b* SF (magenta) and *Or1a* SF (blue) to 4-hexen-3-one sources of increasingly higher strengths. *Or42a* SF is attracted to sources at low strength ($1{:}9x10^{4}$) but repelled at medium strength ($1{:}9x10^{2}$) where *Or42b* SF shows attraction. While *Or42b* SF displays signs of repulsion to a source of very high strength (1:4), *Or1a* SF demonstrates an increase in attraction. **(F)** The *Or42a* and *Or42b* OSNs enter depolarization block at a range that qualitatively match the behavior shown in panel E. The *Or1a* OSN shows robust and persistent firing activity at the highest tested concentration (10 mM). Throughout the figure, firing rates are presented as means±SEM. See Data S1 for sample sizes and p-values.

Discussion

Consistent with the observations that odors activate a subset of OSNs [34], [70]–[74], the results of Figure 26 indicate that the sequential recruitment of OSNs with different affinities to the same odor expands the dynamic range of the larval olfactory system. But contrary to the conventional view, we find that the activity of high-affinity OSNs is not necessarily maintained in the representation of an odor across a wide range of concentrations (Figure 27). Our observations are likely to generalize beyond the larva since there is growing evidence in the literature that OSNs of adult flies [27], [75], mice [76], [77] and rats [78] undergo depolarization block at high-odor concentrations. Moreover, depolarization block has been observed in response to the gating of ionotropic glutamate receptor (IR) by odorant molecules [27]. The pruning of high-affinity OSNs at high-odor concentrations has two implications: first, the same odor might activate distinct subsets of OSNs at low and high concentrations, thereby facilitating central processing and discrimination (Figure 27, bottom). These differences might explain shifts in the internal percept of an odor across concentrations, leading to the report of drastic changes in the perceived quality of the same odor at low and high concentrations in humans [79], [80]. Second, there might be a metabolic advantage in keeping the peripheral representations of odors sparse [81].

In the present work, larvae with an olfactory system restricted to a single type of functional OSNs were all attracted to the odor source at low concentrations. However, the valence of the odor appeared to switch from attractive to aversive behavior at high-odor concentrations (Figure 19, Figure 21, Figure 22 and Figure 26). In previous work, we have demonstrated that an abrupt decrease in the firing rate of the *Or42a* OSN below its basal

activity level is sufficient to trigger stopping behavior and aversive reorientation responses [23]. Here, we showed that all tested OSNs undergo depolarization block at high-odor concentrations (Figure 20, Figure 21, Figure 22 and Figure 26). Therefore, we speculate that the change in valence from attraction to repulsion can be explained by a loss of spiking activity in innately attractive OSNs. Remarkably, the aversion caused by the silencing of high-affinity OSNs can be compensated by the activity persisting in other OSNs with lower affinities, as illustrated by the behavior of wild type larvae (Figure 26).

While depolarization block has been associated with abnormal neuronal function and disease conditions [82]–[84], it has been speculated that depolarization block might also contribute to information processing [85], [86]. In the mammalian visual system, depolarization block conditions the differential tuning of intrinsically photosensitive retinal ganglion cells to represent light intensity with high efficiency [87]. We propose that depolarization block enables the representation of chemosensory stimuli at the sensory periphery over several orders of magnitude of concentration. For instance, it might explain why taste neurons with high sensitivity to sodium shut down at high salt concentration where low-sensitivity sodium taste neurons become active and natural attraction to sodium switches to repulsion [88]. Through the recruitment and loss of active sensory neurons, depolarization block creates a previously unknown dimension along which the quality and intensity of a stimulus can be sparsely represented across magnitudes of concentrations (Figure 27). As such, depolarization block might be an inherent component of sensory population coding across phyla.

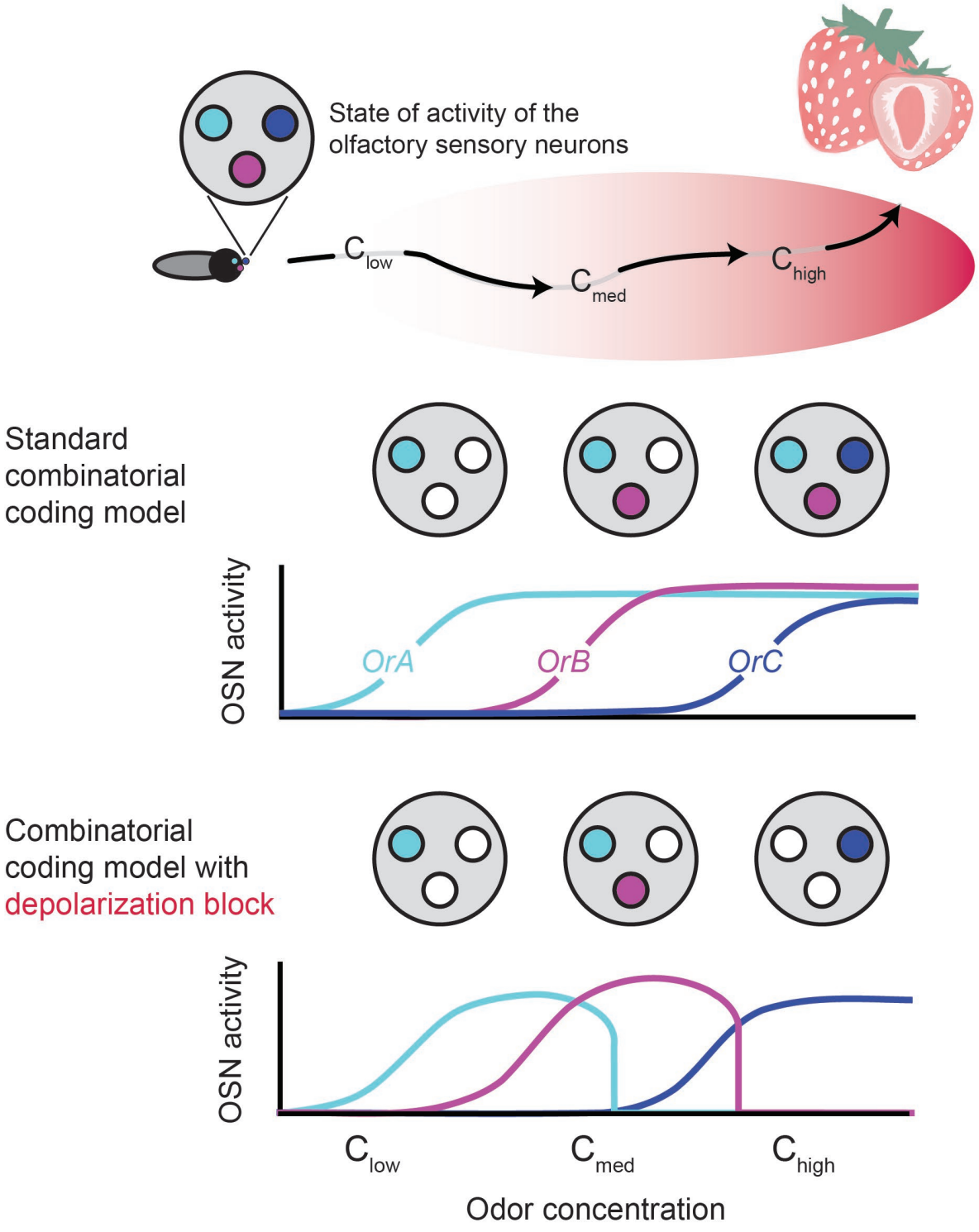

Figure 27: Comparison of the standard combinatorial coding model with and without the effects of depolarization block. (Top) While approaching an odor source (strawberry),

an animal experiences different concentrations of the odor, depending on its distance to the source. **(Center)** Representation of different odor concentrations by the peripheral olfactory system assuming a sigmoidal dose response curve. As the animal approaches the source, an increasing number of olfactory sensory neurons (colored circles) get recruited. **(Bottom)** Our results indicate that depolarization block limits the activity domain of each olfactory sensory neuron to a band of concentration, allowing the olfactory code to remain sparser even at high-odor concentrations.

Odor Discrimination in Olfactory Sensory Neurons

Introduction

In the last chapter, we showed that depolarization block is a feature of several olfactory sensory neurons (OSNs) in the larval olfactory system and developed a computational model to predict the firing activity of the *Or42b* OSN to the fruity odor ethyl butyrate. This changed our existing understanding of how olfactory systems encodes both odor identity and intensity (Figure 27). This led to the question: how does a combinatorial coding model with depolarization block facilitate the peripheral encoding of different odors? What are the advantages of such a design? Our natural next step was to investigate the role of depolarization block in the peripheral encoding of different odors through odor discrimination.

To answer this question, we designed an odor discrimination learning assay to understand when and how the larval olfactory system distinguishes one odor from another. By pairing animals experiencing one odor with a fructose reward, followed by the experience of a different odor without the fructose reward, we were able to observe situations where animals would have a learned preference when both odors were presented at the same time. In other words, we could use this associative learning [89] to identify which pairs of odors were discriminable by the larval olfactory system.

While the *Drosophila* larva has a computationally much simpler olfactory system than larger animal models like mice, studying discrimination via combinatorial coding in the larva is nevertheless quite a complex task as the wild-type larva possesses 21 total pairs of

OSNs. In other words, the peripheral encoding of odors in the larva is a 21-dimensional problem. Focusing our attention on addressing the foundational principles of combinatorial coding, we used genetic manipulation to reduce the number of functional OSNs in our experimental larvae from 21 OSNs to just 2 OSNs: the *Or42a* and *Or42b* OSNs (we will refer to these animals as *Or42a/b* double functional larvae). This allowed us to study the neural representations of odors in a computationally tractable two-dimensional space.

Next, to understand how these different odors were encoded at the sensory periphery by larval OSNs during the odor discrimination learning assay, our quantification required a computational model to determine the mapping from sensory input to firing activity. Thus, we adapted our 3D odor diffusion model to different odors, and developed a generalized version of the OSN model [5] to predict the firing activity of multiple OSNs to combinations of different odors. This allowed us to build a data analysis pipeline where we could infer the neural representation of odors experienced by animals based on their positions in the behavioral assay.

The neural basis of olfactory discrimination and sensory discrimination in general has yet to be fully understood. In olfaction, it is established that different odors activate different subsets of odorant receptors, which have certain affinities for binding depending on the type of odorant molecule [48], [90]. For example, the smells of pineapple and strawberry could be encoded by activating different groups of OSNs in the olfactory system. However, it is unknown how downstream neurons use these encodings to compute and classify the identity of these odors. Besides comparing which subsets of OSNs are firing or not, a neural circuit could also hypothetically compare the magnitude of the firing activity or even the temporal activity patterns of the OSNs [91]. While the neural implementation of classification is

unknown, there is evidence suggesting that neural encodings of sensation are more separable than behaviorally possible [92]. This would suggest that discrimination in biological neural circuits is less accurate than theoretically possible.

In classical machine learning, discriminant analysis is a standard technique to separate different classes of objects. In such methods, training consists of determining a hyperplane that "best" separates two or more groups of observations, for example the smell of pineapple versus strawberry. During testing, this hyperplane is then used to classify whether different observations of odors belong to strawberry or pineapple. While there exist many variants of theoretical methods for building such a classifier, such as linear discriminant analysis, quadratic discriminant analysis, and support vector machines [93], it is unknown how biological neural circuits categorize different classes of observations.

In this chapter, we use the biophysical OSN model to investigate the neural implementation of discrimination, which provides a step in linking theoretical methods of classification from artificial neural networks with biological neural circuits.

Materials and Methods

Behavioral data collection

All behavioral experiments were conducted with *Or42a/b* double functional (DF) PiVR [94]. In the odor discrimination learning assay, the experimental protocol consisted of a training phase followed by a test phase. In the training phase (Figure 28A), groups of 20 larvae are presented with a single odor while crawling on sweet (36% fructose) agarose, with odor sources placed on the left and right side of the arena. The same larvae are then

moved to another dish without fructose where another odor is present. After 3 repeats, the larvae are then placed in a dish with both odors (Figure 28B). Experiments are always run in pairs to account for differences in innate attraction to individual odors. The learning index is calculated by counting the number of animals on each side of the dish divided by the total number of animals before subtracting the result of one condition by the other. In each stage of the experiment, the motion of larvae in the arena is recorded using a video camera over the course of 3 minutes.

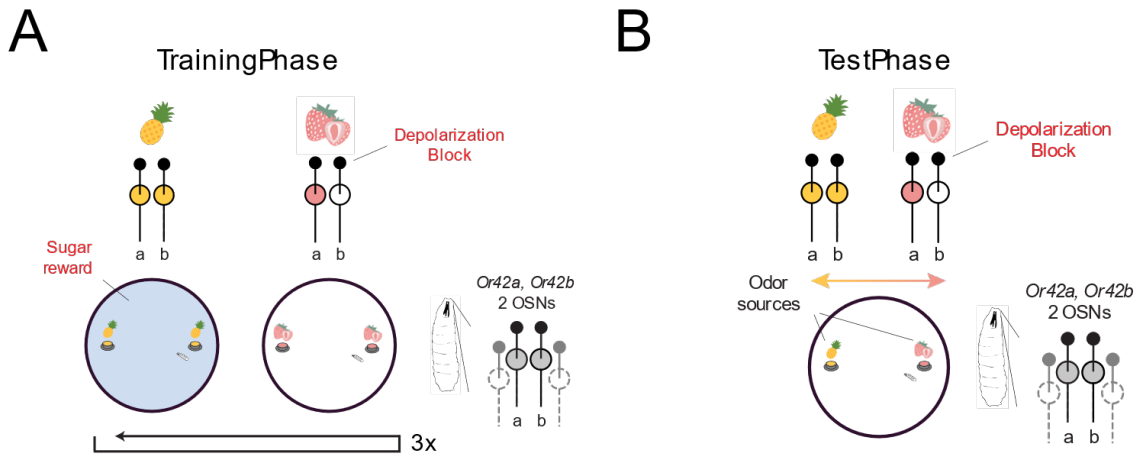

Figure 28: Methodology of the odor discrimination learning assay. (A) Training phase of the odor discrimination learning assay. During each round of training, *Or42a, Or42b* double functional larvae are placed in an arena in groups of 20 for 3 minutes. This arena has a single type of odor (i.e. pineapple) paired with a fructose reward. The larvae are then immediately transferred to an arena with a different type of odor with no reward (i.e. strawberry) for another 3 minutes. This process is repeated 3 times. **(B)** Test phase of the odor discrimination learning assay. After training, the same group of 20 larvae are placed into an arena with both the rewarded odor (i.e. pineapple) and the non-rewarded odor (i.e. strawberry) for 3 minutes.

Trajectory Reconstruction

For each experiment, we identified the positions of individual larvae during both the training and test phases. This was achieved using an adapted version of the motion-based multiple object tracking algorithm in MATLAB to automate the extraction of larvae trajectories from video datasets (Figure 29). The learning index calculated using the automated tracking algorithm was found to be in excellent agreement with a manually counted learning index. In the original off-the-shelf implementation, the tracking algorithm was found to perform well when the larvae were well separated and away from the odor sources, but performed poorly when larvae aggregated under the odor sources. To avoid losing track of larvae at the odor sources, a counter was added to keep track of missing larvae entering and leaving the vicinity of the odor sources.

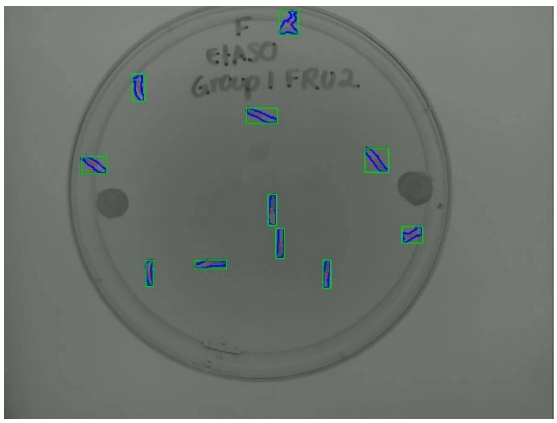

Figure 29: Motion-based multiple larvae tracking in the odor discrimination learning assay.

Physical model for odor diffusion

The sensory experience of larvae in the behavioral assay was quantified using the same methodology outlined in the previous chapter using a 3D odor diffusion model. In contrast

with the behavioral assay developed to study depolarization block [5], we used a circular arena instead of a rectangular arena, again modelled with the open-source CAD software OpenSCAD [57]. The arena was similar in size as before with a diameter of 85mm and a height of 7mm, as illustrated in Figure 30A. Experimentally, the main difference was the use of cylindrical odor cups to contain the odor droplet rather than the reinforcement rings used in the previous study. Due to the small aperture of the odor cups, the odor cup, the flux of odor at the droplet-air boundary was smaller than previously observed, resulting in a more gradual change in the odor profile over time. To simulate this difference, we modelled the geometry of the cylindrical odor cup with a radius of 3mm and a height of 4mm. The odor droplet has a volume of $V_{drop} = 10$ μL and is located inside the odor cup in a cylindrical enclosure with a radius of 2mm and a height of 0.8mm. The walls of the odor cup are assumed as no-flux boundaries, and the odor droplet diffuses out the top of the odor cup through a single aperture with a radius of 0.5mm. In each experiment, the odor cup is positioned 37.5mm away from the center of the arena. We assume that the initial odorant concentration in the air is zero, while the initial odorant concentration in the droplet is equivalent to the applied source concentration.

The parameters of the model were fit to match Fourier transform-infrared spectroscopy (FT-IR) measurements [22] captured along two different cross sections of the arena at different time intervals. In the "close" configuration, the FT-IR beam is positioned along an axis with an angular separation of 18^o from the odor cup. In the "remote" configuration, the FT-IR beam is positioned further away with an angular separation of 90^o from the odor cup (Figure 30A). For each odor used in the odor discrimination learning assay, FT-IR measurements were collected at the close and remote configurations using two different

source dilutions. This resulted in different temporal odor profiles as shown in Figure 30B-D for ethyl acetate, ethyl butyrate, and methyl acetate. To fit the diffusion parameters for each odor, we performed parameter optimization using the global optimization toolbox of MATLAB. The objective was to minimize the normalized root mean squared error (RMSE) between the experimental and simulated odor concentrations observed along the close and remote configurations. After parameter optimization, we found that our odor simulations (solid lines) were in excellent agreement with the experimental odor profiles (dashed lines) shown in Figure 30B-D. In each simulation, we assume there is a delay of 30 seconds during which the odor diffuses from the odor cup into the air before each animal is introduced into the arena. We also assume, in the simulation of multiple odor sources, that there are no interactions between the odorant molecules affecting the individual odor profiles (Figure 30F).

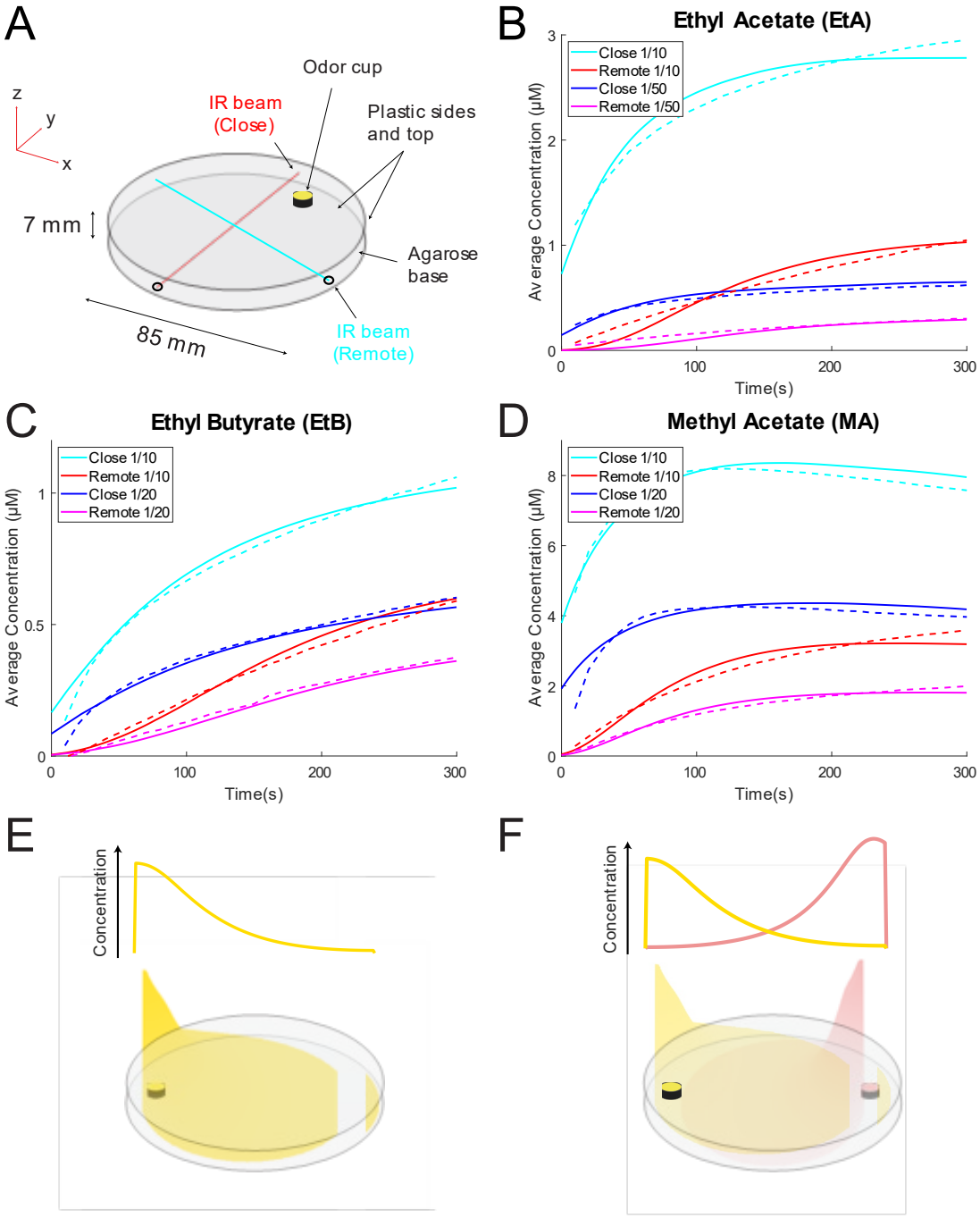

Figure 30: Adaptation of odor diffusion model for the odor discrimination learning assay. (A) Arena geometry with indicated features in the simulation. The odor profile was inferred from FT-IR absorption measurements [58] along two different cross-sections of the arena: close and remote. **(B-D)** Comparison of FT-IR derived odor concentration profiles (dashed lines) and simulated odor profiles after optimization of the 3D diffusion model

(plain lines) for several different odors: (B) ethyl acetate, (C) ethyl butyrate, and (D) methyl acetate. **(E)** Visualization of simulated odor profile for a single odor source of ethyl butyrate on the left side of the arena. **(F)** Visualization of simulated profile for an odor mixture of ethyl butyrate (left source) and ethyl acetate (right source).

Olfactory Sensory Neuron (OSN) Model

In the OSN model of the previous chapter, the odorant transduction module describes the interactions of a single odor ethyl butyrate with the *Or42b* expressing OSN. In this behavioral assay however, there is an additional layer of complexity as pairs of odor mixtures are interacting with the *Or42b* OSN, as well as with the *Or42a* OSN (Figure 31A). This process can be described using a competitive binding model, where different types of odorant molecules compete to attach to a limited number of receptors [95], [96]. This model assumes that only one odorant molecule can attach to receptor binding site at a time, and that different odorant-receptor interactions have different responses in their binding/unbinding kinetics. Since we tested the responses of two OSNS (*Or42a*, *Or42b*) to three different odors (ethyl acetate, ethyl butyrate, and methyl acetate), there were a total of six combinations of odorant-receptor interactions to consider.

By introducing competitive binding into the odor transduction model to account for odor mixtures, we have the following modified set of equations:

$$\begin{aligned} \frac{dx_{odor1}}{dt} &= b_{r,odor1}\, v_{odor1}\,(1 - x_1) - d_{r,odor1}\, x_{odor1} \\ \frac{dx_{odor2}}{dt} &= b_{r,odor2} v_{odor2}\,(1 - x_1) - d_{r,odor2}\, x_{odor2} \\ x_1 &= x_{odor1} + x_{odor2}. \end{aligned} \tag{59}$$

As in eq. (54), the variable x_1 models the fraction of odorant receptors that are bound at any given time. Since we presented odor mixtures of two different odors, odorant receptors can either be bound to the first odor or the second order, or not at all. Therefore, by defining x_{odor1} and x_{odor2} as the fraction of odorant receptors bound to the two respective odors, we have the total fraction of bound odorant receptors: $x_1 = x_{odor1} + x_{odor2}$. v_{odor1} and v_{odor2} represent the odorant concentration profiles for each odor experienced by the larvae. Similarly, $b_{r,odor1}$ and $b_{r,odor2}$ define their respective binding rate constants, while $d_{r,odor1}$ and $d_{r,odor2}$ their respective dissociation rate constants.

For the modelling of the co-receptor channel x_2, and the calcium channel x_3, we adopt the following equations:

$$\frac{dx_2}{dt} = \alpha_2\, x_1\,(1 - x_2) - \beta_2\, x_2 - \kappa\, x_2^{2/3}\, x_3^{2/3}$$
$$\frac{dx_3}{dt} = \alpha_3\, x_2 - \beta_3\, x_3, \tag{60}$$

where x_1 is the total fraction of odorant receptors bound by both odors. The parameters of eq. (60) are defined in the previous chapter [5]. All other equations in the odorant transduction model are identical as before. Note that besides the odorant-receptor specific binding/dissociation rates added to the odor transduction model, all other parameters remain the same as found in the previous chapter [5].

For the spike generator model, we assumed that the firing dynamics were similar across OSNs besides the different responses in odorant transduction. Therefore, we adopted the

same spike generator model and parameters for both the *Or42a* and *Or42b* OSNs (Figure 31B).

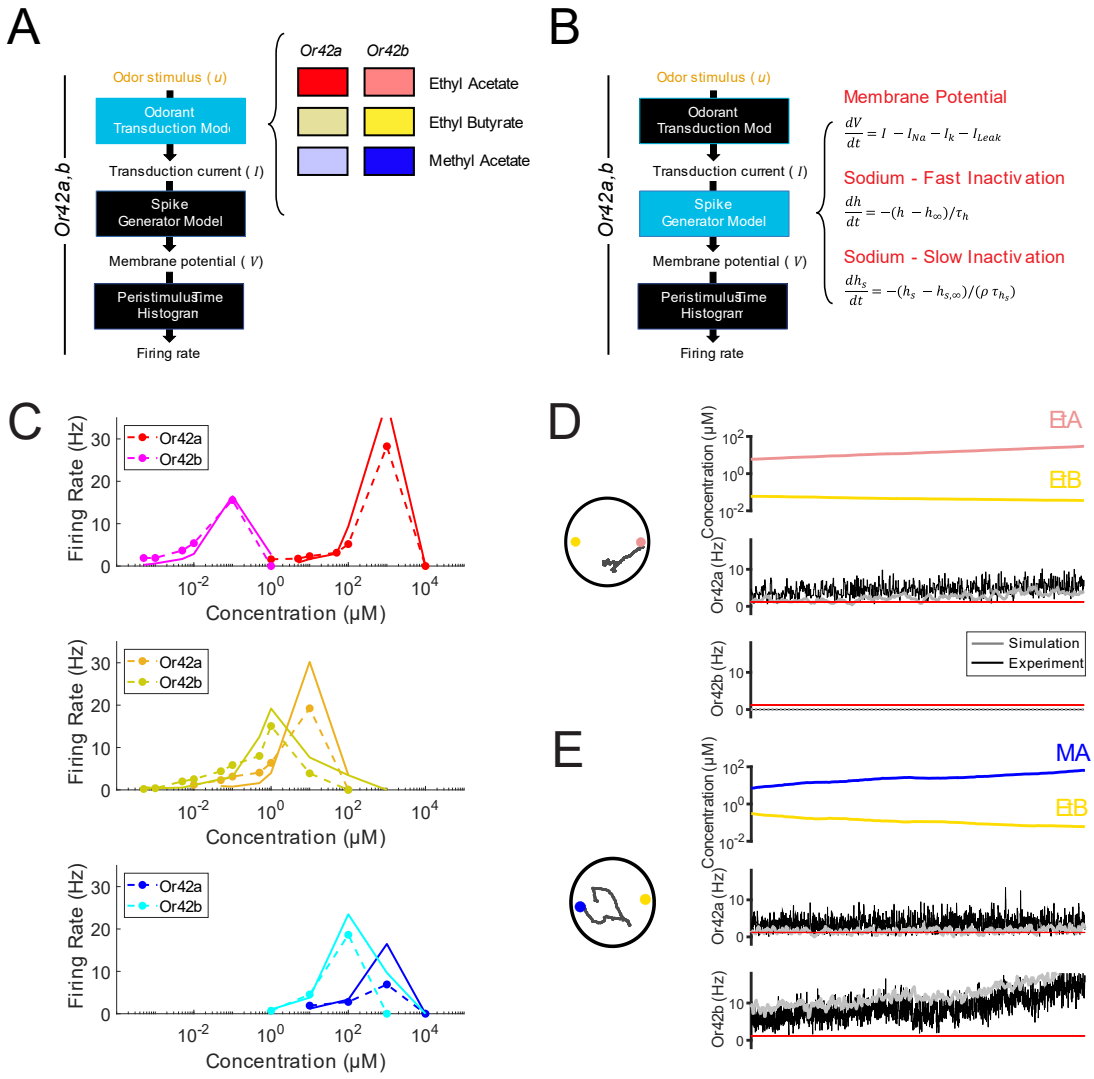

Figure 31: Expansion of the computational model reproducing depolarization block to different OSNs and odors. (A) Framework of the integrated OSN model [5] with an adapted odorant transduction model to account for differences between the *Or42a* and *Or42b* and their responses to different odors. **(B)** The spike generator model is assumed to be identical to that of the integrated OSN model [5] for both the *Or42a* and *Or42b* OSNs. **(C)** Dose responses of the mean tonic firing rates of real (dashed lines) and simulated (plain lines) *Or42a, Or42b* OSNs for: ethyl acetate (top), ethyl butyrate (middle), and methyl acetate (bottom). **(D)** Simulated OSN activity (gray, simulation; black, experiment) and odor experience for a sample trajectory of a single larva in an odor mixture of ethyl butyrate (left source) and ethyl acetate (right source). The red line indicates the basal firing activity of the OSNs. **(E)** Same as (D), for a sample trajectory of a single larva in an odor mixture of methyl acetate (left source) and ethyl butyrate (right source).

The *Or42a* and *Or42b* OSN models were optimized using electrophysiology recordings for different stimulus patterns for each type of odor. This consisted of step stimuli at different concentrations, along with a linear ramp, exponential ramp, and sigmoid ramp. Parameter optimization involved fitting the binding/dissociation rates for each odorant-receptor pair using the global optimization toolbox in MATLAB with a genetic algorithm. The objective was to minimize the normalized root mean squared error between the experimentally recorded firing rate and the predicted firing rate of the OSN model. In the parameter optimization procedure, we matched the number of simulated trials with the existing number of experimental trials.

Results

After parameter optimization, we were able to predict the responses of the *Or42a* and *Or42b* OSNs to single odors of ethyl acetate, ethyl butyrate, and methyl acetate. We found that modifying the binding/dissociation rates associated with the odor transduction model alone, was sufficient to account for the response profiles of both OSNs to different stimulus patterns. In addition, the dose response curves obtained from simulating the steady state response to step stimuli were in agreement with actual experimental electrophysiology recordings for both OSNs (Figure 31C).

To validate the OSN model, we extracted trajectory segments from the odor discrimination learning assay and simulated the expected odor concentrations experienced by the larvae over time. We then obtained electrophysiology recordings of these behavioral replays (Figure 31D-E). The question was whether the OSN model could predict the

responses to different combinations of odor mixtures and whether competitive binding was a valid assumption. Upon comparing the simulation of these trajectory segments using the OSN model with the experimental data, we observed that we were able to predict the firing activity of both OSNs to odor mixtures in the depolarization block regime (Figure 31D), as well as in the spiking regime (Figure 31E). With the accurate predictions of the biophysical OSN model, we now had a means for investigating when and how larvae were able to discriminate odors in the odor discrimination learning assay.

We began by simulating the firing activities experienced by larvae during training for different odor conditions. This data analysis pipeline involved first extracting the trajectory segments of larvae from videos obtained from the PiVR odor discrimination set-up. Next, we used these trajectories to simulate the odor concentration profiles experienced by larvae over the last 30 seconds of training. Finally, we used the OSN model to simulate the firing activity of the *Or42a* and *Or42b* OSNs based on these odor concentration profiles and extracted the mean firing activity over the last 3 seconds of the simulation. We performed this analysis for different dilutions of odor source concentrations: ethyl acetate (1:10K or $1{:}10 \times \mathbf{10^3}$, 1:1K, 1:50), ethyl butyrate (1:10K, 1:400, 1:175) and methyl acetate (1:25, 1:10). The result is illustrated in (Figure 32A,C), where each point represents the firing activity experienced for a given *Or42a/b* double functional larva. In Figure 32A, we plot the firing activities of larvae during the last phase of training for each odor paired with a fructose reward. In Figure 32C, we show the firing activities of the *Or42a* and *Or42b* OSNs during the last phase of training for the same odor without the fructose reward. We observe that regardless of whether fructose is rewarded or not, that the OSN firing activities experienced during training are similar as shown by where the clusters corresponding to

each odor are situated in the neural map (Figure 32B, D). We also observe that each odor exists in different well separated manifolds in this two-dimensional *Or42a-vs-Or42b* neural map, gradually moving towards the upper right at increasing odor concentrations. Note that depolarization block caused by excessive stimuli results in the OSN firing activity to crash abruptly to zero, as observed in the odor condition ethyl acetate 1:50 (EtA50).

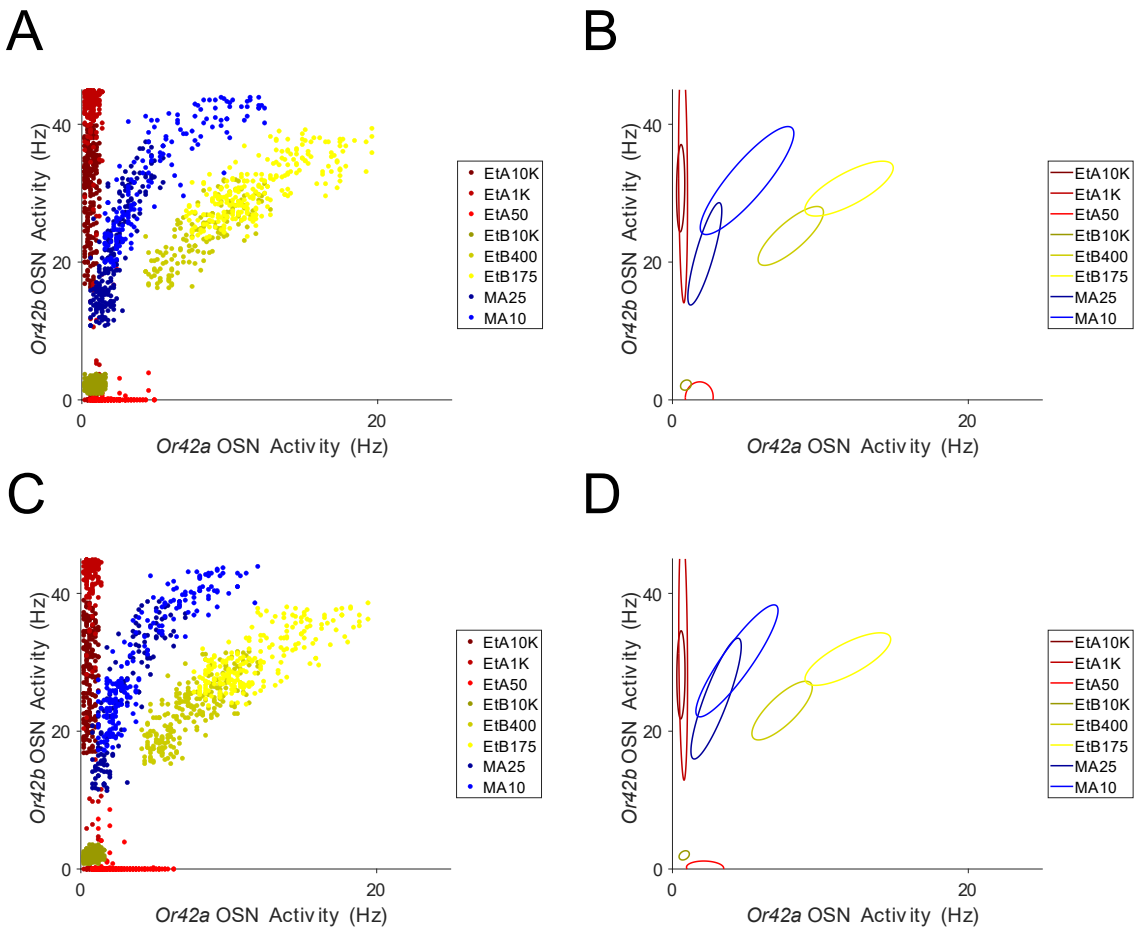

Figure 32: Representations of different odors in the 2D *Or42a, Or42b* neural space. Simulated steady state OSN activities of experimental larvae trajectories during training under different odor dilutions (red - ethyl acetate 1:10K or 1:10 × $\mathbf{10^3}$, 1:1K, 1:50; yellow - ethyl butyrate 1:10K, 1:400, 1:175; methyl acetate 1:25, 1:10) **(B)** Neural map of the same conditions in (A) when fit with a Gaussian model. **(C)** Same as (A) but with no fructose reward. **(D)** Same as (B) but with no fructose reward.

Out of all these different odor conditions, we selected several pairs and asked whether larvae would be able to discriminate the two, using the experimental protocol described in Figure 28. At the most basic level, we first compared ethyl acetate 1:10K with ethyl butyrate 1:10K. In order for larvae to discriminate these two odors, they would need to recognize that ethyl acetate 1:10K (red) leads to firing of the *Or42b* OSN while ethyl butyrate 1:10K (yellow) does not (Figure 33A). For both odors, the *Or42a* OSN is below firing threshold and remains silent. Thus, the question is whether the binary response of a single OSN allows larvae to discriminate.

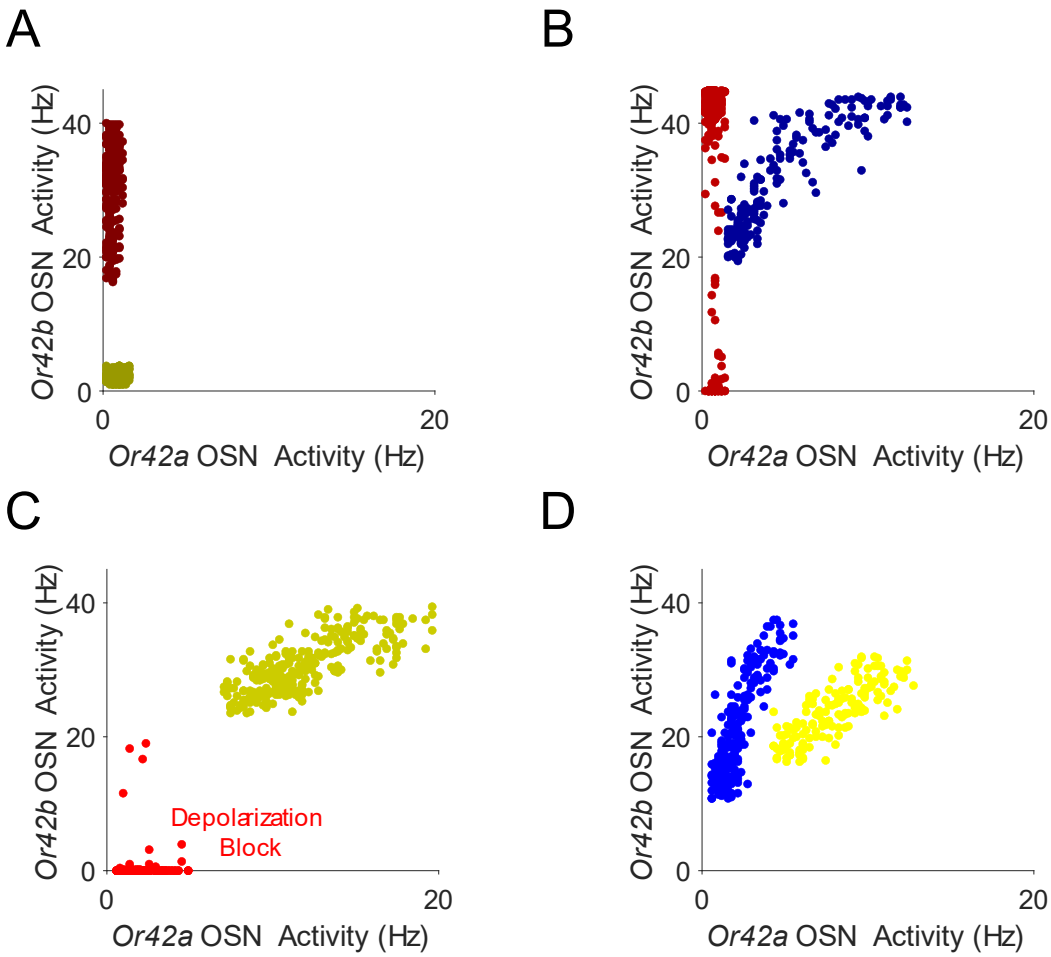

Figure 33: Simulated representation of neural activity experienced during the training phase for different odors paired with fructose reward. (A) Ethyl acetate 1:10K (red) vs. ethyl butyrate 1:10K (yellow). **(B)** Ethyl acetate 1:1K (red) vs. methyl acetate 1:10 (blue). **(C)** Ethyl acetate 1:50 (red) vs. ethyl butyrate 1:175 (yellow). **(D)** Ethyl butyrate 1:400 (yellow) vs. methyl acetate 1:25 (blue).

In the remaining odor conditions from Figure 33B-D, we ask under what circumstances larvae would be able to discriminate odors that activate both the *Or42a* and *Or42b* OSNs. In Figure 33B, the odor ethyl acetate 1:1K (red) activates the *Or42b* OSN, while methyl acetate 1:10 (blue) activates both the *Or42a* and *Or42b* OSNs. Since the *Or42a* OSN has similar

firing activity for both odors, larvae would need to rely on the response of *Or42b* to perform odor discrimination.

In Figure 33C, we test a similar scenario between ethyl acetate 1:50 (red) and ethyl butyrate 1:175 (yellow). In this case, the odor ethyl acetate 1:50 activates the *Or42a* OSN, while ethyl butyrate 1:175 activates both the *Or42a* and *Or42b* OSNs. This is similar to the previous condition in Figure 33B where one odor is activating one OSN while the other odor is activating two OSNs. However, one caveat is that while the *Or42b* OSN is silent under the stimulus of ethyl acetate 1:50, the OSN is also undergoing depolarization block. Compared to the previous condition, the question is whether the addition of depolarization block enhances or has any effect on discrimination.

In the last remaining condition illustrated in Figure 33D, we test the limits of discrimination by introducing a condition where each odor activates both the *Or42a* and *Or42b* OSNs. To discriminate ethyl butyrate 1:400 (yellow) and methyl acetate 1:25 (blue), a simple binary threshold on either OSN is not enough since one cannot find a threshold on either the *Or42a* or *Or42b* OSN that separates the two clusters perfectly. Instead, separating these clusters would involve a model at least as complex as a linear discriminant [93], which would require computing linear combinations of OSN activities.

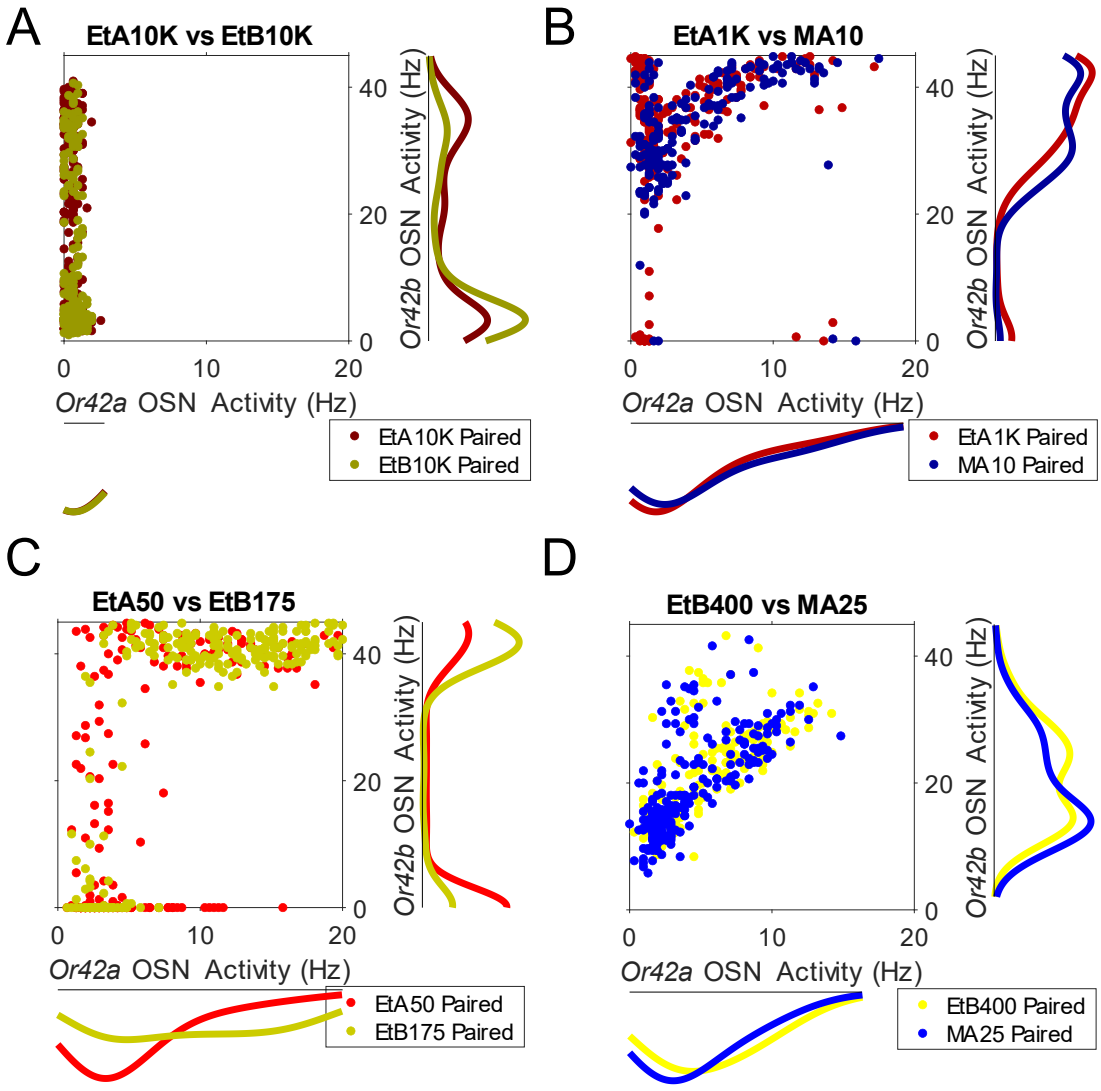

Figure 34: Simulated representation of neural activity experienced during the test phase for different pairs of odors. (A) Ethyl acetate 1:10K (red) vs. ethyl butyrate 1:10K (yellow). **(B)** Ethyl acetate 1:1K (red) vs. methyl acetate 1:10 (blue). **(C)** Ethyl acetate 1:50 (red) vs. ethyl butyrate 1:175 (yellow). **(D)** Ethyl butyrate 1:400 (yellow) vs. methyl acetate 1:25 (blue).

After the training phases, we investigated whether larvae developed a bias during the test phase when both odors were presented at once. Using the 2D neural representation introduced in Figure 32, we found that depending on which odor larvae were paired with the

fructose reward, that they would have an increased tendency to seek out the fructose paired odor source during the test phase. This effect is illustrated in Figure 34, which shows the distribution of firing activities experienced by larvae in the test phase. We can observe from the striking difference in the distributions for the conditions in Figures 34A and C, that on average more larvae are aggregating in regions where they had experienced the fructose reward during training. However, for the conditions in Figures 34B and D, this learning effect is less pronounced as the distributions between the paired conditions look more similar visually.

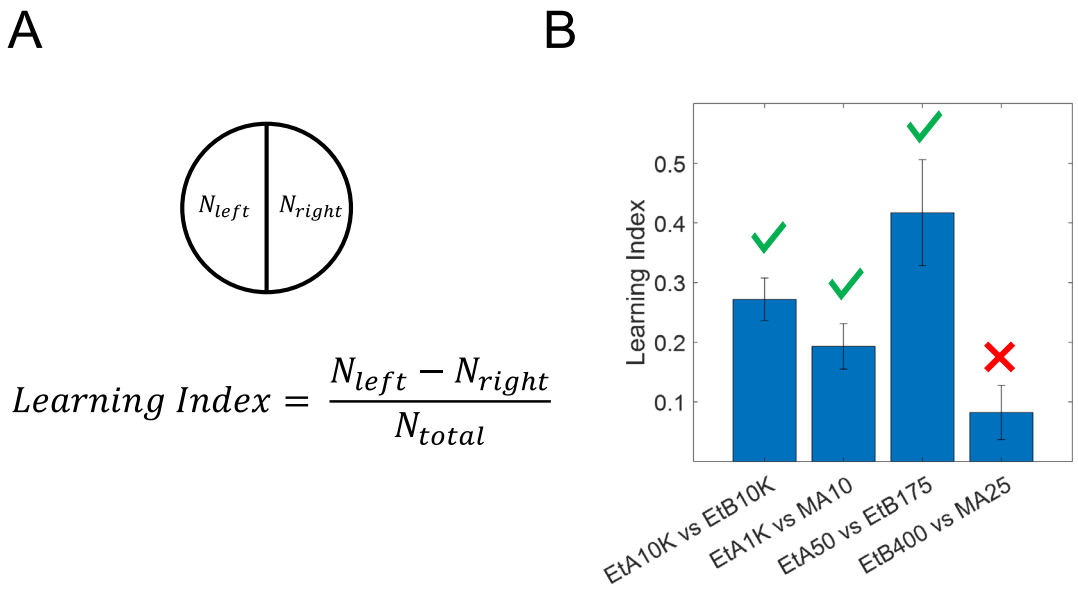

Figure 35: Experimental learning index for each tested odor pairing. (A) Illustration of the learning index. **(B)** Learning indices for each odor condition determined using automated trajectory reconstruction. The error bars denote the standard error of the mean.

To quantify exactly how well the larvae are discriminating the odors after training, we defined a learning index (LI) [97]:

(61)

$$LI = \frac{N_{left} - N_{right}}{N_{total}}$$

Where N_{left} is the number of larvae on the side of the arena with the fructose-paired odor, N_{right} is the number of larvae on the other half of the arena, and N_{total} is the total number of experimentally tested animals. The learning index is calculated at the end of the test phase. The learning index is bounded between -1 and 1: larvae that learn perfectly will have a performance of $LI = 1$, while larvae that always select the odor without the fructose reward would have a performance of $LI = -1$ (this would be equivalent to aversive learning).

For the first three conditions from Figure 33A-C, we observed that larvae were able to discriminate between the two odors (Figure 35B). In particular, the condition comparing ethyl acetate 1:50 with ethyl butyrate 1:175 (Figure 33C) displayed the highest *LI*, which coincidentally is the only condition with depolarization block. The last condition had a low *LI* and did not have a statistically significant difference when compared to the control with no fructose reward (Figure 35D).

Discussion

To understand why the conditions from Figure 33A-C are discriminable while Figure 33D is not, we built classifiers to investigate how simple it is in theory to discriminate each condition. In Figure 36, we used the support vector machine algorithm to find a firing rate threshold for either the *Or42a* or *Or42b* OSN that best separates the clusters corresponding to each odor. In the case of the support vector machine, the best separation is defined as

maximizing the margin between the points from each cluster that are closest to the decision boundary.

For ethyl acetate 1:10K vs. ethyl butyrate 1:10K (Figure 36A), the training clusters are well separated by a threshold on the *Or42b* OSN activity. For ethyl acetate 1:1K vs. methyl acetate 1:10 (Figure 36B), a threshold on the *Or42a* OSN activity also separates the training clusters, though the margin between the two classes is smaller. Given that the inter-class distance (the Euclidean distance between the neural representations of different odors) is the main difference between these two conditions, it is likely that the inter-class margin in neural representations plays a role in how well larvae discriminate. This may explain why the learning index for the latter condition is slightly lower in Figure 35B.

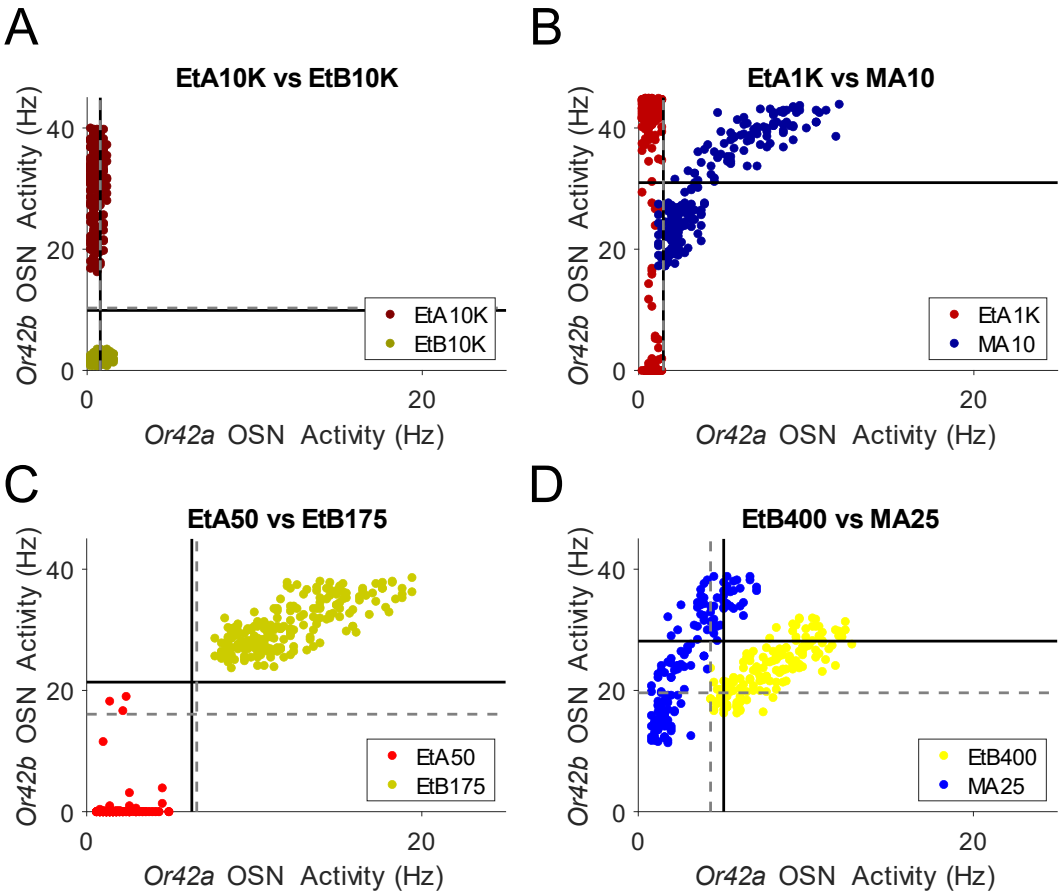

Figure 36: Theoretical implementation of discrimination over 1 dimension. The solid and dotted lines represent the decision boundaries for the two respective groups of larvae paired with each odor. **(A)** Ethyl acetate 1:10K (red) vs. ethyl butyrate 1:10K (yellow). **(B)** Ethyl acetate 1:1K (red) vs. methyl acetate 1:10 (blue). **(C)** Ethyl acetate 1:50 (red) vs. ethyl butyrate 1:175 (yellow). **(D)** Ethyl butyrate 1:400 (yellow) vs. methyl acetate 1:25 (blue).

For the condition with the highest learning index, ethyl acetate 1:50 vs. ethyl butyrate 1:175 (Figure 36C), we can see that the training clusters are easily separable by thresholds over both the *Or42a* and *Or42b* OSN activities. This condition also has the feature of depolarization block induced by the odor ethyl acetate 1:50 in the *Or42b* OSN, bringing the *Or42b* OSN below the basal firing rate. Thus, depolarization block may assist in

discrimination by increasing the inter-class distances between neural representations of odors.

On the other hand, for the condition with the lowest learning index in Figure 36D, we observe that the training clusters are non-separable by thresholds over the *Or42a* and *Or42b* OSN activities. Although the inter-class distance between Figure 36B and Figure 36D are similar, ethyl butyrate 1:400 vs. methyl acetate 1:25 has a significantly lower learning index. This provides a hint as to how larvae implement decision boundaries, because while this odor condition is non-separable using the thresholds applied in Figure 36, the training clusters are actually separable if we consider the slightly more sophisticated linear discrimination (Figure 35). However, this method of discrimination would require the larvae to be able to compute linear combinations of OSN activities. So far, our data suggests that larvae are unable to accomplish this. With the various odor concentrations tested in Figure 32, our next step is to perform additional experiments to confirm the type of classifier that larvae implement in their olfactory neural circuitry.

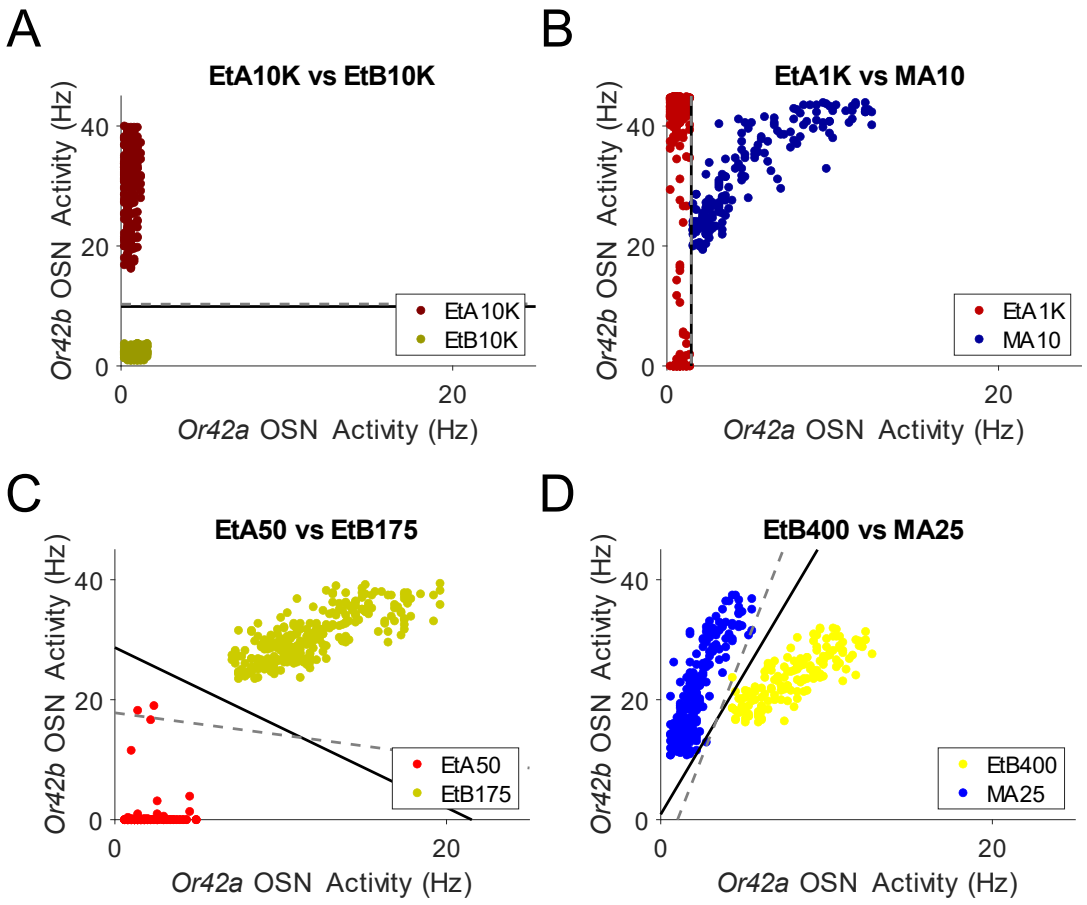

Figure 37: Theoretical implementation of linear discrimination using a support vector machine. The solid and dotted lines represent the decision boundaries for the two respective groups of larvae paired with each odor. **(A)** Ethyl acetate 1:10K (red) vs. ethyl butyrate 1:10K (yellow). **(B)** Ethyl acetate 1:1K (red) vs. methyl acetate 1:10 (blue). **(C)** Ethyl acetate 1:50 (red) vs. ethyl butyrate 1:175 (yellow). **(D)** Ethyl butyrate 1:400 (yellow) vs. methyl acetate 1:25 (blue).

While the neural correlates of olfactory discrimination have not yet been discovered, our biophysical simulations of OSNs at the sensory periphery provides a step forward in understanding the neural representations of odor identity and intensity [98]. Furthermore, our odor discrimination learning assay with *Or42a/b* double functional larvae provides a simple testbed for investigating the type of computations that biological neural circuits use

to classify sensory information, which is difficult to study in higher-order model organisms due to their overwhelming complexity. Here, our simulations suggest that neural representations of odors are encoded more precisely at the sensory periphery rather than behaviorally (Figure 35D), which is consistent with recent findings demonstrating that neural precision surpasses behavioral precision in mice and in humans [92]. Our approach, similar to ref. [90], shows that theoretical classifiers like support vector machines or linear discriminant analysis can be used to decode odor identities from neural representations of odors.

Given that depolarization block brings the firing activities of OSNs below their basal firing rates, it appears that this feature enhances discrimination by adding an extra dimension to the neural code of olfaction. Depolarization block also promotes sparsity, which has been shown to be beneficial in olfaction to overcome the bottleneck in the limited number of olfactory receptor types [99]. This sets the stage for us to show quantitatively whether depolarization block enhances the overall theoretical coding capacity of the olfactory sensory system.

Conclusion

In summary, we utilized computational models to study several fundamental computations involving sensory coding and processing in the olfactory system of the *Drosophila* larva. In the first chapter, we developed an agent-based model to explore how the *Drosophila* larva combines multisensory cues and found that neural circuits in an insect brain are capable of computing signal variance and performing probabilistic inference [4]. In the second chapter, we developed a biophysical model of OSNs to study the dynamics of depolarization block in olfaction [5]. In the final chapter, we used our biophysical OSN model to explore how depolarization block contributes to odor encoding and discrimination, allowing us to also discover clues revealing how biological neural circuits perform classification.

In future work, it would be exciting to expand our biophysical neuron models beyond the sensory periphery of the OSNs and study the dynamics of the olfactory sensory system at a network level. This would allow us to, for example, pinpoint the computations of downstream neurons performing odor discrimination. In addition, the underlying dynamics of these neuron models may uncover temporal aspects of odor encoding not considered previously [100]. With the recent arrival of the *Drosophila* larva connectome and the rapid progress of imaging techniques to reconstruct and record high resolution representations of the brain [1], it is an opportune time to study the computational mechanisms of olfaction in the *Drosophila* larva.

References

[1] M. Winding *et al.*, "The connectome of an insect brain," *Science (80-.).*, vol. 379, no. 6636, p. eadd9330, 2023, doi: 10.1126/science.add9330.

[2] C. Eschbach and M. Zlatic, "Useful road maps: studying Drosophila larva's central nervous system with the help of connectomics," *Curr. Opin. Neurobiol.*, vol. 65, pp. 129–137, 2020, doi: https://doi.org/10.1016/j.conb.2020.09.008.

[3] S. Herculano-Houzel, "The human brain in numbers: a linearly scaled-up primate brain," *Front. Hum. Neurosci.*, p. 31, 2009.

[4] P. Wong *et al.*, "Computational principles of adaptive multisensory combination in the Drosophila larva," *bioRxiv*, pp. 2005–2023, 2023.

[5] D. Tadres, P. H. Wong, T. To, J. Moehlis, and M. Louis, "Depolarization block in olfactory sensory neurons expands the dimensionality of odor encoding.," *Sci. Adv.*, vol. 8, no. 50, p. eade7209, Dec. 2022, doi: 10.1126/sciadv.ade7209.

[6] D. C. Knill and A. Pouget, "The Bayesian brain: the role of uncertainty in neural coding and computation.," *Trends Neurosci.*, vol. 27, no. 12, pp. 712–719, Dec. 2004, doi: 10.1016/j.tins.2004.10.007.

[7] M. O. Ernst and M. S. Banks, "Humans integrate visual and haptic information in a statistically optimal fashion," *Nature*, vol. 415, no. January, pp. 429–433, 2002.

[8] J. M. Hillis, S. J. Watt, M. S. Landy, and M. S. Banks, "Slant from texture and disparity cues: Optimal cue combination," *J. Vis.*, vol. 4, no. 12, pp. 967–992, 2004, doi: 10.1167/4.12.1.

[9] Y. Gu, D. E. Angelaki, and G. C. DeAngelis, "Neural correlates of multisensory cue

integration in macaque MSTd," *Nat. Neurosci.*, vol. 11, no. 10, pp. 1201–1210, 2008, doi: 10.1038/nn.2191.

[10] A. Wystrach, M. Mangan, and B. Webb, "Optimal cue integration in ants," *Proc. R. Soc. B Biol. Sci.*, vol. 282, no. 1816, 2015, doi: 10.1098/rspb.2015.1484.

[11] X. Sun, S. Yue, and M. Mangan, "A decentralised neural model explaining optimal integration of navigational strategies in insects," *Elife*, vol. 9, pp. 1–30, 2020, doi: 10.7554/eLife.54026.

[12] T. A. Currier, A. M. M. Matheson, and K. I. Nagel, "Encoding and control of orientation to airflow by a set of drosophila fan-shaped body neurons," *Elife*, vol. 9, pp. 1–29, 2020, doi: 10.7554/eLife.61510.

[13] W. J. Ma, J. M. Beck, P. E. Latham, and A. Pouget, "Bayesian inference with probabilistic population codes," *Nat. Neurosci.*, vol. 9, no. 11, pp. 1432–1438, 2006, doi: 10.1038/nn1790.

[14] J. Jordan, J. Sacramento, W. A. M. Wybo, M. A. Petrovici, and W. Senn, "Learning Bayes-optimal dendritic opinion pooling," *bioRxiv*, pp. 1–28, 2021, [Online]. Available: http://arxiv.org/abs/2104.13238.

[15] M. E. Berck *et al.*, "The wiring diagram of a glomerular olfactory system," *Elife*, vol. 5, no. May 2016, pp. 1–21, 2016, doi: 10.7554/eLife.14859.

[16] R. Gepner, M. M. Skanata, N. M. Bernat, M. Kaplow, and M. Gershow, "Computations underlying Drosophila photo- taxis, odor-taxis, and multi-sensory integration," *Elife*, vol. 4, no. May, pp. 1–21, 2015, doi: 10.7554/eLife.06229.

[17] R. Gepner, J. Wolk, D. S. Wadekar, S. Dvali, and M. Gershow, "Variance adaptation in navigational decision making," *Elife*, vol. 7, pp. 1–32, 2018.

[18] M. Klein *et al.*, “Sensory determinants of behavioral dynamics in Drosophila thermotaxis,” *Proc. Natl. Acad. Sci. U. S. A.*, vol. 112, no. 2, pp. E220–E229, 2015, doi: 10.1073/pnas.1416212112.

[19] L. Luo *et al.*, “Navigational decision making in Drosophila thermotaxis,” *J. Neurosci.*, vol. 30, no. 12, pp. 4261–4272, 2010, doi: 10.1523/JNEUROSCI.4090-09.2010.

[20] M. Louis, “Mini-brain computations converting dynamic olfactory inputs into orientation behavior.,” *Curr. Opin. Neurobiol.*, vol. 64, pp. 1–9, Oct. 2020, doi: 10.1016/j.conb.2019.11.015.

[21] A. Wystrach, K. Lagogiannis, and B. Webb, “Continuous lateral oscillations as a core mechanism for taxis in Drosophila larvae,” *Elife*, 2016, doi: 10.7554/eLife.15504.

[22] M. Louis, T. Huber, R. Benton, T. P. Sakmar, and L. B. Vosshall, “Bilateral olfactory sensory input enhances chemotaxis behavior,” *Nat. Neurosci.*, vol. 11, no. 2, pp. 187–199, 2008, doi: 10.1038/nn2031.

[23] A. Schulze *et al.*, “Dynamical feature extraction at the sensory periphery guides chemotaxis,” *Elife*, pp. 1–52, 2015, doi: 10.7554/eLife.06694.

[24] W. A. Tucker and L. H. Nelken, “Diffusion coefficients in air and water,” *Handb. Chem. Prop. Estim. Methods Environ. Behav. Org. Compd. Am. Chem. Soc. Washington, DC. 1990. p 17. 1-17. 25. 7 tab, 28 ref.*, 1990.

[25] M. Adler and U. Alon, “Fold-change detection in biological systems,” *Curr. Opin. Syst. Biol.*, vol. 8, pp. 81–89, 2017, doi: 10.1016/j.coisb.2017.12.005.

[26] N. Kadakia and T. Emonet, “Front-end Weber-Fechner gain control enhances the fidelity of combinatorial odor coding,” *Elife*, vol. 8, pp. 1–21, 2019, doi:

10.7554/elife.45293.

[27] L. H. Cao *et al.*, “Distinct signaling of Drosophila chemoreceptors in olfactory sensory neurons,” *Proc. Natl. Acad. Sci. U. S. A.*, vol. 113, no. 7, pp. E902–E911, 2016, doi: 10.1073/pnas.1518329113.

[28] A. Gomez-Marin and M. Louis, “Active sensation during orientation behavior in the Drosophila larva: More sense than luck,” *Curr. Opin. Neurobiol.*, vol. 22, no. 2, pp. 208–215, 2012, doi: 10.1016/j.conb.2011.11.008.

[29] L. Hernandez-Nunez *et al.*, “Synchronous and opponent thermosensors use flexible cross-inhibition to orchestrate thermal homeostasis,” *Sci. Adv.*, vol. 7, no. 35, 2021, doi: 10.1126/sciadv.abg6707.

[30] N. C. Klapoetke *et al.*, “Independent optical excitation of distinct neural populations,” *Nat. Methods*, vol. 11, no. 3, pp. 338–346, 2014, doi: 10.1038/nmeth.2836.

[31] H. Akaike, “Information theory and an extension of the maximum likelihood principle,” in *Selected papers of hirotugu akaike*, Springer, 1998, pp. 199–213.

[32] G. Schwarz, “Estimating the dimension of a model,” *Ann. Stat.*, pp. 461–464, 1978.

[33] G. Si *et al.*, “Structured Odorant Response Patterns across a Complete Olfactory Receptor Neuron Population,” *Neuron*, vol. 101, no. 5, pp. 950-962.e7, 2019, doi: 10.1016/j.neuron.2018.12.030.

[34] S. A. Kreher, D. Mathew, J. Kim, and J. R. Carlson, “Translation of sensory input into behavioral output via an olfactory system.,” *Neuron*, vol. 59, no. 1, pp. 110–124, Jul. 2008, doi: 10.1016/j.neuron.2008.06.010.

[35] S. Gorur-Shandilya, M. Demir, J. Long, D. A. Clark, and T. Emonet, “Olfactory receptor neurons use gain control and complementary kinetics to encode intermittent

odorant stimuli," *Elife*, vol. 6, pp. 1–30, 2017, doi: 10.7554/eLife.27670.

[36] J. Negen *et al.*, "Sensory cue combination in children under 10 years of age," *Cognition*, vol. 193, no. December 2018, p. 104014, 2019, doi: 10.1016/j.cognition.2019.104014.

[37] R. B. Welch and D. H. Warren, "Immediate perceptual response to intersensory discrepancy," *Psychol. Bull.*, vol. 88, no. 3, pp. 638–667, 1980, doi: 10.1037/0033-2909.88.3.638.

[38] J. P. Bresciani, F. Dammeier, and M. O. Ernst, "Vision and touch are automatically integrated for the perception of sequences of events," *J. Vis.*, vol. 6, no. 5, pp. 554–564, 2006, doi: 10.1167/6.5.2.

[39] K. Asahina, M. Louis, S. Piccinotti, and L. B. Vosshall, "A circuit supporting concentration-invariant odor perception in Drosophila.," *J. Biol.*, vol. 8, no. 1, p. 9, 2009, doi: 10.1186/jbiol108.

[40] M. Demir, N. Kadakia, H. D. Anderson, D. A. Clark, and T. Emonet, "Walking Drosophila navigate complex plumes using stochastic decisions biased by the timing of odor encounters," *Elife*, vol. 9, pp. 1–43, 2020, doi: 10.7554/eLife.57524.

[41] T. H. Weisswange, C. A. Rothkopf, T. Rodemann, and J. Triesch, "Bayesian cue integration as a developmental outcome of reward mediated learning," *PLoS One*, vol. 6, no. 7, 2011, doi: 10.1371/journal.pone.0021575.

[42] S. Gepshtein, J. Burge, M. O. Ernst, and M. S. Banks, "The combination of vision and touch depends on spatial proximity," *J. Vis.*, vol. 5, no. 11, pp. 1013–1023, 2005, doi: 10.1167/5.11.7.

[43] B. N. Danforth, "Emergence dynamics and bet hedging in a desert bee, Perdita

portalis," *Proc. R. Soc. B Biol. Sci.*, vol. 266, no. 1432, pp. 1985–1994, 1999, doi: 10.1098/rspb.1999.0876.

[44] A. M. M. Matheson *et al.*, "A neural circuit for wind-guided olfactory navigation," *Nat. Commun.*, vol. 13, no. 1, 2022, doi: 10.1038/s41467-022-32247-7.

[45] O. J. Ahmed *et al.*, "Inhibitory single neuron control of seizures and epileptic traveling waves in humans," *BMC Neurosci.*, vol. 15, no. 1, p. F3, 2014, doi: 10.1186/1471-2202-15-S1-F3.

[46] C. J. Marcuccilli *et al.*, "Neuronal bursting properties in focal and parafocal regions in pediatric neocortical epilepsy stratified by histology," *J. Clin. Neurophysiol.*, vol. 27, no. 6, p. 387—397, Dec. 2010, doi: 10.1097/wnp.0b013e3181fe06d8.

[47] J. P. Dreier *et al.*, "How spreading depolarization can be the pathophysiological correlate of both migraine aura and stroke.," *Acta Neurochir. Suppl.*, vol. 120, pp. 137–140, 2015, doi: 10.1007/978-3-319-04981-6_23.

[48] A. A. Lazar and C. H. Yeh, *A molecular odorant transduction model and the complexity of spatio-temporal encoding in the Drosophila antenna*, vol. 16, no. 4. 2020.

[49] K. Qian, N. Yu, K. R. Tucker, E. S. Levitan, and C. C. Canavier, "Mathematical analysis of depolarization block mediated by slow inactivation of fast sodium channels in midbrain dopamine neurons," *J. Neurophysiol.*, vol. 112, no. 11, pp. 2779–2790, 2014, doi: 10.1152/jn.00578.2014.

[50] M. C. Larsson, A. I. Domingos, W. D. Jones, M. E. Chiappe, H. Amrein, and L. B. Vosshall, "Or83b encodes a broadly expressed odorant receptor essential for Drosophila olfaction," *Neuron*, vol. 43, no. 5, pp. 703–714, 2004, doi:

10.1016/j.neuron.2004.08.019.

[51] A. L. Hodgkin and A. F. Huxley, “A quantitative description of membrane current and its application to conduction and excitation in nerve,” *J. Physiol.*, vol. 117, no. 4, p. 500, 1952.

[52] K. I. Nagel and R. I. Wilson, “Biophysical mechanisms underlying olfactory receptor neuron dynamics.,” *Nat. Neurosci.*, vol. 14, no. 2, pp. 208–216, Feb. 2011, doi: 10.1038/nn.2725.

[53] D. J. Hoare, C. R. McCrohan, and M. Cobb, “Precise and fuzzy coding by olfactory sensory neurons.,” *J. Neurosci. Off. J. Soc. Neurosci.*, vol. 28, no. 39, pp. 9710–9722, Sep. 2008, doi: 10.1523/JNEUROSCI.1955-08.2008.

[54] M. de Bruyne, K. Foster, and J. R. Carlson, “Odor coding in the Drosophila antenna.,” *Neuron*, vol. 30, no. 2, pp. 537–552, May 2001, doi: 10.1016/s0896-6273(01)00289-6.

[55] A. A. Dobritsa, W. van der Goes van Naters, C. G. Warr, R. A. Steinbrecht, and J. R. Carlson, “Integrating the molecular and cellular basis of odor coding in the Drosophila antenna.,” *Neuron*, vol. 37, no. 5, pp. 827–841, Mar. 2003, doi: 10.1016/s0896-6273(03)00094-1.

[56] E. A. Hallem, M. G. Ho, and J. R. Carlson, “The molecular basis of odor coding in the Drosophila antenna.,” *Cell*, vol. 117, no. 7, pp. 965–979, Jun. 2004, doi: 10.1016/j.cell.2004.05.012.

[57] M. Kintel and C. Wolf, “OpenSCAD,” *GNU Gen. Public Licens. p GNU Gen. Public Licens.*, 2014.

[58] M. Louis, T. Huber, R. Benton, T. P. Sakmar, and L. B. Vosshall, “Bilateral olfactory

sensory input enhances chemotaxis behavior," *Nat. Neurosci.*, vol. 11, no. 2, pp. 187–199, 2008, doi: 10.1038/nn2031.

[59] H. K. M. Dweck *et al.*, "The Olfactory Logic behind Fruit Odor Preferences in Larval and Adult Drosophila," *Cell Rep.*, vol. 23, no. 8, pp. 2524–2531, 2018, doi: 10.1016/j.celrep.2018.04.085.

[60] M. Cobb, "What and how do maggots smell?," *Biol. Rev.*, vol. 74, no. 4, pp. 425–459, 1999, doi: 10.1111/j.1469-185X.1999.tb00037.x.

[61] E. O. Aceves-Piña and W. G. Quinn, "Learning in normal and mutant Drosophila larvae.," *Science*, vol. 206, no. 4414, pp. 93–96, Oct. 1979, doi: 10.1126/science.206.4414.93.

[62] P. Monte, C. Woodard, R. Ayer, M. Lilly, H. Sun, and J. Carlson, "Characterization of the larval olfactory response in Drosophila and its genetic basis.," *Behav. Genet.*, vol. 19, no. 2, pp. 267–283, Mar. 1989, doi: 10.1007/BF01065910.

[63] E. Fishilevich, A. I. Domingos, K. Asahina, F. Naef, L. B. Vosshall, and M. Louis, "Chemotaxis behavior mediated by single larval olfactory neurons in Drosophila.," *Curr. Biol.*, vol. 15, no. 23, pp. 2086–2096, Dec. 2005, doi: 10.1016/j.cub.2005.11.016.

[64] M. J. Jordán, K. Tandon, P. E. Shaw, and K. L. Goodner, "Aromatic Profile of Aqueous Banana Essence and Banana Fruit by Gas Chromatography−Mass Spectrometry (GC-MS) and Gas Chromatography−Olfactometry (GC-O)," *J. Agric. Food Chem.*, vol. 49, no. 10, pp. 4813–4817, Oct. 2001, doi: 10.1021/jf010471k.

[65] S. T. Sweeney, K. Broadie, J. Keane, H. Niemann, and C. J. O'Kane, "Targeted expression of tetanus toxin light chain in Drosophila specifically eliminates synaptic

transmission and causes behavioral defects.," *Neuron*, vol. 14, no. 2, pp. 341–351, Feb. 1995, doi: 10.1016/0896-6273(95)90290-2.

[66] K. Asahina, M. Louis, S. Piccinotti, and L. B. Vosshall, "A circuit supporting concentration-invariant odor perception in Drosophila," *J. Biol.*, vol. 8, no. 1, 2009, doi: 10.1186/jbiol108.

[67] C. S. Hong and B. Ganetzky, "Molecular characterization of neurally expressing genes in the para sodium channel gene cluster of drosophila.," *Genetics*, vol. 142, no. 3, pp. 879–892, Mar. 1996, doi: 10.1093/genetics/142.3.879.

[68] W.-H. Lin, C. Günay, R. Marley, A. A. Prinz, and R. A. Baines, "Activity-Dependent Alternative Splicing Increases Persistent Sodium Current and Promotes Seizure," *J. Neurosci.*, vol. 32, no. 21, pp. 7267–7277, 2012, doi: 10.1523/JNEUROSCI.6042-11.2012.

[69] S. H. Strogatz, *Nonlinear Dynamics and Chaos: With Applications to Physics, Biology, Chemistry and Engineering*. Westview Press, 2000.

[70] B. Malnic, J. Hirono, T. Sato, and L. B. Buck, "Combinatorial receptor codes for odors.," *Cell*, vol. 96, no. 5, pp. 713–723, Mar. 1999, doi: 10.1016/s0092-8674(00)80581-4.

[71] E. A. Hallem and J. R. Carlson, "Coding of odors by a receptor repertoire.," *Cell*, vol. 125, no. 1, pp. 143–160, Apr. 2006, doi: 10.1016/j.cell.2006.01.050.

[72] M. Meister and T. Bonhoeffer, "Tuning and Topography in an Odor Map on the Rat Olfactory Bulb," *J. Neurosci.*, vol. 21, no. 4, pp. 1351–1360, 2001, doi: 10.1523/JNEUROSCI.21-04-01351.2001.

[73] M. Wachowiak and L. B. Cohen, "Representation of odorants by receptor neuron

input to the mouse olfactory bulb.," *Neuron*, vol. 32, no. 4, pp. 723–735, Nov. 2001, doi: 10.1016/s0896-6273(01)00506-2.

[74] D. Münch and C. G. Galizia, "DoOR 2.0--Comprehensive Mapping of Drosophila melanogaster Odorant Responses.," *Sci. Rep.*, vol. 6, p. 21841, Feb. 2016, doi: 10.1038/srep21841.

[75] F. Martin and E. Alcorta, "Measuring activity in olfactory receptor neurons in Drosophila: Focus on spike amplitude," *J. Insect Physiol.*, vol. 95, pp. 23–41, 2016, doi: 10.1016/j.jinsphys.2016.09.003.

[76] G. Sicard, "Electrophysiological recordings from olfactory receptor cells in adult mice.," *Brain Res.*, vol. 397, no. 2, pp. 405–408, Nov. 1986, doi: 10.1016/0006-8993(86)90648-7.

[77] T. Connelly, A. Savigner, and M. Ma, "Spontaneous and sensory-evoked activity in mouse olfactory sensory neurons with defined odorant receptors.," *J. Neurophysiol.*, vol. 110, no. 1, pp. 55–62, Jul. 2013, doi: 10.1152/jn.00910.2012.

[78] P. Duchamp-Viret, A. Duchamp, and M. A. Chaput, "Peripheral Odor Coding in the Rat and Frog: Quality and Intensity Specification," *J. Neurosci.*, vol. 20, no. 6, pp. 2383–2390, 2000, doi: 10.1523/JNEUROSCI.20-06-02383.2000.

[79] R. Gross-Isseroff and D. Lancet, "Concentration-dependent changes of perceived odor quality," *Chem. Senses*, vol. 13, no. 2, pp. 191–204, 1988, doi: 10.1093/chemse/13.2.191.

[80] D. G. Laing, P. K. Legha, A. L. Jinks, and I. Hutchinson, "Relationship between Molecular Structure, Concentration and Odor Qualities of Oxygenated Aliphatic Molecules," *Chem. Senses*, vol. 28, no. 1, pp. 57–69, 2003, doi:

10.1093/chemse/28.1.57.

[81] S. B. Laughlin, R. R. de Ruyter van Steveninck, and J. C. Anderson, “The metabolic cost of neural information.,” *Nat. Neurosci.*, vol. 1, no. 1, pp. 36–41, May 1998, doi: 10.1038/236.

[82] A. Călin, A. S. Ilie, and C. J. Akerman, “Disrupting Epileptiform Activity by Preventing Parvalbumin Interneuron Depolarization Block.,” *J. Neurosci. Off. J. Soc. Neurosci.*, vol. 41, no. 45, pp. 9452–9465, Nov. 2021, doi: 10.1523/JNEUROSCI.1002-20.2021.

[83] A. Bragin, M. Penttonen, and G. Buzsáki, “Termination of epileptic afterdischarge in the hippocampus.,” *J. Neurosci. Off. J. Soc. Neurosci.*, vol. 17, no. 7, pp. 2567–2579, Apr. 1997, doi: 10.1523/JNEUROSCI.17-07-02567.1997.

[84] K. El Houssaini, C. Bernard, and V. K. Jirsa, “The Epileptor Model: A Systematic Mathematical Analysis Linked to the Dynamics of Seizures, Refractory Status Epilepticus, and Depolarization Block.,” *eNeuro*, vol. 7, no. 2, 2020, doi: 10.1523/ENEURO.0485-18.2019.

[85] A. Dovzhenok and A. S. Kuznetsov, “Exploring neuronal bistability at the depolarization block,” *PLoS One*, vol. 7, no. 8, 2012, doi: 10.1371/journal.pone.0042811.

[86] E. Marder, L. F. Abbott, G. G. Turrigiano, Z. Liu, and J. Golowasch, “Memory from the dynamics of intrinsic membrane currents.,” *Proc. Natl. Acad. Sci. U. S. A.*, vol. 93, no. 24, pp. 13481–13486, Nov. 1996, doi: 10.1073/pnas.93.24.13481.

[87] E. S. Milner and M. T. H. Do, “A Population Representation of Absolute Light Intensity in the Mammalian Retina,” *Cell*, vol. 171, no. 4, pp. 865-876.e16, 2017, doi:

10.1016/j.cell.2017.09.005.

[88] Y. V Zhang, J. Ni, and C. Montell, “The molecular basis for attractive salt-taste coding in Drosophila.,” *Science*, vol. 340, no. 6138, pp. 1334–1338, Jun. 2013, doi: 10.1126/science.1234133.

[89] J. M. Pearce and M. E. Bouton, “Theories of Associative Learning in Animals,” *Annu. Rev. Psychol.*, vol. 52, no. 1, pp. 111–139, 2001, doi: 10.1146/annurev.psych.52.1.111.

[90] B. Roland, T. Deneux, K. M. Franks, B. Bathellier, and A. Fleischmann, “Odor identity coding by distributed ensembles of neurons in the mouse olfactory cortex,” pp. 1–26, 2017, doi: 10.7554/eLife.26337.

[91] G. Laurent, M. Wehr, and H. Davidowitz, “Temporal representations of odors in an olfactory network.,” *J. Neurosci. Off. J. Soc. Neurosci.*, vol. 16, no. 12, pp. 3837–3847, Jun. 1996, doi: 10.1523/JNEUROSCI.16-12-03837.1996.

[92] C. Stringer, M. Michaelos, D. Tsyboulski, S. E. Lindo, and M. Pachitariu, “High-precision coding in visual cortex,” *Cell*, vol. 184, no. 10, pp. 2767-2778.e15, 2021, doi: 10.1016/j.cell.2021.03.042.

[93] R. O. Duda, P. E. Hart, and others, *Pattern classification*. John Wiley \& Sons, 2006.

[94] D. Tadres and M. Louis, “PiVR: An affordable and versatile closed-loop platform to study unrestrained sensorimotor behavior,” *PLoS Biol.*, vol. 18, no. 7, pp. 1–25, 2020, doi: 10.1371/journal.pbio.3000712.

[95] V. Singh, N. R. Murphy, V. Balasubramanian, and J. D. Mainland, “Competitive binding predicts nonlinear responses of olfactory receptors to complex mixtures,” *Proc. Natl. Acad. Sci. U. S. A.*, vol. 116, no. 19, pp. 9598–9603, 2019, doi:

10.1073/pnas.1813230116.

[96] J. P. Rospars, P. Lansky, M. Chaput, and P. Duchamp-Viret, “Competitive and noncompetitive odorant interactions in the early neural coding of odorant mixtures,” *J. Neurosci.*, vol. 28, no. 10, pp. 2659–2666, 2008, doi: 10.1523/JNEUROSCI.4670-07.2008.

[97] B. Michels *et al.*, “Pavlovian conditioning of larval Drosophila: An illustrated, multilingual, hands-on manual for odor-taste associative learning in maggots,” *Front. Behav. Neurosci.*, vol. 11, no. April, pp. 1–6, 2017, doi: 10.3389/fnbeh.2017.00045.

[98] M. Stopfer, V. Jayaraman, and G. Laurent, “Intensity versus identity coding in an olfactory system.,” *Neuron*, vol. 39, no. 6, pp. 991–1004, Sep. 2003, doi: 10.1016/j.neuron.2003.08.011.

[99] K. Krishnamurthy, A. M. Hermundstad, T. Mora, and A. M. Walczak, “Disorder and the Neural Representation of Complex Odors,” vol. 16, no. August, 2022, doi: 10.3389/fncom.2022.917786.

[100] C. D. Wilson, G. O. Serrano, A. A. Koulakov, and D. Rinberg, “A primacy code for odor identity,” *Nat. Commun.*, vol. 8, no. 1, 2017, doi: 10.1038/s41467-017-01432-4.